UNIVERSIDAD DE SONORA

DIVISIÓN DE INGENIERÍA

DEPARTAMENTO DE INVESTIGACIÓN EN POLÍMEROS Y MATERIALES

"EXPLORATION OF THE FREE ENERGY LANDSCAPES OF BORON, BERYLLIUM AND COPPER NANOCLUSTERS AT FINITE TEMPERATURE VIA DFT AND STATISTICAL THERMODYNAMICS"

TESIS

Que para obtener el título de

DOCTOR EN CIENCIA DE MATERIALES

Presenta:

M. en C. Carlos Emiliano Buelna García

Director:

Dr. Jesús Manuel Quiroz Castillo

Codirector:

Dr. Jose Luis Cabellos Quiroz

Hermosillo, Sonora. 22 de Febrero del 2023

Institutional Statement

Dr. Teresa del Castillo Castro
Head of department

Hermosillo, Sonora, february 22, 2023.

This Thesis was elaborated, presented, and defended

by:

M. Sc. Carlos Emiliano Buelna García

Reviewed and approved by the committee:

Dr. Jesus Manuel Quiroz Castillo (Director)	April 13, 2023 Date
Dr. José Luis Cabellos Quiroz (Co-Director)	April 13, 2023 Date
Dra. Dora Evelia Rodríguez Félix (Sinodal)	April 13, 2023 Date
Dr. José Carmelo Encinas Encinas (Sinodal)	April 13, 2023 Date
Dra. Diana Vargas Hernández (Sinodal)	April 13, 2023 Date
Dr. Teresa del Castillo Castro (Sinodal)	April 13, 2023 Date

Universidad de Sonora.
Hermosillo, Sonora, México, february 22, 2023

Declaration of Authorship

I declare this thesis entitled: ***Exploration of the free energy landscapes of boron, beryllium and copper nanoclusters at finite temperature via DFT and statistical thermodynamics*** is a work of my own authority, which has been done to defend of my Doctoral work at the *Universidad de Sonora*. This work was made under the guidance of Dr. Jesús Manuel Quiroz-Castillo of the *Universidad de Sonora* and Dr. José Luis Cabellos-Quiroz of the *Universidad Politécnica de Tapachula*.

Dedication

I dedicate this work to my parents.

Acknowledgments

Thanks to all **my friends and colleagues**

I thank Dr. **Jesús Manuel Quiroz-Castillo**. An apprenticeship and a long road full of obstacles, which have been necessary to overcome. None of this would have been possible without the help received from Dr. Jesús Manuel Quiroz, thanks for being a guide in my development, and his support during this process was without a doubt very helpful.

I thank Dr. **José Luis Cabellos** for being a guide in my development, for having the patience to support and advise me during the course of this project. Thanks for helping to open my eyes to see the real path to science, and above all, for being a good friend.

I thank M. Sc. **Edgar Paredes-Sotelo** for all the help you have offered me and all the what I have learned from him. Its practically total availability when solving problems.

I thank M. Sc. **Francisco Eduardo Rojas González** for share his knowledge and all scientific discussion and beyond on all the weekends.

I thank Dr. **Khirbet López Velázquez** for all the suggestions and observations made during the development of this thesis.

Many thanks to my **thesis committee**; all their observations were of great help during the development of this work. I thank you for your time and support during these past years.

Thanks to **Dra. Carmen Heras** and L.C.C. **Daniel Mendoza Camacho** of the supercomputing department of Universidad de Sonora for allowing me to use the ACARUS supercomputer and all of its resources. Without their support, this work could not have been completed.

To **CONACyT** for the financial support it gave me with the grant number 860052 of the program *Becas Nacionales* of **CONACyT**.

Abstract

Clusters are aggregates of atoms that are too large to be called molecules and too small to resemble crystal fragments and their properties are highly dependent on structure, size, composition, and temperature; however, most theoretical studies of density functional assume that the temperature is 0 K and neglect temperature-dependent contributions as their finite-temperature properties remain virtually unexplored. Experimental studies are carried out at temperatures higher than 0 K, and it is necessary to understand the effect of temperature on the properties of the cluster and also on the determination of the lowest energetic structure at finite temperature. In this doctoral thesis, we conducted a theoretical-computational study at finite temperature of the structural, thermochemical, and electronic properties of atomic nanoclusters formed by elements of Boron, Beryllium and Copper using density functional theory and statistical thermodynamics. The knowledge of the minimum energy geometries and the most energetically unstable isomers are essential in calculating electronic, and geometric properties, which consequently provide a complete vision of the molecular system. The starting point for understanding the properties of the cluster is the putative global minimum and all lower energy structures near it; locating those low-energy structures is only the first difficult step. Combined DFT with statistical thermodynamics, we roughly calculated the relative thermal populations highly dependent on temperature and the effect of temperature on IR spectra. To elucidate the lowest energy structure and their neighbors, we conducted an extensive and systematic global exploration of potential/free energy landscapes to locate the low-energy structures of clusters formed by B, Be, and Cu atoms. To achieve what was mentioned above, we employed a hybrid genetic algorithm, developed and implemented by our research group, written in *Python* and coupled to any electronic structure program available; Also, we developed the computational codes necessary for calculating the thermochemical properties.

Resumen

Los cúmulos son agregados de átomos que son demasiado grandes para llamarse moléculas y demasiado pequeños para parecerse a fragmentos de cristal, y sus propiedades dependen en gran medida de la estructura, el tamaño, la composición y la temperatura; sin embargo, la mayoría de los estudios teóricos del funcional de densidad asumen que la temperatura es 0 K y desprecian las contribuciones dependientes de la temperatura, como consequencia sus propiedades a temperatura finita permanecen prácticamente sin explorar. Considerando que los estudios experimentales se llevan a cabo a temperaturas finitias, desde el punto de vista teorico, es necesario comprender el efecto de la temperatura sobre las propiedades del cúmulo y también sobre la determinación de la estructura energética más baja a temperatura finita. En esta tesis doctoral realizamos un estudio teórico-computacional a temperatura finita de las propiedades estructurales, termoquímicas y electrónicas de nanoclusters atómicos formados por elementos de Boro, Berilio y Cobre utilizando la teoría funcional de la densidad y la termodinámica estadística. El conocimiento de las geometrías de mínima energía y de los isómeros energéticamente más inestables es fundamental para el cálculo de las propiedades electrónicas y geométricas, que en consecuencia proporcionan una visión completa del sistema molecular. El punto de partida para comprender las propiedades del cúmulo es el mínimo global putativo y todas las estructuras de menor energía cercanas; ubicar esas estructuras de baja energía es solo el primer paso difícil. Combinando DFT con termodinámica estadística, calculamos aproximadamente las poblaciones térmicas relativas altamente dependientes de la temperatura y el efecto de la temperatura en los espectros IR. Para dilucidar la estructura de energía más baja y sus vecinos, llevamos a cabo una exploración global extensa y sistemática de los paisajes de energía libre/potencial para ubicar las estructuras de baja energía de los grupos formados por átomos de B, Be y Cu. Para lograr lo mencionado anteriormente, empleamos un algoritmo genético híbrido, desarrollado e implementado por nuestro grupo de investigación, escrito en *Python* y acoplado a cualquier programa de estructura electrónica disponible; Además, desarrollamos los códigos computacionales necesarios para el cálculo de las propiedades termoquímicas.

Contents

List of Figures

List of Tables

Chapter 1

Introduction

1.1 Introduction

The first step in understanding the molecular properties is elucidating the lowest energy structure and its isomers. The minimum energy structure, the distribution of its isomers, as well as its properties depend to a great extent on the temperature, and with the aim to compute the molecular properties of atomic clusters considering the temperature, it is necessary to consider statistical mechanics. Additionally, the cluster properties depend on the structure, size, and composition, and as mentioned earlier, the temperature plays an important role; however, most theoretical density functional studies assume that temperature is 0 K and their finite temperature properties remain virtually unexplored. On the other hand, experimental studies are carried out in non-zero temperatures, and it is necessary to understand the effect of the temperature on the cluster properties and the determination of the lowest energy structure at finite temperatures.

In this doctoral thesis, we employed density functional theory and statistics thermochemistry to elucidate the effects of the temperature on the determination of the lowest energy structure and its isomers on the potential/free energy surface and the importance of the contribution of the higher energy structures to the IR spectrum. These contributions are taken into account through weight's Boltzmann factors dependents on temperature and show that these high energy geometries are determinants in the IR and UV spectra, inducing changes in the spectrum's shape and amplitudes. In order to take into account these contributions, a couple of things were considered: first, An extensive and systematic search of the lowest energy structures was performed on the potential/free energy surfaces of atomic clusters, using an unbiased hybrid search algorithm coupled to density functional theory (DFT) based on kicking and basing genetic methodologies. Second, the temperature effects on the populations were taken into account through thermochemical properties. As a result, we present how the effect of the temperature is taken into account through the contributions of higher energy structures. As far as we know, for atomic clusters a) no work has attempted to investigate entropy-driven isomers distribution employing b) the effect of the temperature on the IR spectroscopy. To explore the basis set dependence of the optimized geometries, isomers distribution, and computed IR spectrum, we used a basis set Def2tzvp. The starting point requires searching the global minimum on the potential and free energy surfaces. This is a complicated task due to several factors. The degree of difficulty increases with the number of atoms; the calculation of energy requires quantum mechanical energy methodology

to produce a realistic energy value. Furthermore, the number of initial structures should be large enough to ensure that we are not missing structures making an incomplete sampling of the configurational space introducing a major problem in the computation of the thermodynamic properties. Although the problem of searching for global minimum in molecular systems is challenging, the design and use of algorithms dedicated to the search for global minima, such as simulated annealing, genetic algorithms [1, 2, 3], as Gradient Embedded Genetic Algorithm (GEGA), basin hopping, Monte Carlo, particle swarm optimization, graph theory, or the big bang search algorithm, has been made over the years and they have lead us to solve, in a targeted way, the minimum global search. The simplest and easiest way for searching global minimum consist in generating structures with random atomic positions within a finite box, which will be optimized using any quantum mechanical program. The kick method has been used extensively until nowadays; one of the emerging kick methods was used by Saunders in 1987 at the global minimum search of the cycloheptane molecule, and several years later used a complete automated kick procedure in small carbon molecules, imposing some restrictions to the starting point structures, coupled to Density Functional Theory (DFT) methods to find their global minimum. Many works have employed this technique or some variants in several systems,to find the global minimum. Although the search of the global and local minima is helpful in understanding reactivities and catalytic efficiencies, such studies often neglect temperature-dependent entropic contributions to free energy when increasing temperature. And has been done in sodium clusters. Temperature into account requires dealing with the thermodynamics of small systems, the thermodynamics of clusters have been studied by a variety of theoretical and simulation tools, these include Monte Carlo and molecular-dynamics simulations and analytic methods. This contributions can be computed within the so called harmonic superposition approximation or superposition method, this method originally developed for thermodynamics observable only, was improved phonologically by including anharmonic corrections, and extended to others cluster properties. In this approach the partition function is written as a sum over all the minimum on the potential energy surface, and by restricting the sum to a certain subset of the minimal the thermodynamic properties can be obtained. The solid-solid transition occurs when the partition function of two competing structures types area equal means that there are simultaneous coexistence of structural isomers at T, (the Tss computation can be obtained by parallel tempering) The structure corresponding to the global minimum ceases to be the most likely at high T so other structure prevail, As second step for understanding cluster properties relies on their spectroscopy, spectroscopy gives insight into structure and it was proposed as a way of detecting structural transformations into clusters. The influence of temperature on the spectroscopy has been computed before for a variety of clusters, for instance, such in the present study, we will use the statistical formulation of thermodynamics to compute thermodynamics properties and evaluate the relative populations among the isomers and the effects on IR specta. As far as we know, this has not been carried out. In the present doctoral thesis a systematic unbiased search for the lowest energy structures of cluster.

We discuss the influence (or effects) of temperature on the Cu, Be, and B structures, thus the Gibbs energy of the isomers are evaluated statistical mechanically at every degree from 5 to 1500 K, relative populations, dependents of temperature, are computed based on the Boltzmann distribution using the Gibbs free energy also we investigate the effects of temperature on the IR spectrums. Features of the spectrum could be seen to originate from the competition among several clusters.

1.1.1 General objective

The general objective of this thesis is the development of a computational-theoretical study based on density functional theory and thermochemistry that considers the temperature effect on the computation of molecular properties of atomic clusters formed by Be, B, and Cu atoms.

1.1.2 Specific objectives

1. Implementation of the code *galgoYaqui* for the search of structures of minimum energy of atomic clusters based on *Darwinian* theory, written in *Python*, coupled with *Gaussian 09* and running on a parallel machine.

2. Exploration of free energy landscapes to search the putative global minima and the most energetically important isomers in atomic clusters, using the code *galgoYaqui*, and formed by atoms from group Be, B, and Cu atoms.

3. Implementation of the *termoYaqui* code for the inclusion of temperature effects in the calculation of atomic properties.

4. Exploration of free energy landscapes and thermal computation of $Be_6B_{11}^{-1}$ cluster.

5. Exploration of free energy landscapes and thermal computation of Be_4B_8 cluster.

6. Exploration of free energy landscapes and thermal computation of Cu_{13} cluster.

7. Exploration of free energy landscapes and thermal computation of Cu_{38} cluster.

1.1.3 Justification

Experimental studies are carried out at temperatures higher than 0 K; therefore, at a theoretical level, it is necessary to understand what is the effect of temperature on the properties of the cluster, and no less important is that the temperature is essential in achieving the activation energy needed to perform a chemical reaction. Taking temperature into account in the calculations of atomic and molecular clusters properties is a novel and cutting-edge topic, given that its inclusion makes

the theoretical-computational results have the best agreement with experimental measurements. Currently, these methods are being developed and used in international research groups such as *Truhlar Research Group*, the group of Prof. Kieron Burke, and Cabellos's group. The inclusion of temperature requires dealing with the thermodynamics of nanoscopic systems or nanothermodynamics. Emphasizing low-energy structures and temperature plays a preponderant role in determining molecular properties. The calculations, the research topic, and the developed methodologies are original and cutting-edge. All the computer codes were developed and implemented during this doctoral thesis development. This doctoral thesis generates scientific knowledge on the fascinating subject of nanothermodynamics and highlights the importance of temperature in chemistry at theoretical level.

1.1.4 High temperature

The experimental studies are carried out in non-zero temperatures, and temperature is one of the parameters that can be manipulated (at a practical level) to observe novel reactions that do not occur at low temperatures. In accordance with Margrave *et al.* [4], *New molecules will be discovered and new theories required to explain events from 1000 to 1,000,000 K*. The term high temperature in chemistry refers to chemical phenomena which occur at temperatures of 1000 K and higher [4], volcanoes, lightning, and the sun and stars are examples of natural high-temperature sources where chemistry reactions happen in the range of hundreds to millions degrees of temperature. As temperature increases, chemical reactions are faster, and the chemical behavior differs from that found at room and cold temperatures. Dicyanoacetylene, a compound with chemical formula C_4N_2 burns with a flame at a temperature of 5260 K [5]. In this thesis, the computed thermal probabilities for low and medium, or below the melting point temperatures of Cu, Be, and B atomic clusters, can be reasonably described with a harmonic approximation. When the temperature increases enough, melted material may be present instead of a solid and the theory needs to be validated at hot temperatures. We must consider the anharmonic terms to describe the vibrations at high energies correctly. In this thesis, for the mentioned above, we consider temperatures around or below the melting point to capture the system's thermal behavior at high temperatures.

1.1.5 Organization of the thesis

The thesis is structured in seven parts as follows:

- Chapter 1, introduction and objetives.
- Chapter 2, the theory and methodology.
- Chapter 3, study of the $Be_6B_{11}^{-1}$ cluster.
- Chapter 4, study of the Be_4B_8 cluster.
- Chapter 5, study of the Cu_{13} cluster.

- Chapter 6, study of the Cu_{38} cluster.
- Chapter 7, conclusions and future work.

Chapter 2

Theory and methodology

2.1 Density functional theory

In the last 30 years the *Density Functional Theory*, is one of the most active topics in the area of materials science, chemistry and physics [6]. For reference point, the most notable article on DFT has been cited 128902 times [7] (18/12/2022), and one of the most cited scientists is *John P. Perdew* [7, 6]. The DFT applied in atoms, molecules and solids, is a variational procedure that solves the non-relativistic time-independent Schördinger Equation 2.1, considering many electrons and implemented in numerical methods and algorithms written in programming code, usually in *FORTRAN*.

$$\left[-\frac{\hbar^2}{2m}\frac{\partial^2}{\partial x^2} + V(x)\right]\Psi(x) = E\Psi(x), \tag{2.1}$$

In Eq. 2.1, $\hbar$ is the reduced *Planck* constant, m is the mass of the electron, V(x) is the external potential, E the *eigen*-energies and $\Psi(x)$ is the wave function associated to the state in which the system is located and contains all the information of the properties of it. The Hydrogen atom, a system with one electron, is one of the cases in which the solution of the Schördinger equation has an analytical solution, (the free particle is another) for multi-electron atoms the Schördinger equation has no solution with analytics, in the latter case finding the solutions is elaborate [8, 9]. Consequently, and in order to find a solution, DFT and/or other methods are used. The fundamental idea of DFT lies in the minimization of the total energy of the system with respect to the electron density of the ground state, instead of using the wave function. The DFT is a theory that adequately describes the properties of the ground state and its main advantage over methods that use the wave function is that the electron density depends only on the space coordinates x, y, z, contrary to the wave function, which has a large number of parameters. The first DFT was proposed by *Thomas* and *Fermi* [10, 11] in 1928, originally the model was proposed to study multielectron atoms. The foundations underlying modern DFT were published by *Peter Hohenberg* and *Walter Kohn* in their 1964 article [12], where they established that the energy is a functional of the density, that is to say, the energy is a function of the density and this is a function of the geometric coordinates, a function of functions. In their article[12] *Peter Hohenberg* and *Walter Kohn* showed that energy is a functional of electron density establishing the equation:

$$E[\rho] = E_{xc}[\rho] + \int \rho(\mathbf{r})\mathrm{v}(\mathbf{r})\mathrm{dr} \tag{2.2}$$

where $E_{xc}[\rho]$ is the functional that contains the kinetic energy and the energy due to the interaction electron-electron. The problem with DFT is that the exact form of the functional $E_{xc}[\rho]$ is not known. They also established that the electron density that minimizes the energy functional is the density of the ground state, the energy evaluated at that density is the energy of the ground state. In 1965 *Walter Kohn* and *Lu Jeu Sham* in their article[13] proposed the term correlation and exchange which includes the contributions of dynamic electronic correlation and the unknowns, which are not considered in the DFT. The resulting equations are known as *Kohn-Sham equations* and are the ones that are implemented, using different strategies in a variety of electronic structure codes. For the development of the thesis, we employed the DFT as it is implemented in the electronic structure code *Gaussian G09* [14] for the minimization of molecules.

2.2 Theoretical methods and computational details

2.2.1 Global minimum search

Despite advances in computing power, the minimum global search in molecular and atomic clusters remains a complicated task due to several factors. The exploration should be systematic and unbiased; [15, 16] a molecule's degrees of freedom increase with the number of atoms; [16, 17, 18, 19, 20] a molecule composed of N number of atoms possesses 3N degrees of freedom (i.e., a linear molecule has [3N-5] degrees of vibrational modes, whereas a nonlinear molecule has [3N-6] degrees of vibrational modes); and, as a consequence, the potential/free energy surface depends on a large number of variables. The number of local minima increases exponentially as a function of the number of atoms in the molecule. Moreover, the total energy computation requires a quantum mechanical methodology to produce a realistic value for energy. In addition to that, there should be many initial structures. It is essential to sample a large region of the configuration space to ensure that we are not missing structures, making an incomplete sampling of the configurational space and introducing a significant problem to calculating the thermodynamic properties [21]. A Complete sampling of the potential/free energy surface is nearly impossible, but a systematic exploration of the potential energy surface is extremely useful. Although searching for a global minimum in molecular systems is challenging, the design and use of algorithms dedicated to the search for global minima, such as simulated annealing [22, 23, 24, 25, 26, 27], kick method [1, 28, 3, 29, 30, 31, 32] genetic algorithms [33, 34, 35], Gradient Embedded Genetic Algorithm (GEGA) [36, 30, 37], and basin hopping [38, 39], has been accomplished over the years. In the past few years, a member of our research group designed and employed genetic algorithms [3, 28, 40, 41, 42] and kick methodology [43, 44, 45, 46, 47, 48, 49, 41] coupled with density functional theory to explore atomic and molecular clusters' potential energy surfaces. They have led us to solve the minimum global search in a targeted way. In this paper, our computational procedure employs a recently developed and unbiased hybrid strategy for a search methodology that combines a

modified-kick heuristic and genetic algorithm with density functional theory that has been implemented in the *GALGOSON* code. *GALGOSON* systematically and efficiently explores potential/free energy surfaces (PES/FES) of the atomic clusters to find the minimum energy structure. The methodology consists of a three-step search strategy where, in the first and second steps, we explore the PES, and in the third step, we explore the FES. First, the code builds a generation of random initial structures with an initial population of two hundred individuals per atom in the $Be_6B_{11}^-$ cluster using a kick methodology. The process to make 1D, 2D, and 3D structures is similar to that used in previous work. [42, 50] and are restricted by two conditions [42] that can be summarized as follows: a) All the atoms are confined inside a sphere with a radius determined by adding all atoms' covalent radii and multiplied by a factor established by the user, typically 0.9. b) The bond length between any two atoms are the sum of their covalent radii, modulated by a scale factor established by the user, typically close to 1.0; this allows us to compress/expand the bond length. These conditions avoid the high-energy local minima generated by poorly connected structures (too compact/ loose). Then, structures are optimized at the PBE0/3-21G level of theory employing Gaussian 09 code. As the second step, all energy structures lying in the energy range of 20 kcal/mol were re-optimized at the PBE0-GD3/LANL2DZ level of theory and joints with previously reported global minimum structures. Those structures comprised the initial population for the genetic algorithm. The optimization in this stage was at the PBE0-GD3/LANL2DZ level of theory. The criterion to stop the generation is if the lowest energy structure persists for 10 generations. In the third step, structures lying in 10 kcal/mol found in the previous step comprised the initial population for the genetic algorithm that uses Gibbs free energy extracted from the local optimizations at the PBE0-D3/def2-TZVP, taking into account the zero-point energy (ZPE) corrections. The criterion to stop is similar to that used in the previous stage. In the final step, the lowest energy structures are evaluated at a single point energy at the CCSD(T)/def2-TZVP//PBE0-D3/def2-TZVP level of theory. All the calculations were done employing the Gaussian 09 code. [51]

2.3 Thermochemistry properties

Classical thermodynamics describes large system's behavior; in contrast, nanothermodynamics is applied to small systems. The thermodynamics of macrosystems could apply to quantum systems. Nanothermodynamics were developed by Terrell Hill during the 1960 [52, 53, 54]. At temperatures different of zero, the Gibbs free energy determines the lowest-energy structure [55], whereas at temperature zero the enthalpy determines the putative global minimum [1, 2]. A simple analysis of the Gibbs free energy given by $\Delta G = \Delta H - \Delta ST$ deals to a conclusion, in order to minimize the Gibbs free energy we must to maximize the entropy [1, 2, 56]. Front the theoretical point of view, and first of all, with the aim to understand molecular properties, at non-zero temperatures, we must know the lowest Gibbs free energy

structure or the largest entropy structure, and all structures closest in energy to the lowest energy structure[1, 2] or all high-entropy structures closest in entropy to the largest. We must keep in mind that the experiments are performed at non-zero or finite temperatures. From a very general point of view, it has been shown that the validity of DFT can be extended to finite temperatures by the concept of ensemble DFT.[57]

2.3.1 Statistical thermodynamics

All the thermodynamic properties of an ensemble of molecules can be derived from molecular partition function [1, 2, 58] so, the molecular partition function contains all thermodynamic information in a similar way that the quantum wavefunction contains all the information about the system [1, 58]; In the statistical thermodynamics field the partition functions are central, and as I mentioned at the beginning of this chapter, it is an important function that allows us to compute all thermodynamic macroscopic properties [1, 59, 60, 61, 62]. Previous theoretical studies used the partition function to compute thermodynamic properties of Cu_n clusters (n=2, 150) as a function of temperature and demonstrated that the magic clusters are temperature dependent [63] Zhen Hua-Li *et al.* [64] computed the thermodynamics of unsupported neutral Al_n ($2 < n < 65$) particles evaluating rovibrational partition functions, they reported that the dominant cluster depends on temperature, and gives and overview of recent progress on the nanothermodynamics of metal nanoparticles [65]. Christopher Sutton *et al.* [56] in framework of atomistic thermodynamics predict the behavior of materials at realistic temperatures. Recently, Buelna-Garcia *et al.* [1, 2] used the partition function to compute the temperature-dependent relative population and IR spectra of neutral Be_4B_8 and anionic Be_6B_{11} clusters, also Dzib *et al.* [58] employed a similar procedure to compute the reaction rate constants. Other previous theoretical studies computed the temperature-dependent entropic contibutions on [Fe(pmea)(NCS)2] complex.[66] In this thesis, the temperature-dependent Gibbs free energy is computed employing the partition function Q given in Equation, 2.3 under approximations:

1. Harmonic oscillator (HO)
2. The rigid rotor (RR)
3. Ideal gas
4. Particle-in-a-box
5. Born-Oppenheimer (BOA)

We have to underline that RR and HO approximations employed to compute the partition function are **not accurate at high temperatures**, so, to compare theory with experiment [67], the anharmonicity must take into account.

$$Q(T) = \sum_i g_i \; e^{-\Delta E_i / K_B T} \tag{2.3}$$

In Eq. 2.3, g_i is the degeneracy factor, k_{B} is the Boltzmann constant, T is the temperature, and $-\Delta E_i$ is the total energy of a cluster [1, 58, 59]. An exact calculation of Q in Equation 2.3, could be complicated due to the coupling of the internal modes, a way to decouple the electronic and nuclei modes is through the use of Born-Oppenheimer approximation (BOA). This approach says that the electron movement is faster than the nuclei and assumes that the molecular wave function is the electronic and nuclear wavefunction product. $\psi = \psi_e \psi_n$ The vibrations change the momentum of inertia and, as a consequence, affects the rotations; this fact tightly couple the vibrational and rotational degrees of freedom; The separation of rotational and vibrational modes is called the rigid rotor (RR), harmonic oscillator (HO,RRHO) approximation, under this approximation, the molecule is treated rigidly, this is generally good when vibrations are of small amplitude[68]. Here the vibration will be modeled in terms of harmonic oscillator and rotations in terms of the rigid rotor within BOA and RRHO approximations, we point out that the RRHO breakdown for low frequencies modes, and one posible solution. There are two approximations to avoid the low frequencies modes: The Truhlar approximation[69, 2] which set up the low frequencies smaller than 100 cm^{-1} to a value of 100 cm^{-1} and the Grimme's approximation for low-lying frequencies known as free-rotor approximation[70]. In this thesis the low-lying frequencies are treated by the Truhlar approximation[69, 2].

2.3.2 The harmonic oscillator approximation

The vibrations of a molecule can be described employing harmonic oscillators, which follow the force Hooke's Law [68, 59], the vibrational energy levels are determinated by solving the Schrödinger Equation 2.4.

$$-\frac{\hbar}{2m}\frac{\partial^2\psi}{\partial x^2} - \frac{1}{2}kx^2 = E_v\psi \tag{2.4}$$

Where $\hbar$ os the Planck's constant, m mass of electron, and k is the Hooke's constant. The solution of Equation 2.4 is given by Equation 2.5

$$E_v = \left(n + \frac{1}{2}\right)\hbar\omega, \quad n = 0, 1, 2, 3\cdots \tag{2.5}$$

The vibrational energy levels are quantized, and with $n = 0$ apperars an energy level called zero point vibrational energy ($\mathcal{E}_{\mathrm{ZPE}}$) which is totally a quantum effect, and can be explained with the Heisenberg uncertainty principle. The harmonic potential is a good approximation only for low energies, and at higher energies anharmonicity appears and leads to the anharmonic vibrational problem that could be solved employing second-order vibrational perturbation theory (VPT2) [71, 72], so additional corrections should be done, as mentioned before and underlined here; We must consider the anharmonicity, with the aim of comparing theory with experiment[67].

2.3.2.1 $\mathcal{E}_{\text{ZPE}}$ energy correction

The Equation 2.6 gives the zero-point energy ($\mathcal{E}_{\text{ZPE}}$), where ν_i are all 3N-6 vibrational modes that the atomic cluster possesses. $\mathcal{E}_{\text{ZPE}}$ is a pure quantum effect and is due to the fact the Equation 2.5 for $n = 0$ it still retains a energy value at 0 K temperature.

$$\mathcal{E}_{\text{ZPE}} = \frac{\hbar c}{2\pi} \sum_{i=1}^{3N-6} \nu_i \tag{2.6}$$

In Equation 2.6, $\hbar$ is the reduced planck's constant, c is the velocity of light, and ν are the vibrational frquencies. The $\mathcal{E}_{\text{ZPE}}$ can be simply computed with the vibrational modes employing Equation 2.6 under the harmonic oscillator approximation and is the energy due to vibrational at zero K. The electronic energy ($\mathcal{E}_0$) plus $\mathcal{E}_{\text{ZPE}}$ energy g leads to the real total energy at 0 K ($\mathcal{U}_0$) given in Equation 2.7.

$$\mathcal{U}_0 = \mathcal{E}_0 + \mathcal{E}_{\text{ZPE}} \tag{2.7}$$

In this thesis, we establish that Equation 2.7 is the first thermodynamic correction.

2.3.3 The rigid rotor approximation

The simple model of the rigid rotor (RR) can be used to describe the rotational motion, a molecule constrained to rotate around an axis. The RR approximation considers that the atoms are connected by rigid bonds, so the molecule is a rigid object. The rotational energies, E_J are given by Equation 2.8

$$E_J = J(J+1)\frac{\hbar^2}{2I} \tag{2.8}$$

Where J is the rotational quantum number (J is for diatomic molecule, l for electron around nucleus) $J = 0, 1, 2, 3 \cdots$ $\hbar$ is the Planck's constant and I is the moment of inertia. Interesting for $J = 0$, there are not zero-point energy for rotations.

2.3.4 Ideal Gas

The ideal gas law is defined by the Equation 2.9 proposed by Horstmann [73]

$$PV = nRT \tag{2.9}$$

and relates thermodynamic variables, pressure, volume, temperature for a n number of gas moles. In Eqution 2.9, R is the universal gas constant, n the number of moles, P presion, V volume and T absolute temperature. There are two assumptions:

1. There are no forces acting among the particles.
2. The particles have not volume.

The ideal gas has only translational and electronic energies.

2.3.5 Particle-in-a-box

A particle-in-a-box is a quantum approximation that describes the translational motion of a single particle inside an infinitely potential well. The nonrelativistic Schrödinger wave equation for the case of a particle-in-a-box is given by Equation 2.10

$$-\frac{\hbar}{2m}\frac{\partial^2\psi}{\partial x^2} = E\psi \tag{2.10}$$

The solution to Equation 2.10 is given by Equation 2.11

$$E_n = \frac{\hbar^2 n^2 \pi^2}{2mL^2} \tag{2.11}$$

For the case in 3D Equation 2.11 leads to Equation 2.12

$$E_n = \frac{\hbar^2\pi^2}{2mL^2}(n_x^2 + n_y^2 + n_z^2) \tag{2.12}$$

Where n is the principal quantum number $n = 1, \infty$, L is the longitud of the box, m is the mass of electron, $\hbar$ is the normalized planck's constant.

2.3.6 Born-Oppenheimer

Considering that the nuclei is heavier than electrones, the first step in solving the nonrelativistic Schrödinger equation for molecular systems is fix the nuclear positions, which implies that the wavefunctions of nuclei and electrons can be treated separatley. On the one hand, there are cases where the BOA approximation breakdown [74] and on the other, BOA allows us to factorize the partition function Q (Equation 2.3) into its contributions. In this thesis, we establish that is not possible to compute the partition function by factorization, if we do not consider the BOA approximation [2]. The partition function is factorized into electronic, translational, vibrational, and rotational energies as is displayed in Equation 2.13. Consequently, the partition function, Q, (Equation 2.3) can be given as a product of the corresponding contributions [54, 58]

$$Q = q_{trans}\ q_{rot}\ q_{vib}\ q_{elec} \tag{2.13}$$

2.3.7 Translational partition function

Inserting, the quantum single particle-in-a-3D-box solution, Equation 2.12, into Equation 2.3, and computed the summation, the translation partition function is given by:

$$q_{trans} = V\left(\frac{2\pi K_B T}{\hbar^2}\right)^{\frac{3}{2}} \tag{2.14}$$

where m is the mass of the particle, V is the volume and T is the temperature. Employing the ideal gas equation, $PV = nRT$, Equation 2.14 can be rewritten as Equation 2.15.

$$q_{trans} = \frac{K_B T}{P}\left(\frac{2\pi K_B T}{\hbar^2}\right)^{\frac{3}{2}} \tag{2.15}$$

Where P is the pressure (1 bar), K_B is the Boltzmann constant. The term λ_D given in Equation 2.16 is known as thermal Broglie wavelength

$$\lambda_D = \left(\frac{2\pi K_B T}{\hbar^2}\right)^{\frac{3}{2}} \tag{2.16}$$

2.3.8 Vibrational partition function

The vibrational energy for a vibrational mode is given by the solution of Equation 2.4 with solution given in Equation 2.5, inserting Equation 2.5 into Equation 2.3 leads to Equation 2.17b that describe the vibrational partition function for one vibrational mode,

$$q_{vib} = \sum_{i=0}^{\infty} e^{\frac{h\nu\left(n+\frac{1}{2}\right)}{K_B T}} \tag{2.17a}$$

$$= \frac{e^{-\frac{h\nu}{2K_B T}}}{1 - e^{-\frac{h\nu}{2K_B T}}} \tag{2.17b}$$

The total vibration of a molecule is given by the summation of independent harmonic oscillators, considering that a non-linear molecule has (3N-6) vibrational modes (n_ν), the vibrational partition function is given in Equation 2.18a

$$q_{vib} = \prod_{i=1}^{n_\nu} \frac{e^{-\Theta_{\mathrm{vib}_i}/2T}}{1 - e^{-\Theta_{\mathrm{vib}_i}/T}}, \Theta_{\mathrm{vib}_i} = \frac{h\nu_i}{k_{\mathrm{B}}}, \tag{2.18a}$$

2.3.9 Rotational partition function

The energy of a single rotational degree of fredom is given by Equation 2.8 that is the solution of Schrodinger Equation for vibrational modes. Inserting Equation 2.8 into Equation 2.3 leads to Equation 2.19b

$$q_{rot} = \sum_{\mathcal{L}=1}^{\infty} (2\mathcal{L}+1) e^{-\frac{\hbar^2 \mathcal{L}(\mathcal{L}+1)}{2IK_B T}} \tag{2.19a}$$

$$= \sum_{\mathcal{L}=1}^{\infty} (2\mathcal{L}+1) e^{-\frac{\Theta \mathcal{L}(\mathcal{L}+1)}{K_B T}} \tag{2.19b}$$

with Θ given by Equation 2.20

$$\Theta = \frac{\hbar^2}{2I} \tag{2.20}$$

The approximate summation of the Equation 2.19b leads to rotational partition function for linear molecules, and is given by Equation 2.21

$$q_{rot} = \frac{K_B T}{\sigma \Theta} \tag{2.21}$$

Where σ is the symmetry number. For non-linear molecules the rotational partition function is given by Equation 2.22

$$q_{rot} = \frac{1}{\sigma}\left(\frac{\pi(K_B T)^3}{\Theta_A \Theta_B \Theta_C}\right)^{1/2} \tag{2.22}$$

Where Θ_A,Θ_B, and Θ_C are the rotational constants, one for each dimension. In summary, Equations 2.23 are the contributions of electronic (2.23e), translational (2.23a), vibrational (2.23d),and rotational (2.23b,2.23c) to the canonical partition function. Contributions to the canonical partition function

$$q_{trans} = ((\frac{2\pi m k_{\mathrm{B}} T}{h^2})^{\frac{3}{2}} \frac{k_{\mathrm{B}} T}{P}, \tag{2.23a}$$

$$q^{l}_{rot} = \frac{1}{\sigma_r}(\frac{T}{\Theta_r}), \tag{2.23b}$$

$$q^{nl}_{rot} = \frac{\pi^{1/2}}{\sigma_r}\left(\frac{T^{3/2}}{(\Theta_{\mathrm{A}}\Theta_{\mathrm{B}}\Theta_{\mathrm{C}})^{1/2}}\right), \Theta_{\mathrm{i}} = \frac{\hbar}{2\mathrm{I}_i k_{\mathrm{B}}}, i = \mathrm{A}, \mathrm{B}, \mathrm{C}, \tag{2.23c}$$

$$q_{vib} = \prod_{i=1}^{n_\nu} \frac{e^{-\Theta_{\mathrm{vib}_i}/2T}}{1 - e^{-\Theta_{\mathrm{vib}_i}/T}}, \Theta_{\mathrm{vib}_i} = \frac{h\nu_i}{k_{\mathrm{B}}}, \tag{2.23d}$$

$$q_e = \omega_0, \tag{2.23e}$$

2.3.10 Internal energy and entropy

The internal energy, U is given by Equation 2.24

$$U = K_B T^2 \left(\frac{\partial In(Q)}{\partial T}\right) \tag{2.24}$$

The K_B is the Boltzmann constant, T is the absolute temperature, the entropy can be computed emplying the Equation 2.25

$$S = K_B T + In(Q) + K_B T^2 \left(\frac{\partial In(Q)}{\partial T}\right) \tag{2.25}$$

The internal energy is composed of terms given in Equation 2.26

$$U = U_{trans} + U_{rot} + U_{vib} + U_{elec} \tag{2.26}$$

The entropy is composed of terms given in Equation 2.27

$$S = S_{trans} + S_{rot} + S_{vib} + S_{elec} \tag{2.27}$$

We employ equations 2.26,2.28,2.29 to compute the total internal energy (U_T), enthalpy (H), and Gibbs energy (G) of the atomic cluster at finite temperature employing Equations 2.30,2.31. The equations to compute entropy contributions (S) is Equation 2.27 and those employed in a previous work [55, 1, 2] and any standard thermodynamics textbook [59, 54].

$$\mathcal{U}_0 = \mathcal{E}_0 + \mathcal{E}_{\mathrm{ZPE}} \tag{2.28}$$

$$U_T = \mathcal{U}_0 + (E_{rot} + E_{trans} + E_{vib} + E_{elect}) \tag{2.29}$$

$$H = U_T + RT \tag{2.30}$$

$$G = H - TS \tag{2.31}$$

In Equations above, $\mathcal{E}_{\mathrm{ZPE}}$ is the zero-point energy correction, $\mathcal{E}_0$ is the electronic energy, and $E_{rot} + E_{trans} + E_{vib} + E_{elect}$ are the contributions to energy due to translation, rotation, vibration and electronic partitions as function of temperature, respectively. To compute the Boltzmann probability of occurrence of one particular neutral Cu_{38} cluster in an ensemble at thermal equilibrium and at finite temperatures, we employ the probability of occurrence [1, 2, 64, 75, 76, 77, 58, 78, 79, 63, 64] given in Equation 2.32

$$P_i(T) = \frac{e^{-\beta \Delta G^k}}{\sum e^{-\beta \Delta G^k}}, \tag{2.32}$$

where $\beta = 1/k_{\mathrm{B}}T$, and k_{B} is the Boltzmann constant, T is the temperature, and ΔG^k is the Gibbs free energy of the kth isomer. We point out that Gibbs free energies must be corrected considering the symmetry, Buelna-Garcia *et al.* [2] in a previous work shows that the contribution of the rotational entropy to the Gibbs free energy calculated with and without symmetry behave linearly with the temperature and could be significant [55] Equation 2.32 is restricted so that the sum of all probabilities of occurrence, at fixed temperature T, $P_i(T)$ is equal to 1 and given by Equation 2.33

$$\sum_i P_i(T) = 1, \tag{2.33}$$

2.4 Chirality

The term chiral was coined by W. H. Thompson in 1884 and came from the Greek word for hand (*cheir*) [80]. Lord Kelvin wrote: *I call any geometrical figure, or group of points, chiral, and say that it has chirality, if its image in a plane mirror, ideally realized, cannot be brought to coincide with itself* [81] A chiral molecule cannot be superimposed on its mirror image by any translation and rotation on the plane. These two, L- and R-structures, are called enantiomers, which have identical chemical and physical properties, such refractive index, melting point, infrared spectrum among others. Figure 2.1 shows the most familiar example of chiral. Chi-

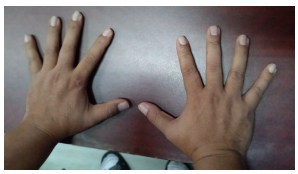

Figure 2.1: A chiral example, the hands

rality depends on symmetries, C_1, C_n and D_n are the chiral point groups and any chiral molecule must belong to any of these groups [81]. Particularly, the chirality

of nanoclusters has attracted attention due to their chiroptical properties, potential application in efficient chiral discrimination [82, 83], nonlinear optics [84] and chiral materials with interesting properties, [85, 86, 87] and of course, not to mention that chiral structures play a decisive role in biological activity [88]. Another system with chiral structures, the lowest energy structures of Au_{28} and Au_{55} are chiral [89]. In this study, two systems were found chiral, the Cu_{13} and Be_4B_8.

2.5 Chemical bonds

Chemical bonds are related to electron sharing between atoms [90], and they are not observable quantities. The chemical bond is a model to describe how atoms link to one another to build a molecule or solid and involve the atom connectivity concept. From the theoretical point of view, the physical interactions responsible for the cohesion of molecules can be studied by quantum chemistry. The definition of bond is ***A bond is considered to exist when two adjacent atoms are so located that the potential energy is a minimum, and when appreciable energy must be supplied to cause the atoms to separate*** [91]. There are some principles that must be observed:

1. The Helium atom and the atoms that have eight electrons in the frontier orbital can not form a chemical bond (neon, argon, krypton, xenon, and radon).

2. All atoms of the periodic table can form a chemical bond (except group 18).

3. Bonds are formed by sharing electrons by two or more atoms

When a chemical bond is formed between two atoms, the energy of the system must be decreased. Basically there are two types of chemical bonds

1. Ionic bonding, which implies complete transfer of electrons from one atom to another (NaCl).

2. Covalent bonding, in which there is share of electrons between atoms (H_2).

There are others types of bonding:

1. Metallic bonds are formed by atoms with low ionization energy and the attraction between delocalized electrons and positive ions (Ag).

2. Hydrogen bonds are an intermolecular interaction that forms a type of dipole-dipole attraction, and they are indicated by $\cdots$

3. Van der Waals (vdW) bond, the International Union of Pure and Applied Chemistry (IUPAC), defines a Van der Waals bond as: *The attractive or repulsive forces between molecular entities (or between groups within the same molecular entity) other than those due to bond formation or to the electrostatic interaction of ions or of ionic groups with one another or with neutral molecules.*

Table 2.1 displays the typical bonding energies for different bonding types and compounds. In this thesis we employed the adaptive natural density partitioning (AdNDP) method to study the bonding in Cu_{13} and Be_4B_8 clusters. The AdNDP employs the concept of the electron pair as central part of chemical bonding models [92]. It represents the electronic structure in terms of n-center two electrons (nc-2e) bond, where n are the number of atoms. The natural bond orbitals (NBOs) create the closet Lewis structure for a given structure, and they provide a valence bond-type of the quantum wavefunction in terms of the Lewis theory. From a computational point of view AdNDP is a generalization of NBO analysis by Weinhold [92], thus, the AdNDP method explains the bonding employing the quantum wavefunction in terms of the simple theory of Lewis. The AdNDP analyses the first-order reduced density matrix and recovers Lewis bonding (1c-2e or 2c-2 e, i.e., lone pairs (LPs) or two-center two-electron bonds) and delocalized bonding elements (associated with the concept of electron delocalization. The AdNDP analysis for chiral putative low-energy structures of B_4B_8 and Cu_{13} are displayed in Figure 4.2, and Figure 5.2, respectively.

Table 2.1: Bonding energies

Bonding type	Substance	Bonding energy (kcal/mol)
Ionic	NaCl	193 (E) [93]
Covalent	C	170 (E) [94]
Metallic	Fe	98 (E) [95]
van der Waals	vdW-bonded organic molecule dimers	0.5 (T) [96]
Hydrogen bond	Isolated bond	5-6 (E) [97]
	Proteins in solution	0.5-1.5 (E) [97]

2.6 Applications of atomic clusters

In the chemistry field, the term *clusters* or *atomic clusters*, is used to describe a collection of atoms or molecules. Atomic clusters are ideal to study catalysis and provide fundamental understanding about the catalytic processes, there are several applications of atomic clusters, among them:

- Mechanisms of CO oxidation [98]
- CO_2 conversion
- Dehydrogenation
- Hydrogenation
- Electrochemical water splitting

The IUPAC, defines a cluster as: *A number of metal centres grouped close together which can have direct metal bonding interactions or interactions through a bridging*

ligand , but are not necessarily held together by these interactions. On the other hand, a nanoparticle is a particle with dimensions in the 1$\tilde{1}$00 nm range, and they can be extended to 500 nm [99]. A nanocluster is a collection of a few atoms. In this doctoral thesis, we employed the term *Nanoclusters* because our systems are composed of few atoms.

Chapter 3

The $Be_6B_{11}^-$ cluster.

3.1 Abstract

The starting point to understanding cluster properties is the putative global minimum and all the nearby local energy minima; however, locating them is computationally expensive and challenging due to the degrees of liberty associated with the molecule rise as a function of the number of atoms. Therefore, the number of possible combinations increases exponentially, leading to a combinatorial explosion problem. The relative populations and spectroscopic properties of a molecule that are a function of temperature can be approximately computed by employing statistical thermodynamics. Here, we investigate entropy-driven isomers distribution on $Be_6B_{11}^-$ clusters and the effect of temperature on their infrared spectroscopy and relative populations. We identify the vibration modes possessed by the cluster that significantly contribute to the zero-point energy. A couple of steps are considered for computing the temperature-dependent relative population: First, using a genetic algorithm coupled to density functional theory, we performed an extensive and systematic exploration of the potential/free energy surface of $Be_6B_{11}^-$ clusters to locate the putative global minimum and elucidate the low-energy structures. Second, the relative populations temperature effects are determined by considering the thermodynamic properties and Boltzmann factors. The temperature-dependent relative populations show that the entropies and temperature are essential for determining the global minimum. We compute the temperature-dependent total infrared spectra employing the Boltzmann factor weighted sums of each isomer's infrared spectrum and find that at finite temperature, the total infrared spectrum is composed of an admixture of infrared spectra that corresponds to the spectrum of the lowest energy structure and its isomers located at higher energies. The methodology and results describe the thermal effects in the relative population and the infrared spectra.

3.2 Introduction

In recent years, the pure boron clusters, the metal, and non-metal doped boron clusters, have attracted considerable attention [1, 2, 100, 101, 102, 103, 104, 105, 106, 107, 42, 28] due to their unpredictable chemistry [108, 109] and high potential to form novel structures [110]. Boron is the smallest and lightest semi-metal atom [107, 111] and a neighbor of carbon in the periodic table. It has electron deficiency [112, 113, 114, 110] and a high capacity to combine and form novel atomic and molecular boron structures that are planar and quasi-planar [115, 86, 116] It

can also form nanotubes [117, 110], borospherenes [118, 102, 119], borophene [102], cages [120], chiral helices [121, 3] and nanosheets [115, 122] consisting of triangle units of boron atoms. Boron can absorb neutrons that make it useful in nuclear and medical applications [123, 124, 125]. Aromaticity, antiaromaticity, and conflicting aromaticity dominate the chemical bonding in boron-based clusters [126, 127, 121, 128]. The two most-used indices for quantifying aromaticity are the harmonic oscillator model of aromaticity, based on the geometric structure, and the nucleus-independent chemical shift, based on the magnetic response. Aromaticity is not observable, cannot be directly measured [129], and it correlates with electronic delocalization [130]. However, with applications in molecular devices, the dynamic structural fluxionality in boron and boron-doped based molecular systems is due to electronic delocalization [121, 131]. Moreover, electronic localization/delocalization contributes significantly to stability, magnetic properties, and chemical reactivity [129]. Nowadays, dynamic structural fluxionality in boron nanoclusters is a topic of interest in nanotechnology [119, 132]. The fluxionality of an atomic cluster is highly relevant in terms of its catalytic activity [133], and in boron-based nanoscale rotors, it is a function of the atomic structure, size, bonding, and cluster charge [134]. Moreover, doping a boron cluster with metals [135, 103, 136, 105, 137, 138, 139] and non-metals [140] dramatically affects its structure, stability, and reactivity, as with the shut-down in the fluxionality of the boron-doped anion B_{19}^- [141]. It is important to mention, the emission of radiation as a competing cooling channel has to be considered in studying small cationic boron clusters' stabilities. Accordingly to Ferrari *et al.*, this improving agreement between experiment and theory [142].

In this chapter, we consider that temperature and entropy are critical in elucidating the low-energy structures and highlight the importance of understanding the thermal and entropic effects in the $Be_6B_{11}^-$ fluxional cluster. In the past years, a boron molecular Wankel motor [143, 144, 101, 145, 146, 147] and subnanoscale tank treads have been reported [148, 149]; however, the entropic and temperature terms have not been considered. In collaboration with Merino's group and Zhai's group, some of us studied and reported fluxionality in $Be_6B_{11}^-$ [3]. The computations indicated that there were two competitive low-energy structures: a helix-type cluster and a fluxional coaxial multiple-layered cluster. More recently, another lowest-energy structure was found in the $Be_6B_{11}^-$ cluster by employing a cellular automaton algorithm. [50] However, the putative global minimum energy structure and its molecular properties depend strongly on the temperature-entropy term [16, 63, 150, 151, 152].

In several previous works, one of the authors computed the barrier energy in a chemical reaction by taking into account the effect of temperature-entropy term [58], computed the temperature-dependent dipole moments for the $HCl(H_2O)_n$ clusters [46], computed the temperature-dependent linear optical properties of the Si(100) surface [153], and more recently, it was considered in a study of gold clusters [79, 154, 78] and the thermochemical behavior of the sorghum molecule [77]. Nevertheless, most theoretical density functional studies assume that the temperature is zero and neglect temperature-dependent and entropic contributions; conse-

quently, their finite temperature properties remain unexplored [155, 156], whereas experimental studies are carried out in non-zero temperatures. Thus, it is necessary to understand the effect of the temperature on the cluster properties and the lowest energy structure's determination [155, 156]. Herein, we investigate the effect of temperature-entropy term on the relative population and its infrared spectra, which need the putative elucidation global minimum and its low-energy isomers [21, 157, 16]. The first starting point requires a minimum global search on the potential/free energy surfaces, which is a complicated task. Taking temperature into account requires dealing with small systems' thermodynamics; The Gibbs free energy of classical thermodynamics also applies for small systems, known as thermodynamics of small systems [158, 53, 159] or nanothermodynamics [65]. The thermodynamics of clusters have been studied by various theoretical and simulation tools [16, 52, 158, 160, 161, 162, 163, 155, 164, 165] like molecular-dynamics simulations [106], Monte Carlo, and analytic methods. Under the harmonic superposition approximation, the temperature-entropy term can be computed with the vibrational frequencies on hand. The entropy effects have been considered for gold, copper, water, and sodium clusters [154, 78, 79, 166, 63, 167, 168, 169, 170, 171]. As the second step for understanding cluster properties relies on the cluster's spectroscopy, spectroscopy gives insight into the structure and detects structural transformations in clusters [172, 173, 174]. The temperature effects on IR spectra have been studied experimentally and theoretically on small and neutral gold clusters [154, 79] and boron cluster [146]. In the same direction, the pristine Au_{13} gold cluster's thermodynamical stability at finite temperature was studied using the replica-exchange method, which shows a fluxional behavior [166]. Au_N clusters thermodynamics properties ($30 < N < 147$) were studied employing the Gupta potential and DFT methodology [78] The total absorption spectra were computed as the sum of the different spectra of different isomers [175].

In this chapter will employ statistical thermodynamics to compute the Gibbs free energy entropic-temperature-dependency, evaluate relative populations as function of temperature, and take into account the effects of temperature on the IR spectra. We also identify the vibration modes that make a significant contribution to the zero-point energy of the cluster that is strongly dominated at temperatures higher than 377 K, and also we show this structure poses the shortest B-B bond length. We investigate the effect of long-range van der Waals interactions on solid-solid transformation points; moreover, we found the vibrational modes responsible for the fluxionality of the cluster. Adicionally, we computed the relative population at single point CCSD(T) level of theory. We believe that this yields useful information about which isomers will dominate at hot temperatures. No work has been attempted to investigate temperature-entropy driven isomers in the fluxional $Be_6B_{11}^-$ cluster as far as we know. The rest of the chapter discusses the lowest energy structures, energetic ordering at DFT/CCSD(T) level of theory, the relative population, and IR spectra taking into account the temperature-entropy term.

3.3 Computational Details

3.3.1 Boltzmann Population

The properties observed in a molecule are statistical averages over the ensemble of geometrical conformations or isomers accessible to the cluster [176]. So the molecular properties are ruled by the Boltzmann distributions of isomers that can change due to temperature-entropic term [46, 177, 63], and the soft vibrational modes that clusters possess make primary importance contributions to the entropy [169]. The relative populations of the low-energy isomers of the cluster $Be_6B_{11}^-$ are computed through the probabilities defined in Equation 3.1

$$P(T) = \frac{e^{-\beta \Delta G^k}}{\sum e^{-\beta \Delta G^k}}, \tag{3.1}$$

where $\beta = 1/k_B T$, and k_B is the Boltzmann constant, T is the temperature in Kelvin, ΔG^k is the Gibbs free energy of the kth isomer. Equation 3.1 establishes that the distribution of molecules will be among energy levels as a function of the energy and temperature. It is worth mentioning that the energy of separation among isomers (energy gap between two isomers) is determinant in the computation of the solid-solid transition, T_{ss} point. T_{ss} occurs when two competing structures are energetically equaled, and there is simultaneous coexistence of structural isomers at T. In other words, the T_{ss} point is a function of the energy difference between two isomers and the energy ΔG that the cluster posses. Boltzmann distribution finds a lot of applications as to native protein structures [76] for a microscopy system, a temperature T or like method simulated annealing applied to the search of structures of minimum energy, rate of chemical reaction [58], sedimentation, among others. For the calculation of the Gibbs free energies at temperature T and the relative populations, we used a homemade *Python/Fortran* code called Boltzmann-Optics-Full-Ader (BOFA).

3.3.2 IR Spectra

The vibrational spectra are useful for identifying phases and determining structures [178], among other applications mentioned above. In this study, the IR harmonic spectra for each isomer were calculated employing Gaussian code [51]. All isomers were characterized as minima because we found no negative frequencies in each isomer. The Lorentzian line shape, with a width at half maximum of 20 cm^{-1}, and a scaling factor of 0.98 were used to compute the IR spectra for each isomer. The most considerable contribution to total IR spectra is the putative global minimum atomic structure [175], while the isomers located at high energies contribute little to the molecular properties. Therefore, the total IR spectrum is dependent on the temperature results from the contributions of all IR spectra weighted according to their relative populations. In this chapter, to obtain the total IR spectrum at temperature T, we weighted the IR spectrum of each isomer according to the prob-

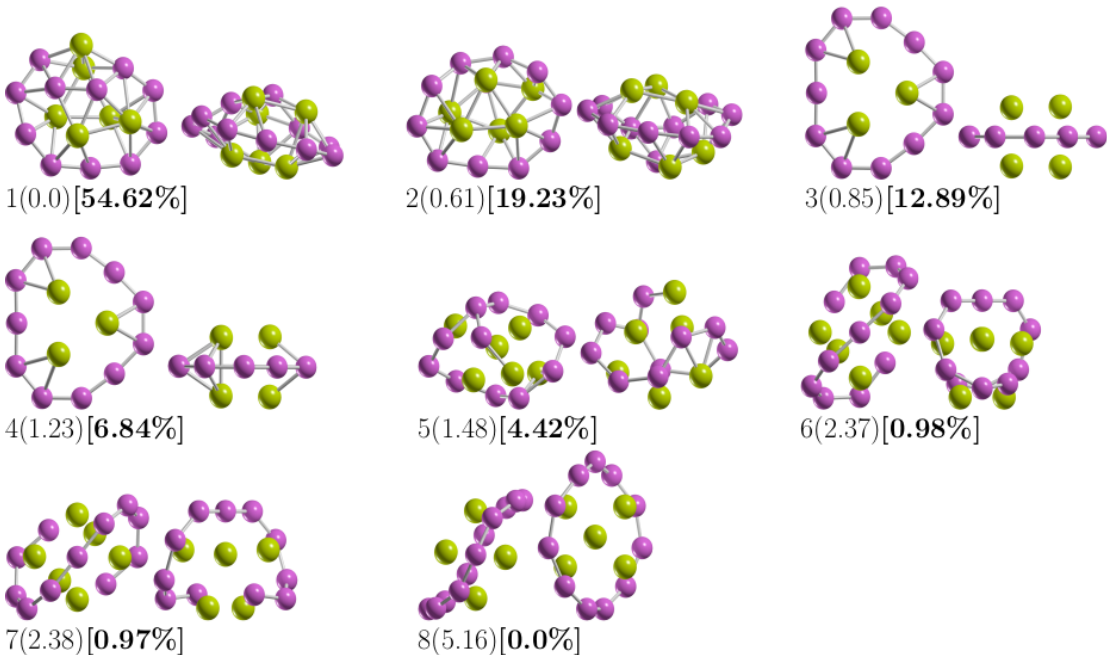

Figure 3.1: The optimized geometries of $Be_6B_{11}^-$ cluster.

abilities computed in Equation 3.1 and the sum of all of them; thus, we computed the total IR spectrum as a function of the temperature.

The global exploration of the potential and free energy surfaces of the $Be_6B_{11}^-$ was done with a hybrid genetic algorithm written in Python. All local geometry optimization and vibrational frequencies were carried out employing the density functional theory (DFT) as implemented in the Gaussian 09 [51] suite of programs, and no restrictions in the optimizations were imposed. Final equilibrium geometries and relative energies are reported at PBE0 [179]/def2-TZVP [180] level of theory, taking into account the D3 version of Grimme's dispersion corrections [181], and including the zero-point (ZPE) energy corrections. (PBE0-D3/def2-TZVP) As Pan *et al.* [182] reported, the computed relative energies with PBE0 functional are very close to the CCSD(T) values in B_9^- boron cluster. The def2-TZVP basis set from the *Ahlrichs* can improve computations accuracy and describe the $Be_6B_{11}^-$ cluster [3]. To gain insight into its energetics, we evaluated the single point energy at CCSD(T)/def2TZVP//PBEO-D3/def2-TZVP level of theory for the putative global minima and the low-energy isomers. The total IR spectra dependent on temperature are computed employing Boltzmann weighted sum of the IR spectra of each isomer, and the relative populations using Boltzmann factors, both of them implemented in a made in home Python/Fortran code called BOFA. The BOFA code is employed in the computation of the relative population and weighted IR spectra.

3.4 Results and Discussion

3.4.1 The lowest energy structures and energetics

We show in Figure 3.1 the lowest energy structure of $Be_6B_{11}^-$ clusters and seven low-energy competing isomers computed at the PBE0-D3/def2-TZVP level of theory. The criterion for drawing the structures is until the percentage of the relative population is zero. The relative Gibbs free energy is given in kcal/mol (round parenthesis) and computed at 298.15 K and 1 bar. In square parenthesis, and in bold is given the percentage of the relative population computed employing Equation 3.1 at 298.15 K. For the putative global minimum at the PBE0-D3/def2-TZVP level of theory, the optimized average B-B bond length is 1.64 Å. In contrast, the optimized B-Be bond length is 2.01 Å. To observe the trend in B-B bond length in the low-energy

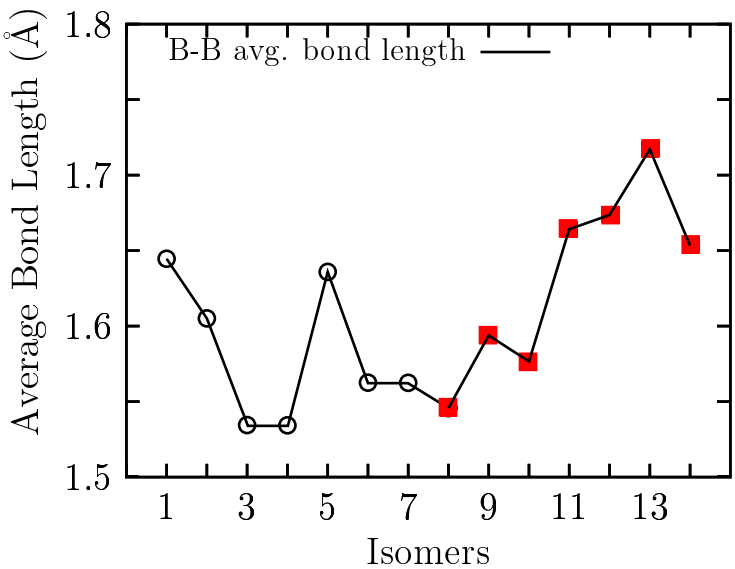

Figure 3.2: The average B-B bond length a function of the number of isomers.

structures, Figure 3.2 shows the average bond length for B-B for the fourteen lowest energy isomers energetically accommodated, from the most energetically favorable, isomer number 1, to the least stable, isomer number 14. Our calculations indicated that the largest average value of the B-B bond length is 1.71 Å and belongs to isomer number 13, which is 25 kcal/mol less stable than the putative global minimum. The lowest average value of the B-B bond length is 1.53 Å and corresponds to the isomers coaxial triple-layered structures with C_s and C_{2v} symmetries, located at energies of 0.85 and 1.23 kcal/mol above the putative global minima, respectively. The structures are depicted in Figure 3.1(3)(4). In these structures, the lowest average B-B bond length of 1.53 Å is considerably shorter compared with the: (a) length of a typical B-B single bond of 1.72 Å [183], (b) the bond length of the B8 and B_9^- molecular wheels [184, 3], and slightly shorter in 2.2% than the B-B double

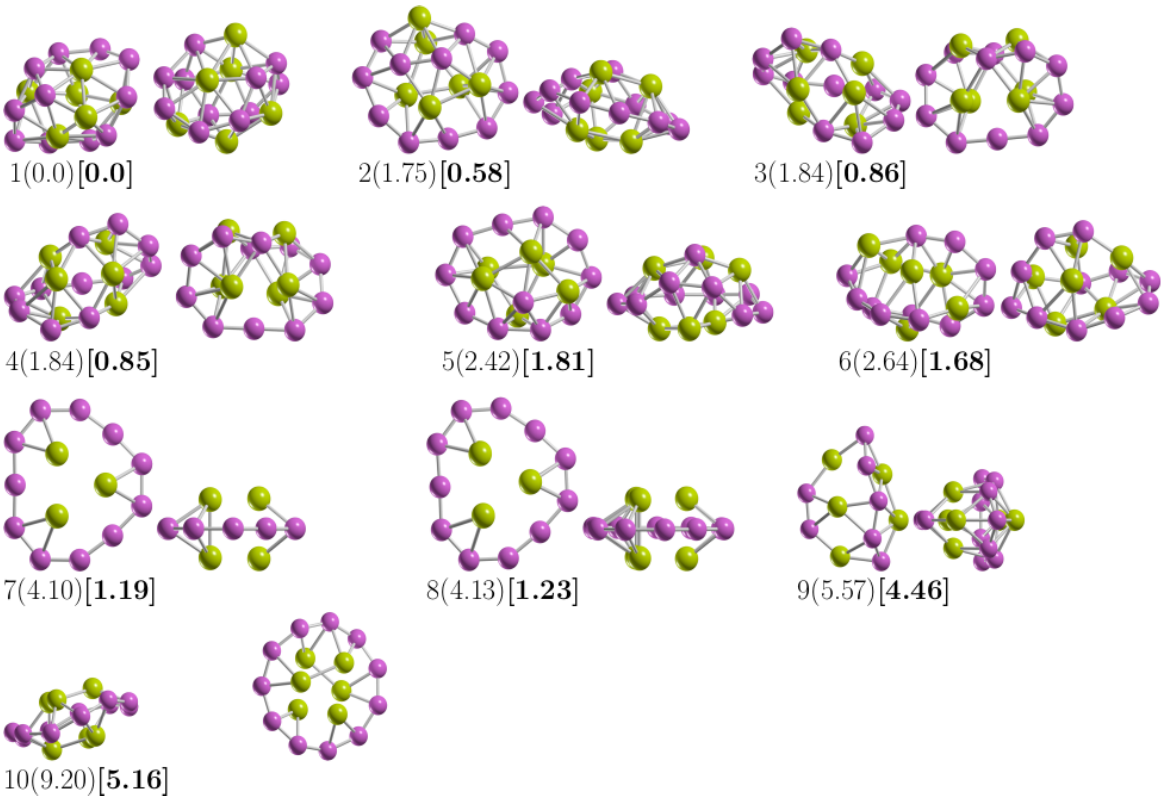

Figure 3.3: The most important energy isomers shown in two orientations, rotated 90 degrees up to plane paper and front.

bond length experimentally characterized in the range of 1.57-1.59 Å [185, 186]. The average B-B bond length shortens from 1.64 Å to 1.53 Å , suggesting strong hyperconjugation in the coaxial triple-layered structures. The shortening of the B-B bond length is caused by orbital interaction, which is also a cause of C-C bond shortening in the Butyne molecule. [187] Hyperconjugation has been shown in the shortening of B-B and C-C bond lengths [188, 187] and which causes increases in the number of electrons shared between region. Figure 3.4 shows the average bond length for Be-B for the 14 low-energy isomers. The largest average value of the Be-B bond length is 2.0 Å and 2.10 Å, which correspond to the isomer coaxial triple-layered structures with C_s and C_{2v} symmetries, respectively. This suggests that if the shortening of the bond length increases the number of electrons shared in that region [187], the increase in bond length should decrease the number of electrons; consequently, the electron delocalization occurs in the ring of boron atoms. In Figure 3.1(1), is depicted the putative global minimum with 54% of the relative population, and it has C_1 symmetry with a singlet electronic state ^{1}A. It is a distorted, oblate spheroid with three berylliums atoms in one face and two in the other face. Nine boron and one beryllium atoms form a ring located around the spheroid's principal axes, and the remaining two boron atoms are located close to the boron ring on one of its

faces. The second higher energy structure, at 298.15 K, lies at a Gibbs free energy of only 0.61 kcal/mol above the putative global minimum; it has C_1 symmetry with a singlet electronic state ^{1}A. It is a prolate spheroid with 19% of the relative population at a temperature of 298.15 K. The next two higher energy isomers, at 298.15 K, are located at 0.85 and 1.23 kcal/mol Gibbs energy above the putative global minimum. They are prolate, coaxial, triple-layered structures with C_s, and C_{2v} symmetries and singlet electronic states ^{1}A and $^1A_1$, respectively. This clearly shows that the low-symmetry structure C_s becomes energetically preferred compared to the C_{2v} symmetry, with a Gibbs free energy difference of 0.38 kcal/mol at 298.15 K due to the entropic effects. This is in agreement with a similar result found in Au_{32} [15]. According to our computations, those structures are strongly dominant at temperatures higher than 377 K. The next structure shown in Figure 3.1(5) is located 1.48 kcal/mol above the global minimum; it is close to spherical in shape and corresponds to a prolate structure with C_1 symmetry and a singlet electronic state ^{1}A. This structure makes up only 4.4% of the relative population at 298.15

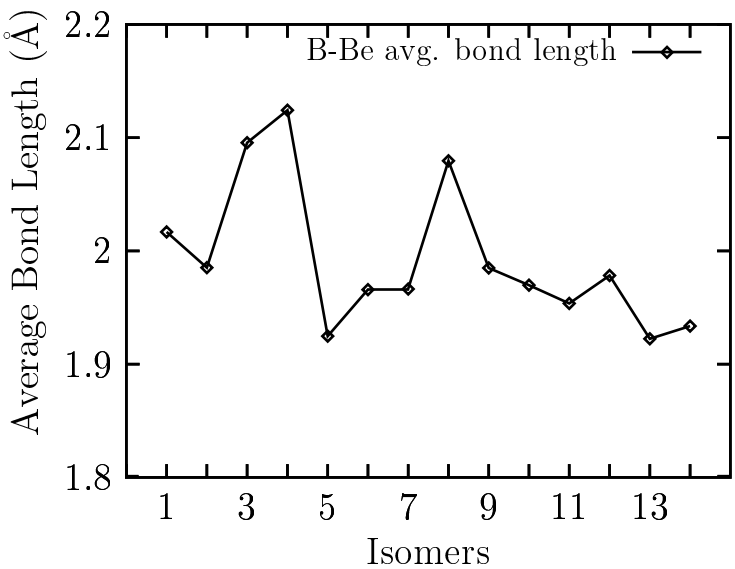

Figure 3.4: The average Be-B bond length a function of the number of isomers.

K. The next two structures, located at a Gibbs free energy of 2.37 kcal/mol above the global minimum, are the chiral helix-type structures. These were previously reported by Guo *et al.* [3] as the global minimum and also found with *GALGOSON* code. They are prolate structures with C_{2v} symmetries and their relative population is around only 1%. We note that the chiral-helix structures are never the lowest energy structures throughout the entire temperature range. The relative population is zero for structures located at relative Gibbs free energies higher than 5.1 kcal/mol, and at 298.15 K, there is no contribution of these isomers to any total molecular property. A full understanding of the molecular properties requires the search for the global minimum and all its closest low-energy structures [21]. The separation

among isomers by energy difference is an important and critical characteristic that influences the relative population and, consequently, the overall molecular properties. To gain insight into how the energy difference among isomers changes and how the energy ordering of the low-energy structures is affected. We computed the putative global minima and the first seven low-energy structures a single point energy at the CCSD(T)/def2-TZVP level of theory corrected with the zero-point energy computed at the PBE0 D3/def2-TZVP level of theory. Figure 3.3 shows the isomers energetic-ordering considering CCSD(T) energy in kcal/mol in parentheses, and the corrected in kcal/mol in square brackets. At the CCSD(T) level of theory, the global minimum, the seven lowest energy isomers, and the energy order agree with those in a previous work [50], as shown in the first row of Table. 3.1 The second row of Table 3.1 shows the corrected Interestingly, the energetic ordering of isomers does not change when considering the ZPE. Nevertheless, the energy-differenece among

Table 3.1: The relative energies in kcal·mol^{-1}, coupled cluster single-double and perturbative triple.

		Isomers						
$Be_6B_{11}^-$	Level	i_1	i_2	i_3	i_4	i_5	i_6	i_7
	CCSDT	0.0	1.75	1.84	1.84	4.10	4.13	2.64
	CCSDT+$\mathcal{E}_{\text{ZPE}}$	0.0	0.58	0.85	0.86	1.19	1.23	1.68
	ΔG	0.0	-1.48	0.89	0.88	-0.63	-0.25	4.14
	$\mathcal{E}_0 + \mathcal{E}_{\text{ZPE}}$	0.0	-0.29	1.51	1.52	2.41	2.42	5.0
$Be_6B_{11}^-$	$\mathcal{E}_0$	0.0	0.87	2.50	2.50	5.32	5.32	5.96
	Point group symmetry	C_1	C_1	C_2	C_2	C_s	C_{2v}	C_1
	Electronic ground state	^{1}A	^{1}A	^{1}A	^{1}A	^{1}A'	^{1}A$_1$	^{1}A
	Frequencies	230	119	102	100	46	43	161

isomers were reduced drastically. For example, the energy difference between the first and second isomers was reduced by 66%, from 1.75 to 0.58 kcal/mol; the energy difference between the second and third isomers was increased almost 300%, from 0.1 to 0.27 kcal/mol, as shown in rows one and two of Table 3.1, respectively. This change (increase/decrease) in energy difference among isomers has an enormous impact on the relative population. Consequently, we deduced that the ZPE inclusion is essential to the isomers' energy ordering and molecular properties. The third row of Table 3.1 shows the energy order considering the Gibbs free energy computed at 298.15 K; at this temperature, the isomers' energy ordering changes: the second isomers are the putative global minima, and the first isomers have the fifth lowest energy. Interestingly, this energy ordering occurs at 298.15 K, and it is a function of the temperature, which we discuss later in the relative population section. The fourth row in Table 3.1 shows the electronic energy considering the ZPE. It follows the same trend in energy ordering when considering the Gibbs free energy, and it is

the same putative global minima. The fifth row in Table 3.1 details the electronic energy. It almost follows the CCSD(T) energies trend, except isomer number 8 takes second place, located at 0.52 kcal/mol above the putative global minimum. The sixth, seventh, and eighth rows in Table 3.1 show the point group symmetry, electronic ground state, and the lowest vibrational frequency of each isomer, respectively. When we use the Gibbs free energy to energy order the structures, the second isomers change to first place, becoming the lowest energy structure; the energy ordering changes drastically, whereas the electronic energy follows a similar trend to that of CCSD(T) energy ordering. This shows us that the level of theory and the inclusion of entropy and temperature change the energy ordering and, therefore, the overall molecular properties.

3.4.2 Relative population

Table 3.2: The five points temperature solid-solid.

$T_{ss_i\text{-g}}/T_{ss_i}$	PBE0-D3/def2-TZVP	PBE0/def2-TZVP
1	(377)/[**33**]	(388)/[**34.5**]
2	(424)/[**22.9**]	(444)/[**22.8**]
3	(316.7)/[**14**]	(305.4)/[**14.7**]
4	(349)/[**17.6**]	(343.6)/[**12.2**]
5	(258)/[**5.7**]	(246.7)/[**4.2**]

We show in Figure 4.4 panel (a) the most important and strongly dominating $T_{ss_1\text{-g}}$ point that is located at 377 K temperature scale with a relative population of 33%. For temperatures ranging from 10 to 377 K, the relative population is strongly dominated by the putative global minima isomer distorted oblate spheroid with C_1 symmetry and this relative population is similar to -T^{-3} function with one point of inflection located at 180 K. After decreases monotonically up to 377 K. At the $T_{ss_1\text{-g}}$ point, the distorted oblate spheroid with C_1 symmetry co-exist and compete with the coaxial Triple-Layered structures with C_s symmetry; This implies that the distorted oblate spheroid will be replaced with the coaxial Triple-Layered structures. Above temperature 377 K, the relative population is strongly dominated by the coaxial Triple-Layered structures with C_s symmetry, located at 0.85 kcal/mol above the global minima at temperature 298.15 K. This relative population depicted in blue-solid line in panel (a) has behavior as a sigmoid function, from temperatures ranging from 377 to 600 K, it grows rapidally and from temperatures ranging from 600 to 1500 K, it almost keeps constant with 60%. The second $T_{ss_2\text{-g}}$ point is located at temperature 424 K with a relative population of 22.9%, and this point the global minima distorted oblate spheroid with C_1 symmetry co-exist, and compete with the coaxial Triple-Layered structures with C_{2v} symmetry, located at

1.23 kcal/mol above the global minima at 298.15 K. The relative population of the coaxial Triple-Layered C_{2v} symmetry depicted in green-solid line in panel (a) also has a behavior of a sigmoid function and up to 600 K it keeps constant with 32% of relative population. The $T_{ss_3\text{-g}}$, and $T_{ss_4\text{-g}}$ points, displayed in Figure 4.4 panel (a),

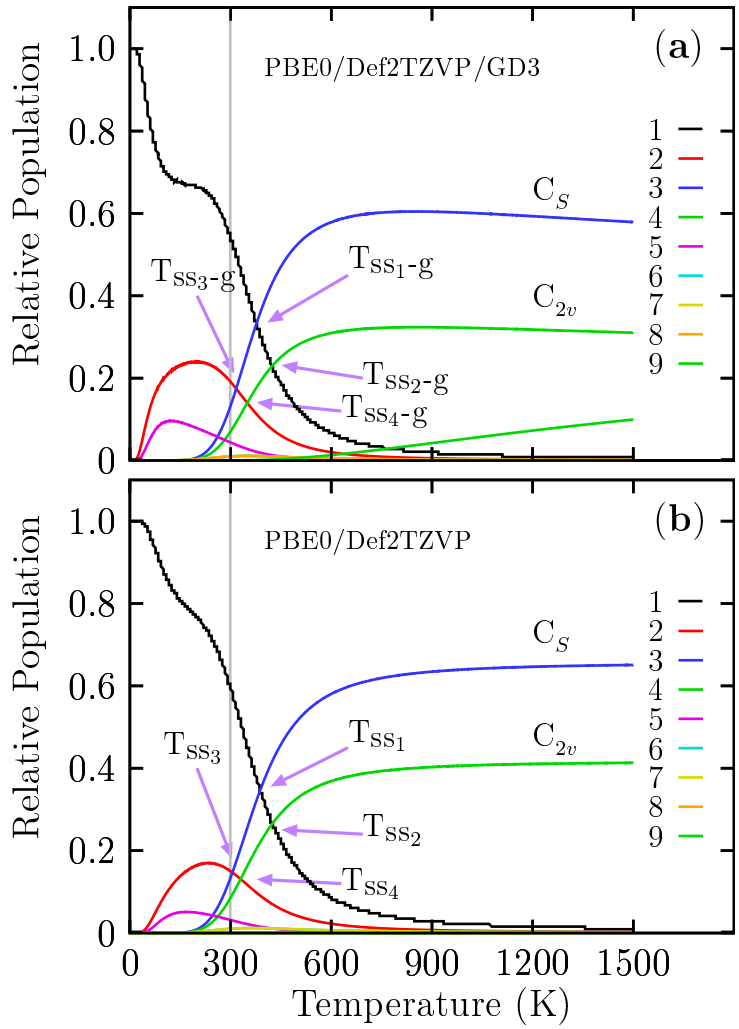

Figure 3.5: The panels shows the relative population for the temperatures ranging from 10 to 1500 K.

are located at 316.7 K, and 349 K axis temperature with relative populations 14% and 17%, respectively. These relative populations correspond to the second isomer located just 0.61 kcal/mol at 298.15 K above the global minima, and co-existing at the temperatures 316.7 K and 349 K with the coaxial Triple-Layered structures with C_s, and C_{2v} symmetries, respectively. At low temperatures range, this isomer's relative population depicted in red-solid line of Figure 4.4a is around only 20%, and up to room temperature, it decreases exponentially to zero. At temperatures up to 600 K, the relative population is zero; hence, at high temperatures these isomers do

not contribute to the molecular properties. The relative population lower than 10%, depicted in violet-solid line shows in Figure 4.4a, correspond to the isomers located at 1.48 kcal/mol above global minima at 298.15 K. Interesting, this structure is the putative minimum global when the CCSD(T) energy is employed in the ordering energetic, despite that, this structure's relative population clearly shows that this structure does not contribute to molecular properties in all ranges of temperatures. The average B-B bond length for this structure is 1.63 Å, distant for the lowest average B-B bond length of 1.53 Å. Moreover, this structure has the largest positive contribution to the relative zero-point energy. This suggests that not just the global minimum and its closest energy isomers of a potential/free energy surface are important, but also the contribution entropic effects and temperature are decisive in which isomers are going to contribute to molecular properties in a temperature ranging of interest. It should be pointed out that neither the helix-type structure reported by Guo *et al.* [3] nor the putative global minimum found in this study, also reported by Yañez *et al.* [50] at a high level of theory, is the putative global minimum when we take into account the entropic term. Our results lead to that the entropic effect should be taken into account. So far, at this point, one may ask if there is a simple and easy method to elucidate which isomers have the largest entopic contributions. This question is going to be boarded in the relative zero-point energy decomposition section. Another interesting question is: What is the effect of Grimme's dispersion (D3) on the relative population?. Figure 4.4, panel (b) shows four transitions solid-solid temperature points T_{ss_1}, T_{ss_2}, T_{ss_3}, and T_{ss_4}, without Grimme's dispersion (D3), and for ease of comparison displayed in round parenthesis in Table. 3.2 togheter with the probability of occurrence in bold and square brackets. The T_{ss_1}, and T_{ss_2} point shifts in the temperature axis to a higeher temperature by 10 K, and 20K, whereas the relative population has a little variations not larger than 1.5%. The T_{ss_3}, T_{ss_4}, and T_{ss_5} shifts to low temperature, at the first galance, it suggest that the effect of the dispersion on the relative population is a little shift of the two dominant T_{ss} points from low temperatures to higher temperatures, almost keeping the relative populations constant. In contrast with the T_{ss} points, with lower probability occurrence, shows a little shift from high temperature to lower temperatures with little changes in the relative population. The total properties in a molecule are statistical averages over the ensemble of isomers. Thus, it is crucial as far as possible to make a complete sampling of the potential energy surface to consider all isomers. The search of the low-energy structures is not straightforward, and many times this could be lead to missing some low-energy isomers. In this respect, One might well ask what happens if we have a missing low-energy structure when we compute the relative populations and their consequence on the computation of any molecular properties. Figure 3.6 shows the computed relative population when the two coaxial Triple-Layered C_S and C_{2v} structures have been taken out of the isomers pool database. Indeed, in the temperature ranging from 773 to 1500 K, the relative population depicted in yellow-solid line in Figure 3.6 indicate that the dominant structure is a distorted coaxial Triple-Layered depicted in Figure 3.3(10) and located at 9.20 kcal/mol above the putative global minimum at

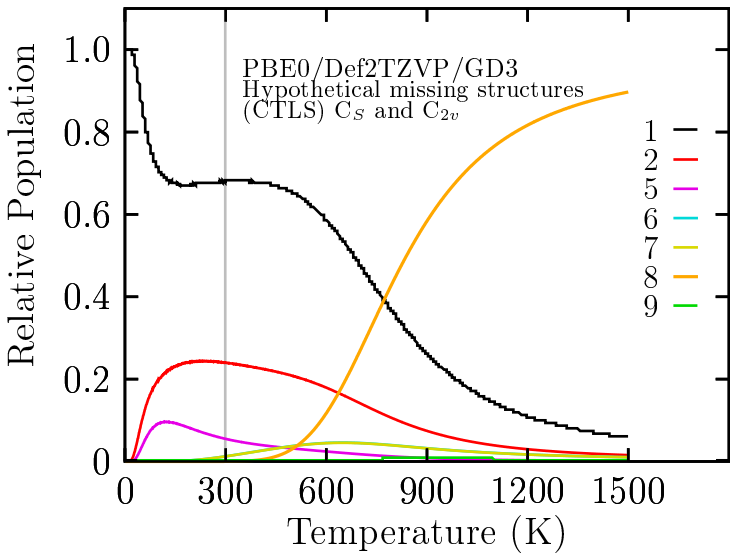

Figure 3.6: The relative population of $Be_6B_{11}^-$ cluster.

CCSD(T) level of theory. Furthermore, analysis of results on the average B-B bond length shows in Figure 3.2 indicates that the structure with the second-lowest bond length is also the same distorted coaxial Triple-Layered structure. This result leads to a couple of interesting observations in the case of $Be_6B_{11}^-$ cluster. Even at the high level of theory, the lowest energy structure (at T=0) does not necessarily have the associated largest entropic effect, and the structure with the lowest B-B bond is correlated with the largest entropic effects. It is worthwhile to note that in the temperature ranging from 377 to 1500 K, in Figure 4.4 panel (a), the relative population depicted blue-solid line indicates that the coaxial Triple-Layered structures with C_s symmetry is energetically more favorable than the coaxial Triple-Layered structures with C_{2v} symmetry. Moreover, those two structures strongly dominate in this range of temperature. These results pointed out that we must consider more than one more isomer with point-group symmetries, ranging from the low-symmetry to high-symmetry. Figure 3.7 panel (a) display the relative population computed without taking into account the C_{2v} symmetry coaxial Triple-Layered structure in the pool database, and panel (b) displays the relative population computed without taking into account the C_{2v}symmetry coaxial Triple-Layered symmetry in the pool database. A Comparison between the relative population shows in panel (a) and panel (b) of Figure 3.7 indicates, on the one hand, that that dominant T_{ss} point does not shift when we do not consider the high-symmetry, and on the other hand, the dominant T_{ss} point shifts from 379 to 425 K when we no take into account the low-symmetry structure. This result leads to the observation that it is more important to calculate the relative population considering the low-symmetry structure than only structures with high symmetries. The reason is when we consider low-symmetry structures; the T_{SS} point does not change. In contrast, when we take

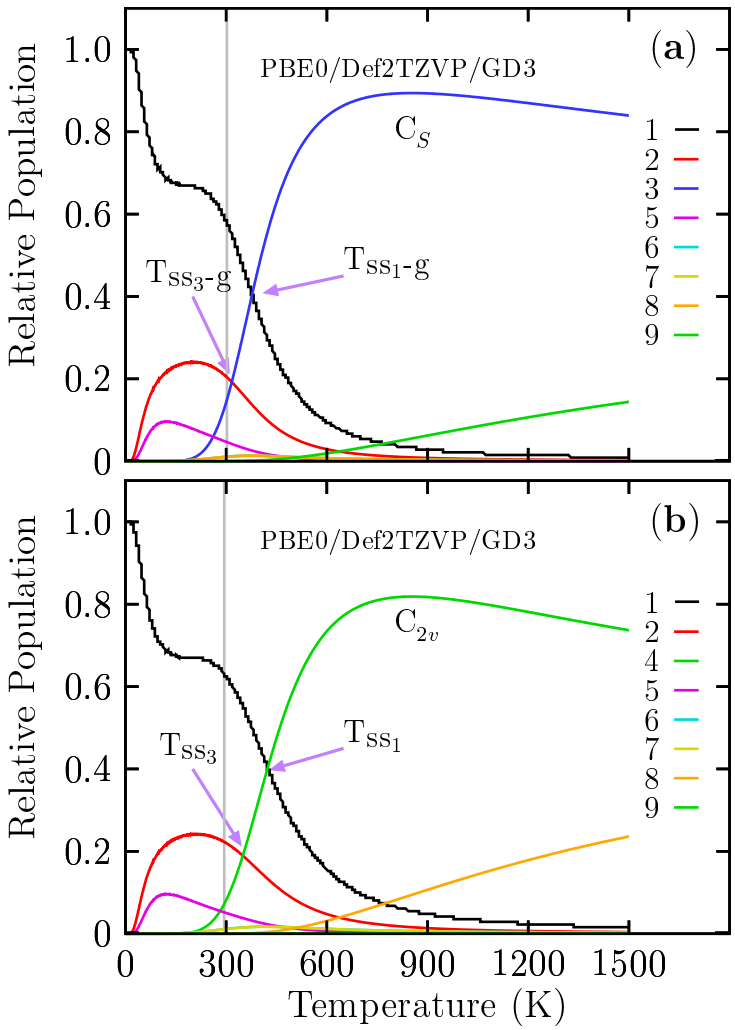

Figure 3.7: The relative population of $Be_6B_{11}^-$ cluster.

only higher -symmetries structures, the T_{SS} shift with important consequences in the molecular properties when we compute the molecular properties as statistical averages over the an ensemble of isomers.

3.4.3 Relative population at CCSD(T) level of theory

Figure 3.8 shows the relative population computed at single point CCSD(T)/def2-TZVP//PBE0-D3/def2-TZVP level of theory. For temperatures ranging from 10 to 357 K, the relative population is strongly dominated by the putative global minima isomer with C_1 symmetry and the relative population decreases monotonically up to 357 K. At the $T_{ss_1\text{-c}}$ point, the distorted C_1 symmetry co-exist and compete with the coaxial Triple-Layered structures with C_s symmetry. The dominant structure at low tmeperatures is the lowest energy structure depicted in Figure 3.3(1) with

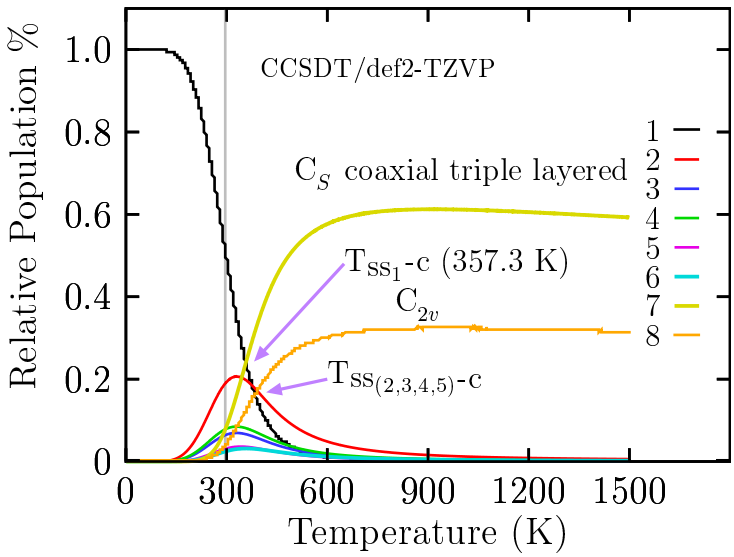

Figure 3.8: The thermal population computed at CCSD(T) level of theory.

C_1 symmetry at SP CCSD(T) level of theory.

3.4.4 Molecular Dynamics

In this study to explore and gain insights into the dynamical behavior of $Be_6B_{11}^-$ a Born-Oppenheimer molecular dynamics (BOMD) was performed employing the deMon2K program [189] (deMon2k v. 6.01, Cinvestav, Mexico City 2011) at three different temperatures, 1600 K, 2000 K, and 2500 K, and the PBE/DZVP level of theory. We have chosen the temperatures from 1600K to 2500 K due to these temperatures are close to the melting points of boron (2349 K) and beryllium (1560 K). The BOMD's were started from the initial configuration of the coaxial-triple layered structure (the putative global minimum at a temperature of 1500 K), employing a Hoover thermal bath with random initial velocities imposed to the atoms, and for a simulation time of 25 ps with a step size of 1 fs. As the temperature increases, $Be_6B_{11}^-$ cluster is subject to dissociation phenomena. Based on the BOMD simulation results, we found the dissociation processes of the $Be_6B_{11}^-$ cluster occurs at a temperature of 2000 K, whereas there is no dissociation during the BOMD simulation at 1600 K; the cluster maintains its connectivity at this temperature. At a temperature of 2500 K, the dissociation processes are stronger, and more beryllium atoms are escaped. Min Li noted that nanoparticles of tungsten dissociate when the temperature of tungsten nanoparticles is higher than the melting temperature. Our results make sense if we considered that the BOMD of $Be_6B_{11}^-$ cluster there is not dissociation at 1600 K, whereas at the temperature of 2000 K, there are dissociation phenomena. From the mentioned previously, we can infer that the melting point of the $Be_6B_{11}^-$ cluster is in the temperature ranging from 1600 K to 2000 K.

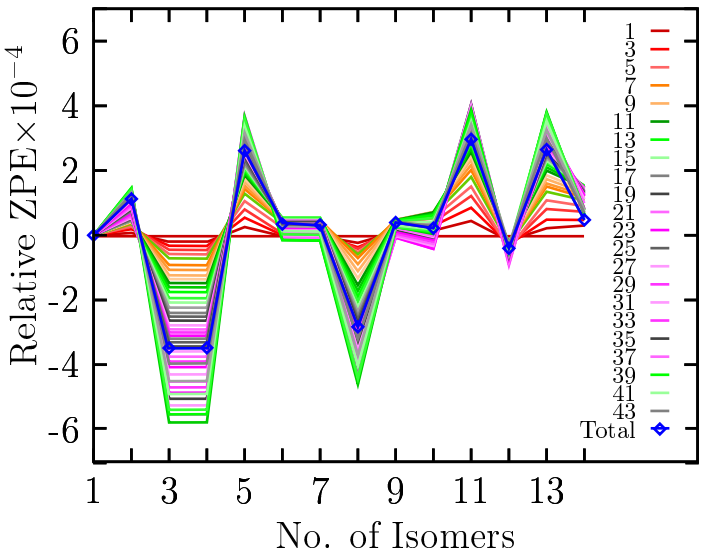

Figure 3.9: Relative $\mathcal{E}_{\text{ZPE}}$ decomposition.

3.4.5 Contributions of the vibrational modes to the ZPE energy.

At temperature zero, the lowest energy structure has the electronic energy plus zero-point energy computed as the sum of all vibration modes. If one increases the system's temperature, entropic effects start to play an important role, and Gibbs's free energy determines the lowest energy structure. The significant contribution to entropy comes from low vibrational modes, and it is approximately proportional to the logarithmic sum of low frequencies, [190] in the other hand, high vibrational modes yield small contributions to vibrational entropy. The Equation 3.2 gives the zero-point energy ($\mathcal{E}_{\text{ZPE}}$), where ν_i are all 3N-6 vibrational modes that the cluster possesses. Figure 3.9 shows the relative $\mathcal{E}_{\text{ZPE}}$ as a function of vibrational modes and isomers that are arranged in energy, from the lowest (1) to the highest energy isomer (14). Remarkably, the smallest value of the total relative $\mathcal{E}_{\text{ZPE}}$ (the minimum of $\mathcal{E}_{\text{ZPE}}$) correlates with the lowest energy structure at high temperatures. The relative population displayed in Figure 4.4 panel (a) shows that the isomer three and four, that correspond to coaxial triple-layered structure with C_s and C_{2v} symmetries respectively, strongly dominate in the temperature range up to 377 K.

$$ZPE = \frac{1}{2}\sum_{i=1}^{3N-6} \nu_i \tag{3.2}$$

Figure 3.9 shows the relative $\mathcal{E}_{\text{ZPE}}$ as a function of vibrational modes and isomers that are energetically ordered, from the lowest (1) to the highest energy isomer (14). Remarkably, the smallest value of the total relative ZPE (the minimum of $\mathcal{E}_{\text{ZPE}}$) correlates with the lowest energy structure at high temperatures. The relative population displayed in Figure 4.4 panel (a) shows that the isomer three and four,

that correspond to coaxial triple-layered structure with C_s and C_{2v} symmetries respectively, strongly dominate in the temperature range up to 377 K. In Figure 3.9, one can see that isomers three and four, the coaxial Triple-Layered structures with C_s and C_{2v} symmetries possess the lowest value of the relative ZPE. Interestingly, the structures with the lowest relative $\mathcal{E}_{\mathrm{ZPE}}$ are correlated with the structures that strongly dominate the putative global minima at high temperatures. This suggests that those structures possess the highest entropic effects. To understand which lowest vibrational modes contribute to the lowest ZPE, we decompose the relative $\mathcal{E}_{\mathrm{ZPE}}$ as a function of the number of modes, adding the number of modes needed to build the smallest value of $\mathcal{E}_{\mathrm{ZPE}}$. The blue-solid line in Figure 3.9 depicts the total relative ZPE employing the forty five vibrational modes, the red-solid lines depicts the relative ZPE with emplying modes from first to the sixth and so on. The Be_6 B_{11}^- cluster posse forty five vibrational modes, we found that we have to add the lowest thirty eight vibrational modes to make the smallest value of relative ZPE. The frequency of mode thirty eight is 1026 cm^{-1}, which indicates that is the highest frequency (cutoff frequency) that contributes to making minimum relative ZPE and, therefore, those vibrational frequencies that are in the range of 46 to 1026 cm $^{-1}$ makes the significant contribution to entropy. The vibrational modes number 39 to 45 (1036-1518 cm^{-1}) does not make contributions to lowering the relative ZPE, as shown in Figure 3.9

3.4.6 Infrared spectroscopy

In this chapter, each isomer's IR spectra and how the relative stabilities contribute to the total IR spectra are discussed. In this study, each isomer's IR spectra were computed using DFT as it is implemented in *Gaussian 09* code; under the harmonic approximation, anharmonic effects are not considered. The effect of temperature on the total spectra and the total IR spectra were computed as a Boltzmann weighted sum of each isomer's IR spectra, implemented in BOFA. As the Boltzmann factors depend on temperature, the total resulting IR spectra depend on temperature. In a previous work, [46] one of the authors computed the total dipole moment as a dipole moment weighted by the Boltzmann factors and successfully compared it with experimental data. From the experimental point of view, Sieber *et al.* [175] compared the measured absorption spectrum of the Ag_9 cluster to a sum of different absorption spectra of the Ag_9 cluster computed by DFT. Concerning boron clusters, the vibrational spectrum of boron cluster B_{13}^+ was measured by infrared photodissociation spectroscopy and also compared with computed spectra. Experimental spectroscopy studies employing anion photoelectron spectroscopy on boron anions cluster up to B_{40}^- clusters have been done. Additionally, the structure of neutral boron clusters B_{11}, B_{16}, and B_{17} was also probed by IR. The IR spectrum is related to vibrations that alter the dipole moment. These spectra are usually used to identify functional groups and chemical bond information, and are useful in organic/inorganic chemistry. However, from an experimental perspective, the assignment of IR bands to vibrational molecular modes can be somewhat difficult and

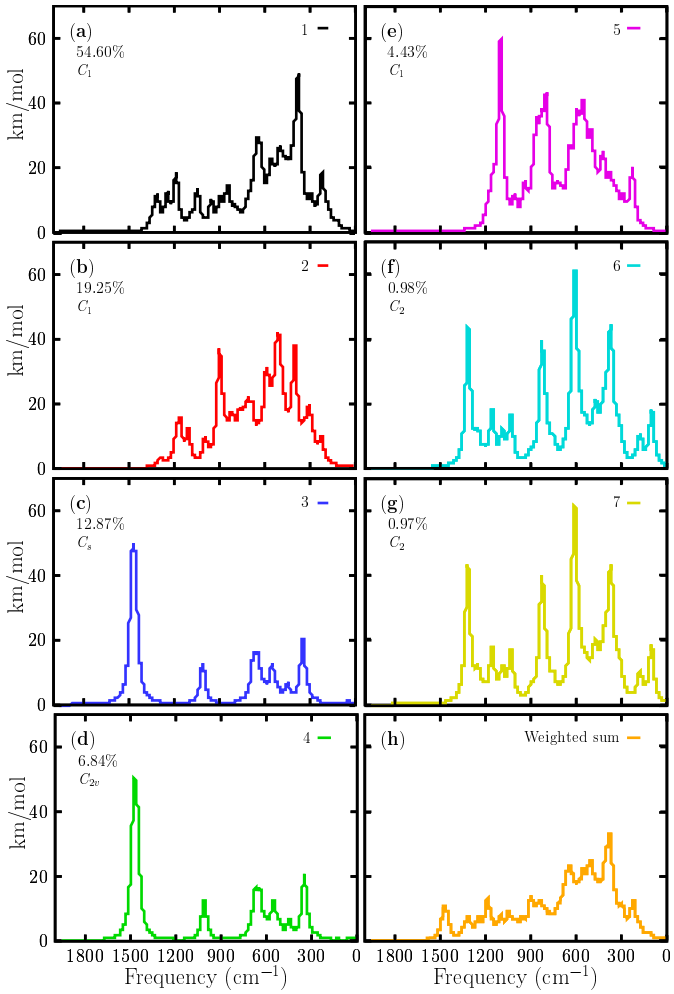

Figure 3.10: Panels (a) to (g) shows computed infrared spectra of boron clusters.

requires *ab-initio* calculations. In these computations, the temperature is generally not considered, and discrepancies between experimental and calculated IR spectra can result from finite temperature and anharmonic effects. It is also important to remember that the experiments are essential of multi-photon nature, whereas calculations IR spectra assume single-photon processes. Figure 3.10(a-g) display the individual IR spectra that belong to the putative global minima and the six lowest energy structures, respectively, located in the relative energy range up 0 to 2.38 kcal/mol at 298.15 K. Figure 3.10h shows the Boltzmann weighted spectrum at 298.15 K computed with BOFA. Interestingly, 93% of the total weighted IR spectra was found to be composed of the individuals spectral contributions of the four lowest energy structures located at an energy scale-up of 0 to 1.23 kcal/mol. The other 7% of the Boltzmann weighted spectra is composed of the IR spectra of the three structures located in the energy range from 1.48 to 2.38 kcal/mol. In the total

weighted Boltzmann IR spectrum in Figure 7h, there are three segments on its frequency axis. The first segment is located in the frequency range of 0 to 700 cm^{-1}. The main bands observed in this range correspond to the IR vibrational modes of the global minimum. The highest peak is located in the 387 cm^{-1} frequency axis, which corresponds to compression of the main ring formed by 10 boron atoms. It is located mainly on one side of the ring, accompanied by the vibrations of the two beryllium atoms. The second band is located at 669 cm^{-1} in the frequency axis. This corresponds mainly to the 10-ring boron's small asymmetric vibration and a minor vibration of the six beryllium atoms. The third peak is located at 225 cm^{-1} on the frequency axis. It corresponds mainly to a stretching of the boron atom that does not form part of the boron ring, together with the two beryllium atoms located close to the boron. The second segment is located in the frequency range of 700 to 1400 cm^{-1}. In the Boltzmann weighted IR displayed in Figure 3.10h, the band observed at 900 cm^{-1} is mainly composed of the 19.2% contribution of the individual IR spectrum of the second isomer that lay 0.61 kcal/mol above the global minimum; this vibrational mode of the second isomer corresponds to the stretching of the three beryllium atoms located on one side along with a boron atom, together with the stretching of one of the boron atoms. The band observed at 1200 cm^{-1} (Figure 3.10h) is mainly associated with the global minima's IR spectrum, which corresponds to the boron atoms unique stretching. There is almost no vibration of the beryllium atoms. The band observed at 1500 cm^{-1} (Figure 3.10h) is completely composed of the contribution of 12% of the individual IR spectra of the third isomer, which has a coaxial triple-layered structure with C_s symmetry located 0.85 kcal/mol above the putative global minima. The fourth isomer's contribution is the coaxial triple-layered structure with C_{2v} symmetry located 1.23 kcal/mol above the global minimum. The different symmetries of the coaxial triple-layered structures (C_{2v} and C_s) are responsible for the different contributions to the total weighted IR spectrum. The low-symmetry isomers become more stable at high temperatures as a result of entropic effects. Interestingly, neither individual IR spectrum of the putative global minimum nor the individual IR spectrum of the second isomer, which was 0.61 kcal/mol above the putative global minimum, has any IR band in the range of 1500 cm^{-1}. Based on this, we assigned this band at 1500 cm^{-1} in the total Boltzmann weighted IR spectrum to the third and four isomers, which have a coaxial triple-layered structure with two different symmetries. The helix-type structures proposed by Guo *et al.* [3] have a small contribution to the IR spectra in all ranges of temperature. The methodology employed in this paper for the assignment of the IR bands demonstrates that the total IR spectra are a mixture of many contributions from the low-energy structures. In this cluster, the total IR spectrum's low-energy region is attributed to the putative minimum global contribution. In contrast, the high-energy region of the total IR spectrum is attributed to the isomers contribution on the high-energy axis. Figure 3.11 displays the IR spectra computed as a function of temperature. Figure 3.11a shows the total Boltzmann weighted IR spectra in the temperature range of 10 to 300 K. Note that the IR spectrum at low temperatures is strongly dominated by the individual IR spectrum of the putative

global minimum; this finding is in agreement with the relative population displayed in Figure 4.4. Below 377 K, the relative population is strongly dominated by the putative global minimum. The band observed at 1500 cm^{-1} in Figure 3.11a starts

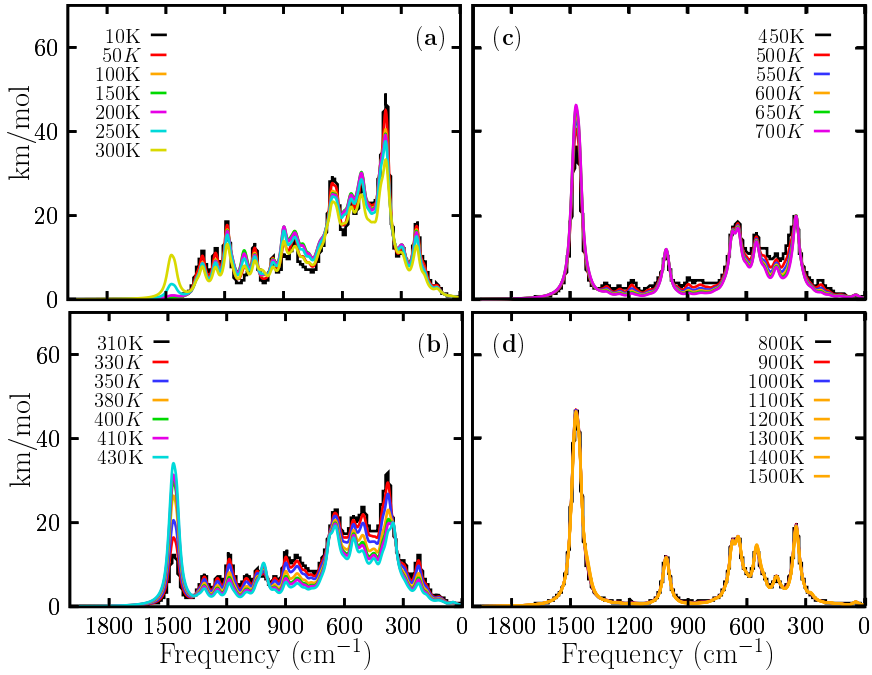

Figure 3.11: Panels (a) to (g) show the computed infrared spectra of boron clusters.

to increase at 200 K (pink line), increases again at 250 K (cyan line), and increases further at 300 K (yellow line). This IR band has contributions from the individual IR spectra of the coaxial triple-layered structures with Cs and C_{2v} symmetries. It is in complete agreement with the relative population displayed in Figure 4.4a. The relative population of the coaxial triple-layered structures start to increase at 200 K. Figure 3.11b shows the IR spectra in the range of 310 to 410 K. Within this temperature range, most transformation solid-solid point occur with different probabilities of occurrences as shown in Figure 4.4a; therefore, large changes in the total weighted IR spectra are also expected. In Figure 3.11b, the IR band located at 1500 cm^{-1} continues increasing at 310 K, and it persists, increasing to 430 K (cyan line). This vibrational mode pertains to an individual IR spectrum of the isomer with coaxial triple-layered structures displayed in Figure 3.10c. This is completely in agreement with the relative population displayed in Figure 4.4. From 377 to 1500 K, the relative population is strongly dominated by the coaxial contributions of the triple-layered structures with C_s and C_{2v} symmetries. The appearance and constant growth of the peak located at 1500 cm^{-1} in the weighted total IR spectrum displayed in Figure 3.11b, as a function of temperature, indicate the coexistence and competition of at least two strongly dominant structures at a specific finite

temperature (377 K). Most importantly, the constant growth of the peak located at 1500 cm^{-1} is indicative that putative global minimum interchange occurs as a function of temperature. This suggests that we must search exhaustively and systematically for the putative global minimum on the potential/free energy surface and its full distribution of all low-energy structures if we want to assign IR bands to specific vibrational modes. This paper shows how some IR bands in the Boltzmann weighted total IR spectrum belong to the IR spectra of isomers located on the higher energy axis. In summary, in the Boltzmann weighted total IR spectrum shown in Figure 3.11b, the low-frequency range is dominated by the contributions of the putative global minimum, whereas the high-frequency range is dominated by geometric structures located at higher energies. Figure 3.11b shows the IR spectra in the range of 310 to 410 K. Within this temperature range, most solid-solid transitions occur with different probabilities, as shown in Figure 4.4a; therefore, large changes in the total weighted IR spectra are also expected. In Figure 3.11b, the IR band located at 1500 cm^{-1} continues increasing at 310 K, and it persists, increasing up to 430 K (cyan line). This vibrational mode pertains to an individual IR spectrum of the coaxial triple-layered isomer displayed in Figure 3.10c. This is completely in agreement with the relative population displayed in Figure 4.4a. The peak located at 1500 cm^{-1}, shows in Figure 3.11, panels (a-d), is present only in temperatures higher than 300 K, where the coaxial-triple layer structures start to be the lowest energy structures. The abovementioned reasons indicate that the vibrational modes located in the range of 1036 to 1518 cm^{-1} are responsible for the cluster's fluxionality. The B-B stretching modes of the B_{11} ring are located in the range of 1036 to 1518 cm^{-1}. This is correlated to hyperconjugation, delocalization, and fluxionality of the cluster.

3.5 Conclusions

In summary, we systematically explored the potential and free energy surface of the $Be_6B_{11}^-$ cluster using an unbiased hybrid, efficient, and multistep/multilevel algorithm implemented in Python and coupled to density functional theory. The temperature effects were considered employing Gibb's free energy. If the system's temperature is increased, entropic effects start to play an important role, and Gibbs's free energy determines the lowest energy structure.

Chapter 4

The Be_4B_8 cluster

4.1 Abstract

The lowest-energy structure, distribution of isomers, and their molecular properties depend significantly on the geometry and temperature. The total energy computations under DFT methodology are typically carried out at zero temperature; thereby, entropic contributions to total energy are neglected, even though functional materials work at finite temperature.

In this chapter, the probability of occurrence of one particular Be_4B_8 isomer at temperature T is estimated within the framework of quantum statistical mechanics and nanothermodynamics. To locate a list of all possible low-energy chiral and achiral structures, an exhaustive and efficient exploration of the potential/free energy surface is done by employing a multilevel multistep global genetic algorithm search coupled to DFT. Moreover, we discuss the energetic ordering of structures computed at the DFT level against single-point energy calculations at the CCSD(T) level of theory. The computed VCD/IR spectrum of each isomer is multiplied by their corresponding Boltzmann weight at temperature T; then, they are summed together to produce a final Boltzmann weighted spectrum. Additionally, we present chemical bonding analysis using the Adaptive Natural Density Partitioning method in the chiral putative global minimum. The transition state structures and the enantiomer-enantiomer and enantiomer-achiral activation energies as a function of temperature, evidence that a change from an endergonic to an exergonic type of reaction occurs at a temperature of 739 K.

4.2 Introduction

The potential of boron atom to form stable molecular networks [191, 131] lies in the fact that it has three valence electrons and four available orbitals, which implies it is electron deficient. Moreover, it has a small covalent radius of 0.8-1.01 Å [192, 193], high ionization energy 344.2 kJ/mol [192], and an affinity for oxygen atoms, which is the basis of borates [194, 192]. Boron electron deficiency gives origin to vast number of allotropic forms and uncommon geometries [102, 110, 131] such as nanotubes, [117, 28] borospherenes [119], borophene [110], cages [28, 120], planar [115], quasi planar [86], rings [177, 138], chiral [116, 195], boron-based helix clusters [3, 121],and fluxional boron clusters [3, 144] that have recently attracted the interest of experimental and theoretical researchers. Since the molecular properties depend greatly on their geometry and temperature [16, 1]; boron cluster ex-

hibit a large number of molecular properties that yield potential applications in medicine [109, 125, 196, 197], molecular motors [147, 3], superhard materials [198], hydrogen storage [199], batteries [200, 201, 202, 203], catalysis [204], and energy materials [205] among many others.

Particularly, the chirality of nanoclusters has attracted attention due to their chiroptical properties, potential application in efficient chiral discrimination [82, 83], nonlinear optics [84] and chiral materials with interesting properties, [85, 86, 87] and of course, not to mention that chiral structures play a decisive role in biological activity. [88]

Previous theoretical studies joint with experimental photoelectron spectroscopy reported the first pure boron chiral B_{30}^- structure as the putative global minimum. [86] In these pair of planar enantiomers, the chirality arises due to the hexagonal hole and its position. A year later, the lowest energy structures of the B_{39}^- borospherene were reported as chiral due to their hexagonal and pentagonal holes. [118] Similarly, the B_{44} cluster was reported as a chiral structure due to its nonagonal holes. [195] That is, in these clusters, holes in the structure cause chirality. Regarding beryllium-doped boron clusters, they exhibit remarkable properties suach as fluxionality, [3, 206, 207, 110, 208, 209] aromaticity, [3, 210] and characteristics similar to borophene. [107] Furthermore, previous theoretical studies showed that the boron fullerenes B_{60} and B_{80} can be stabilized by surrounding the boron clusters with beryllium atoms, [211, 212] which effectively compensates for boron electronic deficiency. [212] These effects make beryllium-doped boron clusters interesting.

Particularly attractive are the chiral helices $Be_6B_{11}^-$, reported by Gou *et al.* [3], Yanez *et al.*, [50] and Garcia-Buelna *et al.* [1] as one of the low-lying and fluxional isomers, and later a chemical bonding and mechanism of formation study of the beryllium-doped boron chiral cluster $Be_6B_{10}^{2-}$ and coaxial triple-layered $Be_6B_{11}^-$ sandwich structure were reported. [121, 209] In these structures, the chirality arises due to the formation of a boron helix.

However, there are only a few theoretical studies on vibrational circular dichroism (VCD) and infrared spectroscopy (IR) as a function of temperature in beryllium-boron clusters [213, 1]. We emphasize that there are neither theoretical nor experimental studies of VCD / IR spectra in chiral Be_4B_8 clusters, although VCD/IR spectra give insight into the geometrical structure. [214, 215, 216, 217] Reciently, Castiglioni *et al.* reviewed experimental aspects of solid-state circular dichroism, [218] and Avilés Moreno *et al.* reported the experimental and theoretical IR/VCD spectra of various compounds. [219, 220, 221, 222] VCD is differential spectroscopy sensitive to the difference in the absorption for the left and right polarized light. [214, 223, 217] It usually is four times in magnitude smaller than IR absorption [224] and yields information on the lowest energy conformation in solution; [225] thus, the chiral molecule's absolute configuration can be determined employing the VCD spectra. [226]

The IR frequencies are related to the second derivative of the potential energy and they are useful in identifying transition states and computing thermodynamics through the vibrational partition function. [1, 58, 178] Additionally, the structure

of neutral boron clusters B_{11}, B_{16} and B_{17} was probed by IR. [146]. The DFT VCD/IR spectra depend on the functional and basis set employed [216] and significantly on the lowest- and the low-energy achiral and chiral structures, so we need an efficiently sampling of the free energy surface to know the distribution of isomers at different temperatures. [2, 1, 16, 65, 64, 63] A considerable change in the isomer distribution and the energetic separation among them is the first notable effect of temperature. [1, 2] Useful materials work at finite temperatures; in that conditions, Gibbs free energy is minimized [56] and determines the putative global minimum at given temperature, [1] whereas, entropy of the atomic cluster is maximized. [56] Although in the mid 1960's, Mermin *et al.* [227] studied the thermal properties of the inhomogeneous electron gas, most of DFT calculations are typically performed at zero temperature. Recently, over again, DFT was extended to finite temperature, [228, 229, 230] but nowadays, as far as we know, it is not implemented in any software. However, molecular dynamics and other simulation tools have been employed to study atomic clusters at finite temperatures. [106, 155, 231, 101, 52, 165] In this study, based on the Gibbs free energy of each isomer and Boltzmann factors, we computed the probability of occurrence (Boltzmann weights) of each particular isomer of Be_4B_8 as a function of temperature using quantum statistical mechanics. The computed VCD/IR spectrum of each isomer is multiplied by their corresponding Boltzmann weight at temperature T; then, they are summed together to produce a final Boltzmann weighted spectrum. In the mid 1980, P. J. Stephens with coworkers implemented the atomic axial tensors in Gaussian 80 code that allows them to compute the VCD spectrum of propylene oxide and compare with the experimental spectrum [232] Later, Nafie and Stephens employed the Boltzmann weights scheme, they computed the VCD spectrum for each isomer, and the total resulting spectra were averaged and weighted by Boltzmann factors. [233, 214, 234, 235] Recently these factors were used in other previous works. [65, 1, 64, 228, 63].

To achieve the mentioned above, we located all low-energy structures on the potential and free energy surfaces of the Be_4B_8 cluster with a genetic algorithm coupled to DFT and computed the Boltzmann weights in temperatures ranging from 20 to 1900 K. We also located the solid-solid transformation point at 739 K, where chiral and achiral structures coexist, and computed the energy barrier (E_a) for temperatures ranging from 20 to 1900 K for transformation of enantiomers (plus, $\mathcal{P}$) to an achiral structure. We locate the T_{ee} point is defined here as the temperature where the reaction change from endergonic to exergonic. Moreover, the energy of enantiomerization was computed between $\mathcal{P}$ and minus ($\mathcal{M}$) enantiomers, and we defined the T_{bb} point in scale temperature where the energy barrier of two possible reaction mechanisms is equal to each other, which implies the velocity of the reaction is equal for both mechanisms. We investigated how the symmetry point group affects the Gibbs free energy. Our results show that the chirality on Be_4B_8 arises from the Be-Be dimers capping the boron ring and also of the distorted boron ring, thus, the lowest energy chiral structure is favored by the interaction between beryllium and the boron framework. The high energy of enantiomerization of the Be_4B_8 cluster in temperatures ranging from 20 to 1900 K suggests that it is a good candidate for

applications; only one of the enantiomers shows the desired effect. The computed enthalpy of formation (ΔH) between chiral and achiral structure at 739 K show that there is a change from endo to exothermic reaction. Our results indicate that the Boltzmann weighted VCD spectrum is zero in all range of temperature, wheras, the Boltzmann IR weighted spectrum is strongly dominated by the lowest energy pair of enantiomers. The remainder of the chapter is organized as follows: the computational details and a brief overview of the theory and the algorithms used. The results and discussion are presented next. We discuss the effect of the symmetry in the energetic ordering and clarify the origin of the 0.41 kcal/mol difference energy between two structures with symmetries C_2 and C_1 that appear when we compute the Gibbs free energy. A comparison among energies computed at a single point CCSDT against DFT levels of theory and the $\mathcal{T}_1$ diagnostic is presented. We do the chemical bonding analysis by employing the AdNDP scheme to $\mathcal{P}$ minimum energy structure. The interconversion energy barrier between the $\mathcal{P}$ and $\mathcal{M}$ enantiomers and between an achiral structure and $\mathcal{P}$ enantiomer are discussed in terms of temperature. IR spectra are analyzed as a function of temperaturea, and conclusions are given.

4.3 Results and discussion

4.3.1 The lowest energy structures and energetics

Figure 4.1 shows the low-energy configurations of Be_4B_8 clusters optimized at PBE0-GD3/def2-TZVP level of theory taking into account ZPE energy correction. The optimized average B-B bond length of the putative chiral global minimum is 1.5867 Å, in good agreement with an experimental bond length of 1.57-1.59 Å. [185, 186] and also within agreement with others previous DFT calculations. [1] The most recurring motif within the lower energy isomers of B_8Be_4 is a sandwich structure,(SSh) in which the boron atoms form a hollow distorted ellipsoid ring with each of the Be-Be dimers capping the top and bottom with C_1 point group symmetry. Isomers a and b and also listed as i_1 and i_2 in Table 4.1, are enantiomers differing in the orientation of the Be-Be dimers with respect the boron skeleton. Based on the B-B bond length evolution along the intrinsic reaction coordinate (IRC) between Plus-enantiomer-Minus-enantiomers, and displayed in Figure B.2 appendix B.2 the shortest B-B bond length is located at the transition state structure. In contrast, the largest B-B bond length is located in the reactant and product points. On the other hand, appendix Figure B.2 appendix B.2 shows the distance evolution between (Be-Be)-(Be-Be) dimers; one can see the largest distance between dimers is located at the transition state, whereas the shortest distance is located at the product and reactants points. From the above mentioned, the B-B interaction does not favor the formation of the lowest energy enantiomers structures; meanwhile, the Be-Be interaction promotes the lowest energy structure to be chiral. Here, we infer that the Be-B interaction also favors the chiral lowest energy structures. The Be-Be bond length for the six lowest energy enantiomers is

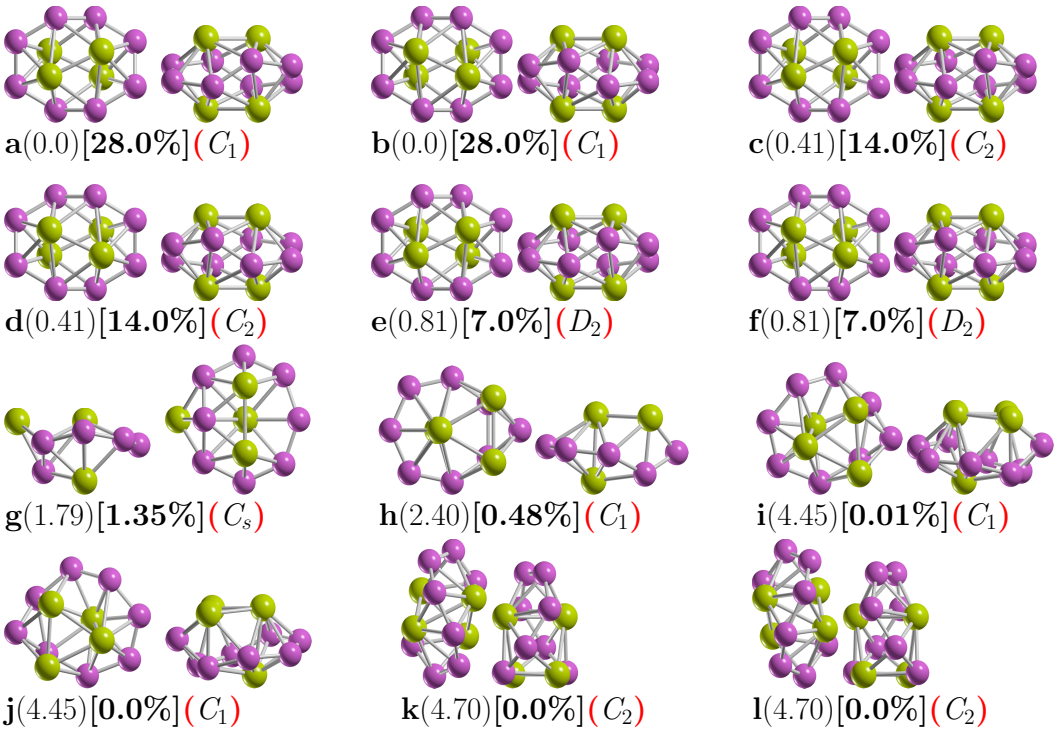

Figure 4.1: Optimized geometries of neutral Be_4B_8 cluster.

1.9874, 1.9876, and 1.9881 Å for symmetries C_1, C_2, and D_2, respectively, in good agreement with the bond length of the Be-Be in Be_2B_8 cluster 1.910 Å. [207] To gain more insight into the chemical bonding, an AdNDP analysis of the lowest energy isomer was performed (Figure 4.2). The AdNDP analysis for this chiral structure revealed the presence of eight 2c-2e B-B σ-bonds with an occupation number (ON) between 1.92 and 1.94 |e| and three delocalized σ-bonds throughout the B_8 ring with an ON between 1.95 and 1.99 |e|. Additionally, three distorted π-bonds (due to the non-planarity of the structure), one of which is delocalized over all eight boron atoms and the other two involving four boron and two beryllium atoms (one from the top and one from the bottom). Finally, the bonding pattern is completed by two 6c-2e σ-bonds with main contribution coming from the interaction between the two Be atoms from the top and bottom, respectively. The isomers with symmetry C_1 are the most energetically favorable, with 28% each of the Boltzmann population at 298.15 K. An exhaustive and systematic exploration of the potential energy surface considering triplet states revealed that the lowest triplet ground state lays 13.7 kcal/mol above the singlet putative chiral global minimum single ground state, which is too far away energetically to be considered. Next, low-energy SSh-isomers labeled i_3 and i_4 in Table 4.1, and depicted in Figure 4.1(3,4) lies just 0.41 kcal/mol above the putative global minimum, it is a similar-SSh structure than the putative global minimum, only with C_2 point group symmetry, followed by slightly

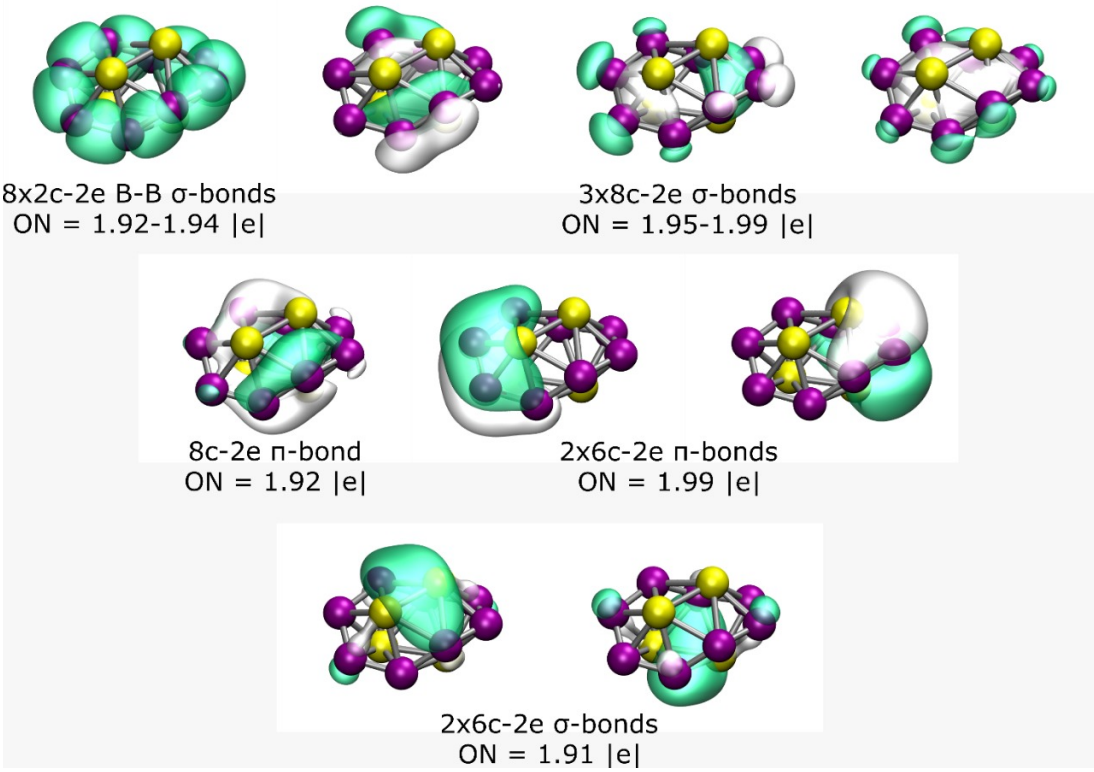

Figure 4.2: Results of the AdNDP analysis of the lowest-energy chiral isomer of the Be_4B_8 system.

higher energy and similar-SSh structure located just 0.81 kcal/mol above the putative minimal structure with D_2 point group symmetry. We point out that the unique differences among these chiral structures are the different symmetry point groups. The most energetically favorable is the non symmetry (C_1) cluster; moreover, these six structures contribute to 98% to the relative population at 298.15 K. The next higher energy structure, labeled as i_7 in Table 4.1 and depicted in Figure 4.1(g), is located at 1.79 kcal/mol above the putative minimum global at 298.15 K, with symmetry C_s. It is also a sandwich structure formed by a distorted circular ring in which one of the Be-Be dimers is capping in the center of the ring, and the other one is located on one face of the boron circular ring. This structure is achiral, and its probability of occurrence is 1.35% at 298.15 K. Next achiral isomer lies 2.40 kcal/mol above the putative minimum global with C_1 symmetry, labeled as i_8 in Table 4.1 and depicted in Figure 4.1(8). It is also a sandwich-type structure formed by a distorted circular boron ring with three boron atoms capping one side of the ring and the other Be atom capping the other. The probability of occurrence of this isomer at 298.15 K is just 0.48% and its contribution to chiroptical spectroscopies is negligible. The next two chiral structures lies 4.45 kcal/mol above the putative global minimum with C_1 symmetries, labeled as i_9 and i_{10} in Table 4.1 and de-

Table 4.1: Single point relative energy calculations of the low energy structures at differents levels of theory.

	Isomers									
Level	i_1	i_2	i_3	i_4	i_5	i_6	i_7	i_8	i_9	i_{10}
ΔG	0.0	0.0	0.41	0.41	0.81	0.81	1.79	2.40	4.45	4.45
CCSDT	0.0	0.0	0.0	0.0	0.0	0.0	3.61	3.38	5.38	5.38
CCSDT+$\mathcal{E}_{\text{ZPE}}$	0.0	0.0	0.0	0.0	0.0	0.0	2.71	2.51	4.51	4.51
DLPNO-CCSD(T)	0.0	0.0	0.0	0.0	0.0	0.0	0.75	1.37	5.0	5.0
DLPNO-CCSD(T)+$\mathcal{E}_{\text{ZPE}}$	0.0	0.0	0.0	0.0	0.0	0.0	-0.20	0.50	4.10	4.10
$\mathcal{E}_0 + \mathcal{E}_{\text{ZPE}}$	0.0	0.0	0.0	0.0	0.0	0.0	2.38	2.80	5.03	5.03
$\mathcal{E}_0$	0.0	0.0	0.0	0.0	0.0	0.0	3.28	3.68	5.90	3.28
Point group symmetry	C_1	C_1	C_2	C_2	D_2	D_2	C_s	C_1	C_1	C_1
$\mathcal{T}_1$ Diagnostic	0.019	0.019	0.019	0.019	0.019	0.019	0.016	0.015	0.016	0.016

picted in Figure 4.1(i,j). They are sandwich-type structures formed by a non-planar distorted circular boron ring with three Be atoms capping one side of the boron ring and the other Be atom is located on the other face, and in the center of the distorted boron ring; Its Boltzmann probability of occurrence is zero at 298.15 K, so as a consequence, at this temperature, its contributions to any chiroptical spectroscopies are negligible. The following chiral higher energy structure, with C_2 point group symmetry, lies 4.70 kcal/mol energy above the putative global minimum. It is a chiral helix type structure depicted in Figure 4.1(12,13); it has four Be atoms located in the center of the boron spiral, this helix structure is similar to those found by previous theoretical works [3, 50, 1] and its probability of occurrence is negligible at room temperature. To gain insight into the energy hierarchy of isomers and validate our DFT calculations, relative energies were computed at different levels of theory, and differences between them are shown in Table 4.1. Energy computed at different methods yield different energies due mainly to the functional and basis-set employed, [236, 2], so the energetic ordering change; consequently, the probability of occurrence and the molecular properties will change. The first line of Table 4.1 shows the relative Gibbs free energy computed at PBE0-GD3/def2-TZVP and room temperature. The small relative Gibbs free energies (0.41, and 0.81 kcal/mol) differences among the six enantiomer structures i_1 to i_6 in Table 4.1 are caused by the rotational entropy being a function of the symmetry number that in turn depends on the point group symmetry. An increase/decrease in the value of rotational entropy changes the Gibbs free energy. The Gibbs free energy computed with and without symmetry will differ by a factor RTln(σ). Here, R is the universal gas constant, T, the temperature, and σ is the symmetry number. Figure 5.3 shows the factor RTln(σ) for temperatures ranging from 0 to 1900 K and for different symmetry number values (σ=2,3,4,5). A closer analysis of Figure 5.3, shows that at room temperature RTln(σ)=0.41 kcal/mol with σ=2, and RTln(σ)=0.81 kcal/mol with σ=4, in agreement with the values shown in the first line of Table 4.1. As the temperature increases, the energy differences between the factors RTln(σ) be-

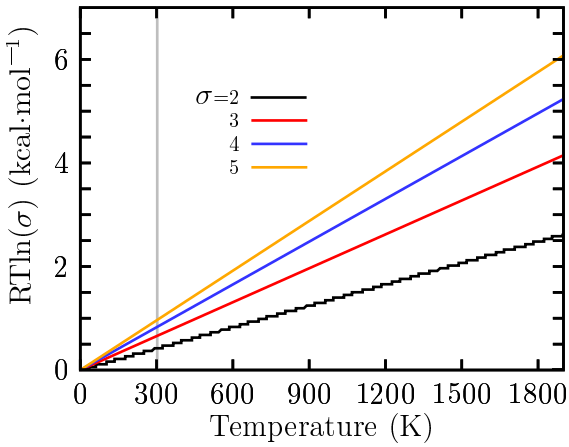

Figure 4.3: The difference of the rotational entropy with and without symmetries.

come larger. These small relative Gibbs free energies are responsible for differents values of probability of occurrence at low temperatures for the similar isomers with different point group symmetry. This strongly suggests that there must be atomic clusters with low and high symmetries in the Boltzmann ensemble to compute the molecular properties correctly. The second line in Table 4.1 shows single point (SP) relative energies computed at the CCSD(T)[237], the energetic ordering of isomers listed in the first line of Table 4.1 follows almost the trend of energetic ordering at SP CCSD(T) level, notice that just the achiral isomers label i_7 to i_8 in Table 4.1 are interchanged in energetic ordering. The third line Table 4.1 shows single point relative energies computed at the CCSD(T)[237]/def2-TZVP//PBE0-GD3/def2-TZVP; the energetic ordering is similar to pure CCSD(T) energy. DLPNO-CCSD(T)) realtive energies, with and without ZPE correction, are shown in lines four and five of Table 4.1, the first follows the trend of pure CCSD(T) energy, and the second, the ZPE value, interchange the isomers, label i_7 in Table 4.1, to be the putative global minimum. Here we can say that the ZPE energy inclusion is essential in distributing isomers and molecular properties. The sixth and seventh lines of Table 4.1 show the electronic energy with and without ZPE correction, and both of them follow the trend of the Gibbs free energy given in line number one. Line number 8 in Table 4.1 shows the point group symmetry for each isomer. The T_1 diagnostic for each isomer is shown inline nine of Table 4.1, all of them are lower than the recommended value 0.02 [237, 238] so the systems are appropriately characterized.

4.3.2 Structures and Stability at Finite Temperature.

As we mentioned earlier, the determination of the structure is the first step to study any property of a material. Moreover, we have to consider that an observed molecular property in a Boltzmann ensemble is a weighted sum of all individual contributions of each isomer that form the ensemble. At temperature 0 K, the elec-

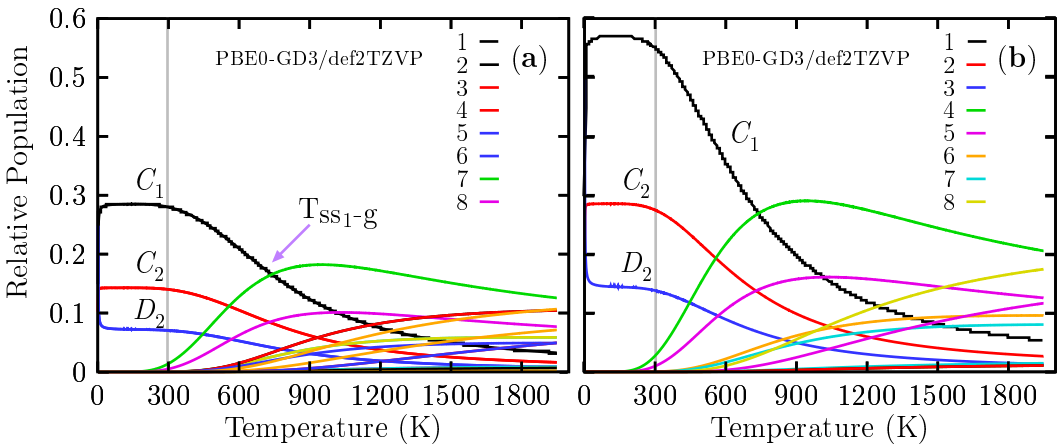

Figure 4.4: The left panels shows the probability of occurrence for temperatures ranging from 20 to 1900 K.

tronic energy plus zero-point energy determine the putative global minimum and all nearby low-energy structures (PGMLES), whereas, at temperatures larger than 0 K, the Gibbs free energy defines the PGMLES. Figure 4.4 shows the probability of occurrence for each particular chiral and achiral Be_4B_8 isomers for temperatures ranging from 20 to 1900 K. In panel (a) the probability of occurrence is shown, taking into account the $\mathcal{M}$,$\mathcal{P}$, and achiral structures, which implies Boltzmann racemic ensemble (the percent enantiomeric excess is zero (Boltzmann racemic ensemble). whereas panel (b) shows the probability of occurrence only taking into account just the $\mathcal{M}$ handled and achiral structures, which implies that the percent enantiomeric excess is 100%. then the ensemble is a Boltzmann pure ensemble of only one type of enantiomer. There is a significant difference in the probability of occurrence between the two panels. In panel (a), we consider the $\mathcal{P}$ and $\mathcal{M}$ structures, and both structures possess the same probability of occurrence in all ranges of temperature. All the probabilities of occurrence (chiral) shown in panel (b) are approximately two times the probability of occurrence (chiral) shown in panel (a). A closer examination of the panel (a) shown that in the temperature ranging from 20 to 300 K, all molecular properties are dominated by chiral structure depicted in Figure 4.1(a,b) becuase its probability of occurrence is almost constant. We point out that in this range of temperature, the C_1, C_2 and D_2 symmetries strongly dominate with different probabilities of occurrence of 28, 14 y 7% respectively. This different probability of occurrence for the same structure with only different symmetries is due to rotational entropy, that also is responsible for those slight energy differences shown in Table 4.1 and, in turn, it is the reason for the differences in the probability. At temperatures above 300 K, the probability of occurrence of the putative global minimum at cold temperatures and depicted in solid-black line decay exponentially up to 1900 K. The dominant transformation solid-solid point ($T_{ss_1\text{-}g}$) is located at 739 K with 16.6% of probability. At this point, there is a co-existence of chiral structures and

achiral structures, shown in Figure 4.1(a,g), above this point the achiral structure (Figure 4.1(g)) become dominant. Its probability of occurrence is depicted in the solid-green line in Figure 4.4a and start to grow up at almost at room temperature. The second transformation solid-solid point located at 1017 K and 10% of probability also coexist the chiral putative global minimum with symmetry C_1 and achiral structure (Figure 4.1(h)) located at 2.40 kcal/mol Gibbs free energy at 298.15 K above the putative global minimum. Figure 4.4b shows the computed probability of occurrence considering the percent enantiomeric excess is one hundred percentage, which implies of a pure Boltzmann ensemble of only one type of enantiomer. With the aim to compute the Boltzmann VCD/IR weighted spectra as a function of temperature, we take the relative population shown in Figure 4.4a. The probability of the dominant achiral putative global minimum with symmetry C_1 is depicted in the solid-green line in Figure 4.4a. Analysis of the probability of occurrence leads to an interesting observation: The individual putative minimum global strongly dominates the VCD/IR at a temperature ranging from 20 to 1240 K. The achiral structures have a zero contribution to VCD in hot temperatures. The probability of occurrence is dependent on the functional and basis set employed as a result of those energies computed at differents methods provides different energies [236] Figure B.1 shows the relative population computed at TSPP [239]-GD3/def2-TZVP level of theory. At cold temperatures, strongly dominate the chiral structure with symmetry C_1 and depicted in Figure 4.1(a,b). At hot temperatures, the dominant structure is a chiral helix-type structure depicted in Figure 4.1(k,l) located at 4.70 kcal/mol Gibbs free energy above the putative global minimum. Also, at SP CCSD(T) level, it is located at high energy above the global minimum. The relative population employing this functional does not follow the trend of energetic ordering at CCSD(T) level of theory. The above discussion shows that the probability of occurrence is sensitive to the functional.

4.3.3 Enantiomerization Energy Barrier at Finite Temperature.

The process in which pair of chiral molecules or enantiomers undergo to the conversion of one enantiomer into the other is referred to as enantiomerization. Enantiomers each have the same free energy and equal probability of occurrence, as shown in Figure 4.4 The extent of interconversion of enantiomers depends on the energy barriers to enantiomerization. Moreover, this energy barrier determines if an enantiomer can be resolved at temperature T and defines its configurational stability. There are cases where the enantiomerization is undesirable; for example, many drugs are related to chirality, and frequently only one of the enantiomers shows the desired effect while the other shows undesirable effects, moreover chiral molecules with high charge-carrier mobility and fluorescence quantum yield needs high energy barriers of enantiomerization. [240]

Figure 4.5a shows the computed enantiomerization energy barrier (energy activation (E_{ae}) or Gibbs free activation energy ($\Delta G^{\ddagger}$)) of the pair of enantiomers $\mathcal{P}$ and $\mathcal{M}$ of Be_4B_8 cluster that has only a single-step for two mechanisms of reaction

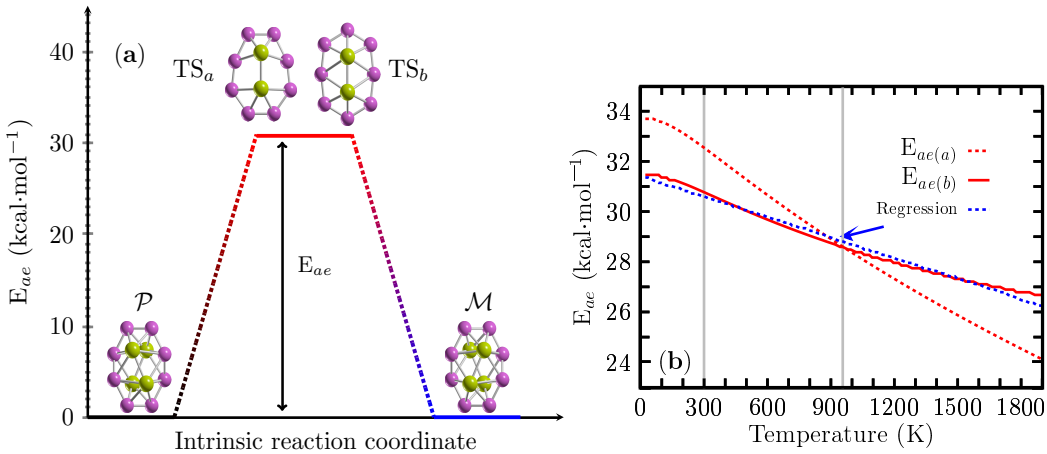

Figure 4.5: There are two transition states close in energy, TS$_a$ and Ts$_b$.

whose energy barriers are energetically similar. The transition states (TS$_a$, TS$_b$) depicted in Figure 4.5a, are achiral sandwich-type structures in which the borons form a planar ring with each of the Be-Be dimers capping the top and bottom, and thery are aligned parallel to the major axis of the boron ellipse. The main difference between both of them is a shift of ring position concerning the Be-Be dimers. The energy barriers of TS$_a$ and TS$_b$ are 32.50 and 30.77 kcal/mol, respectively, and indicates that Be_4B_8 enantiomers are stable at room temperature. Those energy barriers height are similar to that of computed energy barrier height in $Au_{38}(SR)_{24}$, [241] clusters that lie in the range of 29.9 to 34.5 kcal/mol. The energy of enantiomerization, E$_{ea(a)}$ and E$_{ea(b)}$ corresponding to the TS$_a$ and TS$_b$ for temperatures ranging from 20 to 1900 K are displayed in Figure 4.5b respectively. The E$_{ea(a)}$ is depicted in a red dashed line, whereas the E$_{ea(b)}$ is depicted in a red solid line. Analysis of the results leads to an interesting observation: In Figure 4.5b, one can see that there is a barrier-barrier temperature point (T$_{bb}$) located at 954 K where the energy barriers of both mechanisms are equal to each other. At T$_{bb}$, the probability that reaction takes one path or another is 50/50% which implies that the velocities of reaction for both reaction mechanism are equal to each other. Below the temperature of 954 K, the reaction path b (TS$_b$) is more favorable than reaction path a (TS$_a$), and vice-versa for temperatures above 954 K. In Figure 4.5b. is shows that the energy barrier E$_{ea(b}$ decreases linearly in the temperature range from 200 to 740 K. Below 200 K and in temperatures ranging from 740 to 1900 K; the energy barrier behavior is non-linear. To make it clearer, a line depicted in the blue dashed line in Figure B.3 appendix B.3 overlapping to energy barrier in the temperature range 200 to 740 K. Equation 4.1 was found by the linear regression, with correlation coefficients -0.9925, of the energy barrier depicted in a red solid line in Figure 4.5b.

$$\Delta G^{\ddagger} = 31.41 - 0.00271188 \cdot T \tag{4.1}$$

In Equation 4.1, T is the temperature, and it describes approximately the energy

Table 4.2: Approximate, energy barrier, enthalpy, entropy terms, and the percentage in which the energy barrier decreases

Temperature (K)	ΔG	ΔH	ΔS·T	%(Decrease)
0	31.41	31.41	0.0	0.0
300	30.60	31.41	-0.81	2.58
600	29.79	31.41	-1.62	5.17
900	28.97	31.41	-2.44	7.76
1200	28.16	31.41	-3.25	10.35
1500	27.35	31.41	-4.06	12.94
1800	26.53	31.41	-4.88	15.53

barrier in all ranges of temperature. It is depicted in the blue dashed line of Figure 4.5b. Evaluating Equation 4.1 with T=298.15 K gives 30.59 kcal/mol, just very close to the computed value of 30.77 kcal/mol. The first term of the Equation 4.1 is enthalpy, and the second one is the entropic term. The computed values of ΔG, ΔH, ΔS, and the percentage of contribution of ΔS to energy barrier are summarized in Table 4.2 for some temperature values. Analysis of results shown in Table 4.2 leads that the enthalpy term is too large compared with the entropic term shown in row 3 and row 4 of Table 4.2, respectively, and evaluated in ranging temperatures given in row 1 of Table 4.2. In row five of Table 4.2 is given the percentage in which the energy barrier decreases as a function of temperature and due to entropic term considering as reference one hundred percent when the energy barrier is computed at T=0. Notably, the composition of the energy barrier is enthalpic and is too high in all ranges of temperature. We concluded that the interconversion between enantiomers is thermodynamically unfavorable in all ranges of temperature based on our computations. At hot temperatures, the energy barrier still is too high, and the most significant entropic contribution is not more than 15.54%. Similar results are obtained for the TS_b.

4.3.4 Energy barrier between chiral and achiral structures at finite temperature.

Figure 4.6a displays the height of energy barrier interconversion at room temperature between the chiral $\mathcal{P}/\mathcal{M}$ structures shown in Figure 4.1(1,2), and achiral structure depicted in Figure 4.17. Remarkable, these structures coexist at the dominant solid-solid transformation point located at 739 K, and according to the probability of occurrence, at hot temperatures, the achiral structure is the putative global minimum. Furthermore, the endergonic to an exergonic temperature point, Tee, is defined here as the temperature where the reaction type change from an endergonic to an exergonic and in this Be_4B_8 clusters it coincides with the solid-solid transformation point. When these two points coincide, at least two structures coexist, and there is a change of type reaction from endergonic to an exergonic or vice-versa.

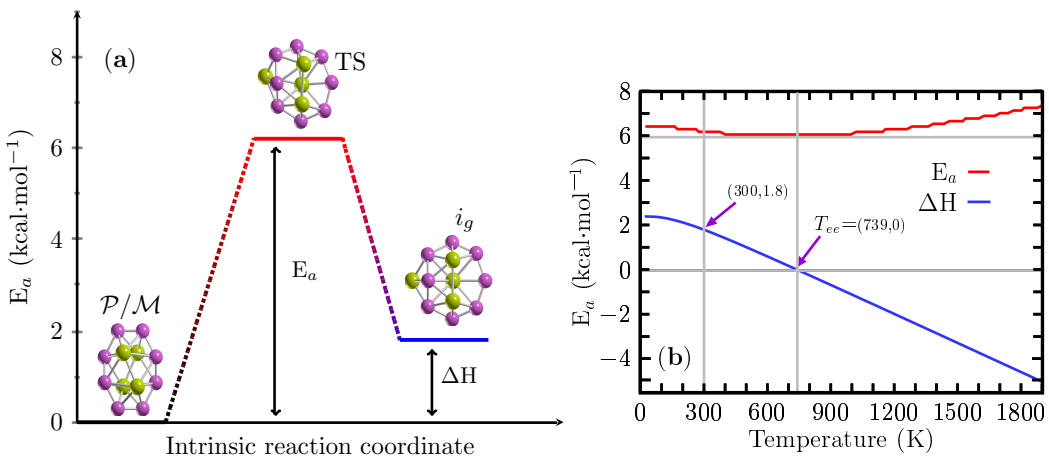

Figure 4.6: The height of energy barrier.

For the interconversion between those structures, the height of the energy barrier at room temperature is 6.20 kcal/mol, and the enthalpy of formation (AH) is 1.8 kcal/mol. The TS is depicted in Figure 4.6a, it is also a sandwich type structure formed by a distorted circular ring in which the Be-Be dimers are capping each faces of the ring, it has similar structure to isomer i_7 depicted in Figure 4.1(g). Figure 4.6b shows the height of the energy barrier for chiral and achiral structures depicted in a red solid line, the enthalpy of formation (ΔH)) for the same structures is depicted in a solid blue line for temperatures ranging from 20 to 1900 K. An analysis of ΔH in Figure 4.6b, shows that the reaction process is endothermic for temperatures ranging from 20 to 739 K because the ΔH is positive. At the temperature of 739 K, the ΔH is zero, which implies that the chiral structure with C_1 symmetry and achiral (i_7) structure with C_1 symmetry coexist. The above discussion is in good agreement with the computed point T_{ss-1} located at 739 K displayed in Figure 4.4a, and according to the probability occurrence, at this point, the chiral and chiral structures coexist. Furthermore, in this temperature point, the height of the energy barrier, depicted in the red-solid line Figure 4.6b, has a minimum value of 6.0 kcal/mol. At temperatures above 739 K, the reaction process is exothermic due to the ΔH is negative, and the height of the energy barrier starts to increase slowly. Analysis of results in more detail leads to several observations. The reaction process is endothermic up to 739 K, which implies the absorption of energy, and the chiral structures strongly dominate as the putative global minimum. At temperatures of 739 K, the chiral and not chiral structures coexist. At temperatures above 739 K, the reaction process is exothermic, which implies a heat of reaction, and the non-chiral structures weakly dominate as the putative global minimum. Based on the ΔH behavior in all ranges of temperature, we point out that the reaction is an entropic-driven process due to that type of reaction change from endothermic to exothermic as the temperature increases.

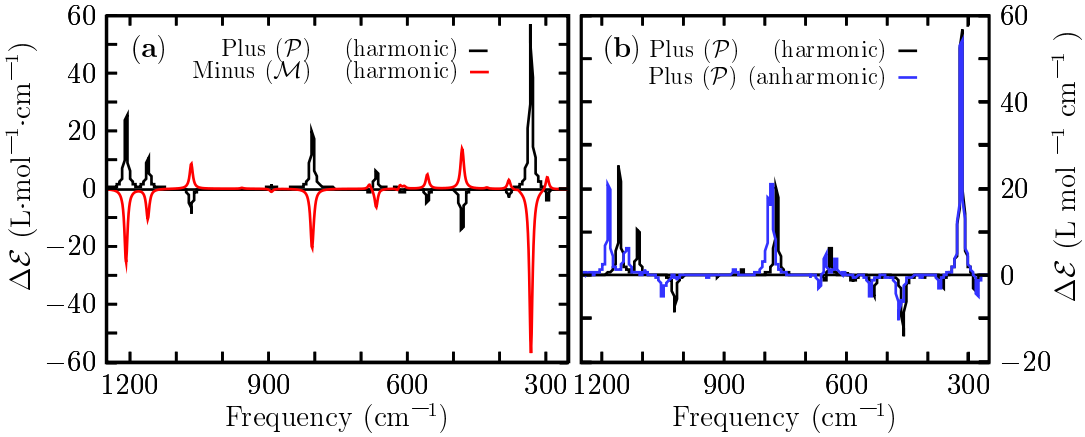

Figure 4.7: The panels Shows a comparison of the VCD spectrum.

4.3.5 VCD and IR spectra

Figure 4.7a. shows a comparison of the VCD harmonic spectra corresponding to $\mathcal{P}$ and $\mathcal{M}$ lowest energy structures depicted in solid black- and red lines, respectively. They show a mirror image relationship, thereby ensuring that the two structures are non-superposable. The computed VCD spectrum ($\mathcal{P}$ structure) is characterized by five main peaks located at frequencies of 330 cm^{-1}, 481 cm^{-1}, 802 cm^{-1}, 1062 cm^{-1}, and 1208 cm^{-1} respectively. The largest peak positive intensity is located at 330 cm^{-1}, and it corresponds to the stretching of the two Be-Be dimers that capped the distorted boron ring. Next, a transition located at 481 cm^{-1} is the largest negative and is attributed to bending of the boron distorted ring, a kind of breathing motion. The peaks located in the region 1062 cm^{-1} to 1208 cm^{-1} corresponds to ring boron stretching. The harmonic approximation works if the potential energy is parabolic and it fails [242] as the temperature increases due to anharmonic effects [242] Under harmonic approximation, strongly anharmonic systems are not well described [243, 244] For high temperatures above 0.7...0.8 melting temperature, explicit anharmonic contributions become relevant, [245] moreover, we have to consider if the cluster whether or not it is highly strongly anharmonic. To estimate the importance of anharmonicities of the Be_4B_8 chiral cluster, we show, In panel (b) of Figure 4.7b the anharmonic VCD spectra that is depicted in solid blue line, and for ease comparison overlaying with the harmonic vibrational spectrum depicted in solid black line, both of them computed for $\mathcal{P}$ lowest energy structure, and employing Gaussian code. [51] A shifting factor of 0.96 is applied to shift the harmonic spectrum to overlaying the anaharmonic spectrum. We found that the frequency shift is 14 cm^{-1} towards to high energy. A comparison of two spectra displayed in Figure 4.7b shows that The computed harmonic and anharmonic spectra are in very good agreement. In fact, most of the peaks are correctly computed employing the harmonic approximation. In the low range of energy the harmonic peaks and anharmonic peaks agree well, however, there are slightly discrepancies in

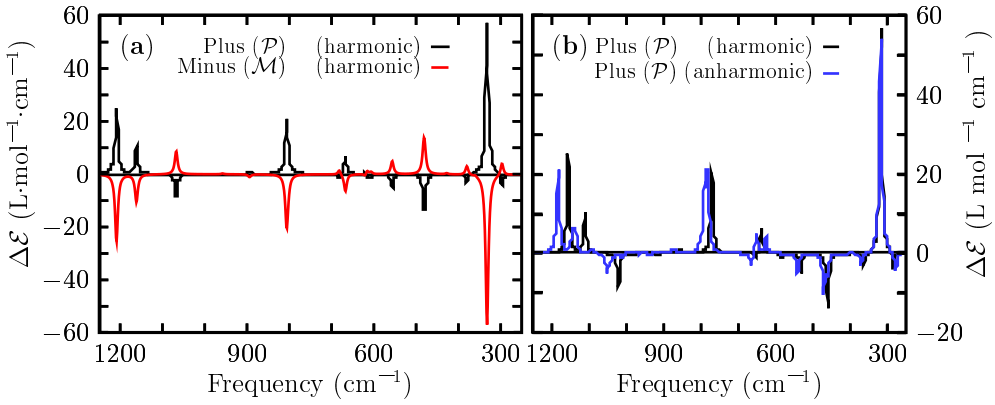

Figure 4.8: The dependent temperature IR Boltzmann-spectra-weighted.

the region 1100 cm^{-1} to 1200 cm^{-1}, nevertheless, in this study the computations of the thermodynamic properties and VCD spectra under the harmonic approximation yield reliable results enough to describe the non-strongly anharmonic Be_4B_8 chiral cluster. Additionally, the Figure B.4, appendix B.4 show the IR spectra computed under harmonic and anharmonic approximations. The IR-harmonic spectrum is depicted in solid black line, whereas, the IR-anharmonic spectrum is depicted in solid red line. A shifting factor of 0.96 is applied to match the IR-harmonic spectrum over the IR-anharmonic spectrum. Comparing both spectra, it can see that the spectra match over a large range of frequencies. From the above mentioned we infer that the IR spectra under harmonic approximation yield valid results. Regarding dependent-temperature VCD spectra, the Boltzmann weighted overlapping to yield a total VCD spectrum at all ranging temperatures is zero because the Boltzmann ensemble is composed of achiral structures and an equal mixture of both $\mathcal{P}$ and $\mathcal{M}$ enantiomers, which implies that the Boltzmann ensemble is racemic. Any chiroptical response in the Be_4B_8 cluster is going to be null. The exhaustive exploration of potential and free energy surface revealed that there are twenty two isomers within an energy range of 9.2 kcal/mol, six of which are chiral structures, with symmetries C_1, C_2, D_2 respectively, and were within 1 kcal/mol. Moreover, these structures compose 98% of relative population at room temperature. With the aim to compute Boltzmann weighting IR spectra, those structures which only differs on symmetries has to be taken into account The IR spectra, in comparison to VCD spectra, is not null. Figure 4.8 shows the IR spectra for temperatures ranging from 50 to 1900 K. The IR spectrum is composed of five peaks. The largest peak intensity is located 330 cm^{-1} frequency axis it corresponds to the alternating stretching of the two Be-Be dimers that capped the distorted boron ring, and it is a mode that contributes to interconversion between P and M structures, The other four modes are related to compression/expansion of the boron ring.

Figure 4.8a display the IR spectra for temperatures ranging from 50 to 300 K, in this range, the IR spectra is strongly dominated by the spectrum of the lowest

energy pair of enantiomers with C_1 symmetry, and further the IR intensities remain constants in all range of temperatures. The above mentioned, is in agreement with the relative population depicted in Figure 4.4a where the probability of occurrence of the pair of enantiomers with symmetry C_1 strongly dominate. We have to consider that the contribution to IR spectra of the four enantiomers with C_2 and D_2 symmetries for temperature ranging from 20 to 300 K is equal to the IR spectrum with symmetry C_1, and there is not presence of other structure. Thus at room temperature all molecular properties, except for the chiral properties, are attributable to the lowest energy pair of enantiomers, depicted in Figure 4.1(a,b). Panel (b) of Figure 4.8 shows the IR spectra for temperature ranging from 400 to 700 K. The IR intensities start with exponential decay, in agreement with the probability of occurrence of the lowest pair of enantiomers of Figure 4.4a. There is a little contribution from other isomers, but not enough to change/alter the IR spectrum. Thus the shape of IR spectrum remains equal to IR spectrum at cold temperatures. The IR spectra for temparatures ranging from 800 to 1200 K are shown in Figure 4.8c, the largest contribution of a particular isomers is less than 17% thus the largest peak of IR spectra trend to be neglected. Panel (d) in Figure 4.8 displays that the IR spectra is almost null, thus at hot temperatures the IR spectra is neglected because of almost all contributions of the isomers to IR spectum are around 10%.

4.3.6 Molecular Dynamics

We perfomed a Born-Oppenheimer molecular dynamics employing the deMon2K program [189] (deMon2k v. 6.01, Cinvestav, Mexico City 2011) at different temperatures (1200, 1500 and 1800 K), with the aim to gain insights into the dynamical behavior of Be_4B_8 cluster. We employed similar parameters that in a prevoius work. The simulation time was of 25 ps with a step size of 1 fs. For Be_4B_8 cluster we found a dissociation phenomena when the temperature is higher than 1500 K, at 1800 K the dissociation process is stronger, while at 1200 K there is no dissociation. When at temperature T, a cluster dissociate the melting point temperature is lower that temperature of dissociation. [246, 51] a [2, 1, 16, 65, 64, 63]

4.4 Conclusions

For the first time, to our knowledge and from our results, we found that the chiral cluster Be_4B_8 is the lowest energy structure.

Chapter 5

The Cu_{13} cluster

5.1 Abstract

This chapter reports the lowest energy structure of bare Cu_{13} nanoclusters as a pair of enantiomers for temperatures ranging from 20 to 1200 K. Moreover, we compute the enantiomerization energy for the interconversion from $\mathcal{M}$ to $\mathcal{P}$ structures in the chiral putative global minimum for temperatures ranging from 20 to 1300 K. Additionally, employing statistical thermodynamics and nanothermodynamics, we compute the Boltzmann Probability for each particular isomer as a function of temperature. To achieve that, we explore the free energy surface of the Cu_{13} cluster, employing a genetic algorithm coupled with density functional theory and statistical thermodynamics. Moreover, we discuss the energetic ordering of structures computed at the DFT level and compared to high level DLPNO-CCSD($\mathcal{T}_1$) reference energies, and we present chemical bonding analysis using the AdNDP method in the chiral putative global minimum. Based on the computed relative abundances, our results show that the chiral putative global minimum strongly dominates for temperatures ranging from 20 to 1100 K.

5.2 Introduction

Transition-metal (TM) nanoclusters have been widely studied due to their potential applications in catalysis [247, 248, 249], photoluminescence [250], photonics [251], magnetism [250], chirality [252], and the design of new materials [253, 254]. Cu is a 3d TM with several oxidation states [255, 256], which explains its reactivity and confers many interesting physical and chemical properties [255, 256]. Moreover, the high boiling point of Cu makes it compatible with high-temperature chemical reactions. Clusters are aggregates of atoms at the nanoscale size, which exhibit unusual physicochemical properties [257]. Cu clusters are particularly fascinating due to their applications in catalysis [256], light-emitting devices [258], and nanotechnology [259], despite presenting some challenges such as their easy oxidation [259]. The most stable structure of small Cu clusters has been investigated by density functional theory (DFT) studies [260, 261, 262, 263] and considering the *Jahn-Teller effect* [264]. In the early 2000s, Poater *et al.* [265] characterized neutral copper clusters (Cu_n n = 1-9) using computed chemical reactivity descriptors within the DFT framework. Later, atomic structures and reactivity descriptors of Cu_nCO (n = 1,9) were computed and discussed [265]. Calaminici *et al.* reported the structure

of neutral and anionic Cu_9 clusters, employing DFT [266]. Moreover, in previous combined theoretical-experimental studies, the computed removal energies were compared with the measured photoelectron spectra in anionic Cu_n (n= 9,20) clusters [267], and later, the optical absorption of small Cu clusters was presented [268]. Based on their geometry and electronic structure, atomic clusters could be characterized by magic numbers [269, 247, 270, 271] that form highly symmetric structures; for example, icosahedron (ICO) and cuboctahedron (CUB) shapes [247]. From the geometrical point of view, the first magic number that appears is 13. Experimental studies have found magic TM_{13} clusters for Fe and Ti, amongst others [272, 247]. Previous theoretical studies based on the empirical potential of Cu_{13} clusters showed that the low-energy structures were the icosahedron and the cuboctahedron [273]; those structures consist of a central atom surrounded by 12 Cu atoms. In contrast, Guvelioglu *et al.* [274], within the framework of DFT, found that the lowest energy structure of Cu_{13} is the double-layered structure, and in the same year Itoh *et al.* [275] reported a similar double-layer structure as the putative global minimum. Yang *et al.* explored the structural evolution of Cu_n (n = 8-20) anions and found platelike structures [276]. Later, larger Cu_n (n = 20-30) clusters were investigated, and it was found that the structures are based on a 13-atom icosahedral core [277]. In the previous studies, Cu_{13} was investigated because it was found to have an icosahedral structure that has a high percentage of edge and corner sites and high-index facets, resulting in increased catalytic activities [278, 279, 280]. In most cases, low-energy Cu clusters have preferentially lower symmetry structures [281], although some present distorted structures [281, 282]. Although there are many studies on Cu clusters, the chirality of Cu_{13} clusters has not been discussed. In general, chirality plays a decisive role in biological activity and life processes. [88]. Remarkably, chiral nanoclusters have attracted attention because they have applications in chiral materials with novel properties [283, 87, 2]. Recently, theoretical studies on beryllium boron cluster Be_4B_8 at the DLPNO-CCSD($\mathcal{T}_1$) theoretical level found chiral structures as the lowest energy structures [2]. Previous theoretical studies on PtPd co-doped silicon clusters reported chiral and fluxional low-energy structures [284]. Recently, Kong *et al.* reported propeller-like chiral AIE copper (I) clusters with exciting properties [285]. However, clusters properties depend on their putative global minimum and low-energy structures, considering achiral and chiral structures. Hence, we need to know the distributions of isomers at different temperatures [1, 2, 16]. The lowest- and low-energy geometries, composition, and temperature of the ensemble determine all the properties of a cluster at temperature T [1, 286, 16], i.e., its electronic, structural, thermodynamics, vibrational, and optical properties, as well as its chemical reactivity. Moreover, the atomic structure is the first level at which it is possible to manipulate the macroscopic properties of a cluster.

In this chapter, intending to elucidate the lowest- and the low-energy structures of neutral Cu_{13} clusters at finite temperature, we explored their free energy surface by employing a genetic algorithm coupled to DFT, statistical thermodynamics and nanothermodynamics. We computed the probability of occurrence of each particu-

lar isomer, employing Boltzmann probabilities for temperatures ranging from 20 to 1500 K. Our findings show that the putative global minimum is a chiral structure at room temperature. Moreover, we computed the transition state (TS), i.e., the enantiomerization energy for temperatures ranging from 20 to 1300 K, for interconversion of a pair of enantiomers (Plus, $\mathcal{P}$, and Minus, $\mathcal{M}$). Our computations showed that enantiomerization barriers led to persistently chiral structures and enabled the complete separation of enantiomers at room temperature [287, 2]. The remainder of the manuscript is organized as follows. Section 2 provides the computational details and a brief overview of the theory and the algorithms used. The results and discussion are presented in Section 3. We discuss the low-energy structures, the effect of the DFT functionals on the energetic ordering of isomers and comparison to DLPNO-CCSD($\mathcal{T}_1$) [288] reference energies; T1 diagnostic is presented. The effect of the symmetry number on the Gibbs free energy and on the thermal populations at temperature T; and the origin of the slight 0.41 kcal/mol energy differences are investigated. We analyze the interconversion energy barrier between $\mathcal{P}$ and $\mathcal{M}$ enantiomers, the effects of the temperature in the energy barriers, and the thermal population.

5.2.1 Computational Details

All geometrical structures are optimized locally without imposing any symmetry, the self-consistent-field procedure was performed with a convergence criterion of 10^{-6} a.u. The energy, maximum force and maximum displacement convergence were set to 10^{-6} Ha, 0.002 Ha/Å and 0.0005 Å respectiveley. All calculations were performed using the Gaussian suite code [14] employing the Beck's hybrid three parameter [289, 6] exchange-correlation functional in combination with the Perdew and Wang GGA functional PW91, [290, 291] this combination is known as B3PW91 exchange-correlation functional. The B3PW91 has been employed in other studies of reactivity in copper clusters with a good performance [292, 293], It is worth point out that hybrid functionals including a portion of Hartree-Fock exchange have shown a superior performance [292, 294, 295]. For the basis set, we employed the The LANL2DZ basis set is used for transitions metals due to its low computational cost [296] With the aim to refine the optimization and the energies, we used Ahlrichs-type triple-ζ quality extended valence def2TZVP basis [297, 298] that is more accurate for transition metals [299] despite it has a considerably higher computational cost. [300] In this study the dispersion corrections are taking into account trough the D3 version of Grimme dispersion [181] as it is implemented in Gaussian code. In a previous work, the effect of the dispersion corrections on the structural and energetic properties of the pure BeB clusters were studied founding that the energetic ordering of isomers can change when the dispersion is taking into account [1, 2]. Transition states are discarded through a vibrational analysis, making sure that the minimum energy structure is a true structure minimum energy. Calculation of Gibbs free energy properties of Cu_{13} cluster requieres an exhaustive and systematic sampling of the free energy surface with the aim to find all possible low-energy

structures. [1, 301] First of all, the search of the global minimum in atomic clusters is a complicated task due mainly that degrees of freedom of a molecule increases with the number of atoms; as a consequence, the number of local minimum increase exponentially with the number of atoms, moreover the calculated total energy of the cluster requisites high level of quantum mechanical methodology to produce a real energy. In spite of that, several algorithms coupled with DFT to search the lowest energy structures on the potential energy surface of atomic clusters has been employed until nowadays, as kick methodology [302, 41, 303, 44, 48, 47, 49, 304], genetic algorithms [1, 28, 3, 29, 30] Our computational procedure to elucidate the lowest energy consisted of employing a hybrid genetic algorithm called *GALGOSON* [1, 2] *GALGOSON* employ a multi-step search strategy where in the first step it makes optimizations employing LANL2DZ basis set and in second step-refine it employs the def2TZVP basis set, the creation of the initial population take into account the 2D and 3D structures [28, 42] with an initial population of 650 random structures for the Cu_{13} cluster and the criterion to stop the algorithm is until the five generations converged. This methodology based on previous works [305, 238, 3] consists of a multi-step approach (cascade) to efficiently sample the potential/free energy surface coupled to the *Gaussian* code [51]. Chemical bonding was examined using the Adaptive Natural Density Partitioning (AdNDP) method [92, 2]. AdNDP analyses the first-order reduced density matrix and recovers Lewis bonding (1c-2e or 2c-2 e, i.e., lone pairs (LPs) or two-center two-electron bonds) and delocalized bonding elements (associated with the concept of electron delocalization).

5.3 Results and Discussion

5.3.1 The lowest energy structures and energetics

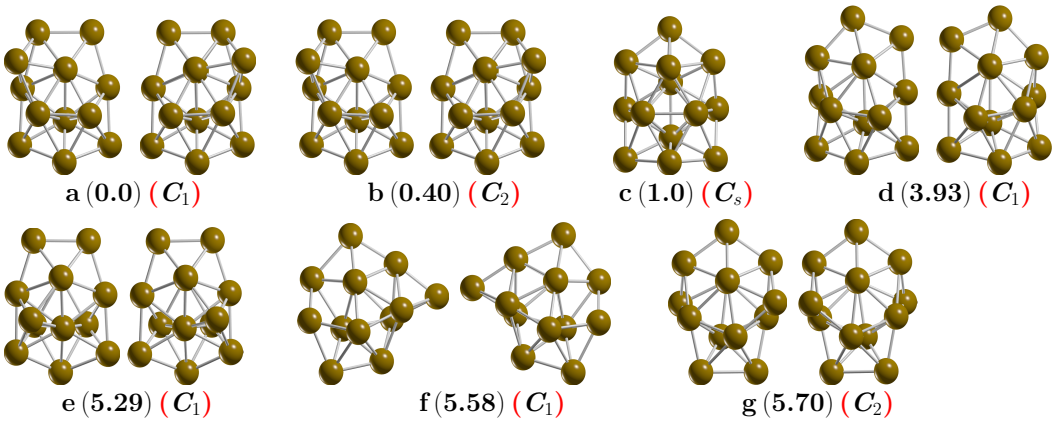

Figure 5.1: The chiral and achiral lowest energy structures.

The most important low-energy structures of a neutral Cu_{13} cluster optimized at the B3PW91-GD3/def2TZVP level of theory found in this study are shown in

Figure 5.1. At room temperature, the isomers depicted in Figure 5.1 contributed to 94% of the molecular properties in a Boltzmann ensemble; thus, almost all molecular properties were due to those isomers. Additionally, they are chiral structures. The putative chiral global minimum is depicted in Figure 5.1a with symmetry C_1. These are bilayered structures composed of a shared pentagonal bipyramid interspersed with a distorted hexagonal ring with a Cu atom capping one of its faces and two Cu atoms capping the other face of the hexagonal ring, in good agreement with similar structures [306, 274, 307]. The pentagonal bipyramid interspersed with the hexagonal ring is built with 12 Cu atoms. One more Cu atom caps the pentagonal bipyramid; this capping Cu atom is responsible for the chirality of the Cu_{13} cluster. Our calculated Cu-Cu bond length on the putative chiral global minimum is 2.432 Å, in good agreement with other reported DFT calculations of a Cu-Cu dimer of 2.248 Å [308] and also with an experimental bond length of 2.22 Å [309, 310], just slightly above 5.3% of the experimentally determined value. The calculated vibrational frequency of Cu_{13} was 60 cm^{-1}, whereas the computed vibrational frequency of the Cu-Cu dimer was 245 cm^{-1}, again in good agreement with the experimental value of 265 cm^{-1} [310]. We also explored the higher multiplicity of quartets and found that the lowest energy structure lay 20.5 kcal/mol above the doublet putative chiral global minimum energy structure. The second structure that was higher in free energy lay at 0.41 kcal/mol at room temperature; it was also a bilayered structure, similar to the putative global minimum, but with C_2 symmetry. Iwasa *et al.* [311] reported a similar double-layer structure as a putative global minimum with C_2 symmetry, but without taking into account the temperature. One of our previous studies showed that these tiny Gibbs free energy differences are derived from rotational entropy [2]. The C_1 and C_2 symmetry clusters adopted a hollow layered structure. The following higher energy isomer lay at 1.0 kcal/mol at room temperature and was an achiral buckled-biplanar (BBP) structure with C_s symmetry, which agrees with previous work [312]. At room temperature, its contributions to the molecular properties were less than 6%. The average bond length on isomer BBP was 2.432 Å, similar to the average bond length of the chiral putative global minimum. Next, higher energy structures lay 3.9 kcal/mol above the chiral putative global minimum, and their average bond length was 2.444 Å, slightly larger than the average bond length of 2.432 Å of the putative global minimum. This also appeared as a bilayered chiral structure with a shared hexagonal bipyramid interspersed with a hexagonal bipyramid. The following higher energy structure lay 5.29 kcal/mol above the putative minimum global. It was a bilayered structure consisting of 12 atoms, with 1 atom capping one of its faces. It is depicted in Figure 5.1e. Structures located at higher energy than 5.5 kcal/mol above the putative global minimum are depicted in Figure 5.1f,g. Those structures also adopted a layered structure with no interior atoms, with similar morphology to that of low-energy isomers. These two structures did not contribute to the molecular properties in the studied temperature range. The Cu_{13} cluster low-energy structures preferentially adopted morphologies of bilayered structures rather than highly symmetric 3D structures. In contrast, Au_{13} clusters prefer planar structures due to relativistic effects [281]; therefore, fur-

ther studies are needed to investigate why bilayered structures in the Cu_{13} cluster are energetically preferred. For the Cu_{13} cluster, the icosahedron structure is not energetically favorable in the temperature range examined, which is consistent with previous work where the authors did not take into account the temperature [247]. In this study, the icosahedron structure was located at 24.6 kcal/mol above the putative global minimum at room temperature. To get an idea of the bonding situation

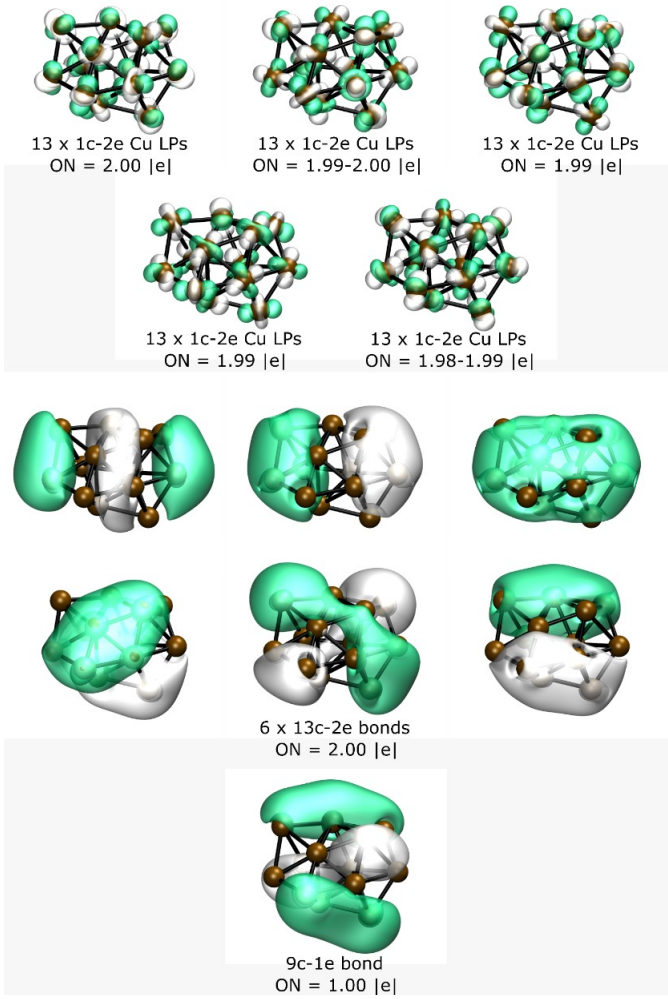

Figure 5.2: Results of the AdNDP analysis of the lowest-energy chiral isomer of the Cu_{13} system.

in the chiral putative global minimum structure, we performed an AdNDP analysis; the results are shown in Figure 5.2. This analysis revealed the presence of 5 sets of 13 1c-2e bonds with occupation numbers (ONs) between 1.98 and 1.99 |e|, i.e., lone pairs (LPs) corresponding to the fully filled 3d shell in each Cu atom. The bonding in this cluster was then due to the 4s shell electrons for which the bonding

pattern, as revealed by AdNDP, consisted of 6 sets of 13c-2e completely delocalized bonds, plus a 9c-1e bond corresponding to the unpaired electron which, as shown in Figure 5.2, was mostly delocalized in the peripheral atoms of the cluster.

5.3.2 Energetics

Table 5.1: Relative energy in kcal/mol of the low-lying isomers depicted in Figure 5.1 labeled from a to f.

	Isomers									
Level	i_a	i_a	i_b	i_b	i_c	i_d	i_d	i_e	i_e	i_f
ΔG(B3PW91)	0.0	0.0	0.3953	0.4091	0.9946	3.9338	3.9357	5.2967	5.2967	5.5728
ΔG(TPSS)	0.0	0.0	0.4010	0.4016	0.7248	5.6017	5.6029	5.5477	5.5477	7.5438
ΔG(PBE)	0.0	0.0	0.4145	0.4217	0.5491	3.8478	3.8491	5.5283	5.7284	5.7310
ΔG(BP86)	0.0	0.0	0.4079	0.4035	0.8634	3.5611	5.4291	5.4291	5.2817	7.2798
DLPNO-CCSD(T)	0.0	-0.1298	-0.2154	-0.2144	0.6827	5.0246	5.8771			
DLPNO-CCSD(T)+$\mathcal{E}_{\text{ZPE}}$	0.0	-0.1298	-0.2216	-0.2170	0.7084	4.9022	5.7886			
$\mathcal{E}_0 + \mathcal{E}_{\text{ZPE}}$	0.0	0.0	0.0	0.0	0.9262	4.5877	4.5877	5.6124	5.6124	6.3327
$\mathcal{E}_0$	0.0	0.0	0.0	0.0	0.9002	4.7096	4.7098	5.7013	6.4969	6.4966
Point group symmetry	C_1	C_1	C_2	C_2	C_s	C_1	C_1	C_1	C_1	C_1
$\mathcal{T}_1$ Diagnostic	0.023	0.023	0.023	0.023	0.023	0.023	0.023	0.023	0.023	0.023

Temperature drastically affects the Gibbs free energy of the isomers; therefore, in a molecular ensemble (collection), the energetic ordering of isomers changes. Besides, from a theoretical point of view, the energetic ordering can also change when computing energies using different levels of theory [1, 313]. To wit, energy computed at different methods yield different energies due mainly to the functional and basis-set employed, [1], so the energetic ordering change; consequently, the probability of occurrence and the molecular properties will change. Moreover, we compute the $\mathcal{T}_1$ diagnostic to determine if the computed DFT energies are properly described by a single reference method or contain a multireference character. To gain further insight into the energetic ordering of the low-lying isomers, we optimized the low-lying energy structures employing three more DFT functionals: TPSS [314], PBE [7], and BP86 [6] with def2-TZVP basis set, and single point (SP) relative energies computed employing the domain-based local pair natural orbital coupled-cluster theory (DLPNO-CCSD(T)), with TightPNO setting [288], and with and without ZPE energy correction. The purpose was to ascertain the origin of the slight 0.41 kcal/mol differences (below the chemical accuracy of 1 kcal/mol) in the relative Gibbs free energy (Table 5.1) and that these are not due to numerical errors, algorithmic approximations, integration grids, or functional and basis set dependence, to name a few. In Table 5.1, lines first through the fourth show the relative Gibbs free energies computed at B3PW91-D3/def2-TZVP, TPSS-D3/def2-TZVP, PBE-D3/def2-TZVP, and BP86-D3/def2-TZVP, respectively. DLPNO-CCSD(T)) relative energies, with and without ZPE correction, are shown in the fifth and sixth line of Table 5.1, electronic with zero-point energy and electronic energy, at the B3PW91-D3/def2-TZVP level of theory are shown in the seventh and eighth lines of Table 5.1, and

line ninth shows the point group symmetry, the $\mathcal{T}_1$ diagnostic for each isomer is shown in line tenth of Table 5.1, our results confirm that the computed $\mathcal{T}_1$ diagnostic values are slightly above the recommended threshold of 0.02 [315, 2]; So, these values suggest that multireferential studies have to be carried out for Cu_{13} cluster. At the CCSD(T) theoretical level, the lowest-energy structure is the pair of enantiomers with symmetry C_2; despite that, at finite temperature, the lowest energy structure is the pair of enantiomers with symmetry C_1. A more detailed analysis of the results in Table 5.1 shows that the relative electronic energy of the four chiral low-energy isomers labeled in Table 5.1 (a, b, c, d), with symmetry C_1, C_1, C_2, and C_2, respectively, is zero, considering the ZPE; also the relative electronic energy is zero. In contrast, the relative Gibbs free energy at 298.15 K shown in the fifth column is 0.41 kcal/mol. The relative Gibbs free energy at 298.15 K for the TPSS, PBE, BP86 DFT-functions, between the putative global minimum and the second isomer, is also 0.41 kcal/mol. This Gibbs free energy difference does not depend on the functional employed, as shown in Table 5.1. At temperature T=0, the total energy of an isomer is the electronic energy plus ZPE ($\varepsilon_0 + ZPE$). If the temperature increases, entropic effects start to play, and Gibbs's free energy determines the global minimum. At any temperature T, the isomers, represented in Figure 5.1 and Figure 5.1b, differ only in molecular symmetry. The isomer with C_2 symmetry has a Gibbs free energy equal to RTIn(σ) less than the non-symmetric C_1 isomer. Here R is the universal gas constant, T temperature, and σ is the symmetry number. The symmetry number appears in the denominator of the molecular rotational partition function [316, 1, 2, 317]. This implies that the less symmetric isomers at finite temperature are more thermodynamically stable than the more symmetric ones due to the energy factor given by RTIn(σ). The factor becomes zero at T=0 and increases linearly with temperature. Figure 5.3 shows the factor as a function of temperature

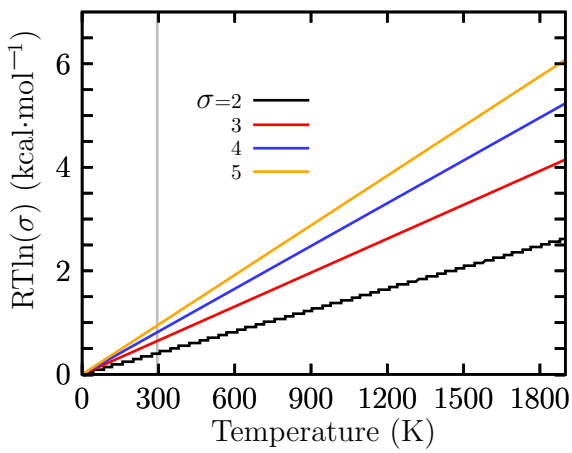

Figure 5.3: The difference of the Gibbs free energy with and without symmetry.

and for different symmetry numbers. Moreover the $\mathcal{T}_1$ diagnostic indicate that a multireference c For our optimized low-energy isomers with C_2 symmetry, the sym-

metry number is 2, so the Gibbs free energy at 298.15 K with and without symmetry will differ by 0.41 kcal/mol regardless of the DFT method. This value is higher at high temperatures and with higher symmetry numbers. For example, the benzene molecule with D_{6h} symmetry has a symmetry number 12, the Gibbs free energy at 298.15 K with and without symmetry will differ by 1.47 kcal/mol, which is greater than the chemical precision. Here, we call this the effect of the symmetry number on the Gibbs free energy and on the thermal populations at finite temperature; the symmetry number appears when identical atoms are considered indistinguishable and are determined solely by the point group symmetry of the molecule. We emphasize the importance of symmetry in calculating thermal populations at absolute temperature T or the so called population probability or relative populations, hence the molecular properties. For example, the melting temperature for a symmetrical molecule is higher than a non-symmetrical molecule; moreover, the activation energy barrier could be higher when we consider a non-symmetrical molecule in the calculation of the transition state. The energy computed at different theoretical levels influences the energy distribution of the isomers and, as a consequence, the Boltzmann weights. For the four DFT functionals used in this study, the energy ordering is preserved, although differences in the energy between the isomers occur; for each DFT functional, the main contributors to any molecular property of Cu_{13} are always the chiral isomers depicted in Figure 5.1a.

5.3.3 Structures and Stability at Finite Temperature.

In chemistry, physics, and biology, the lowest energy structure and all the low-energy structures near the global minimum are crucial because all molecular properties are statistical averages derived from the ensemble of molecular conformations [2]. The probability of occurrence of each particular isomer is depicted in Figure 5.4 for the Cu_{13} cluster. It was determined by employing Equation 3.1 and temperatures ranging from 20 to 1500 K at the B3PW91-D3/def2TZVP level of theory. Figure 5.4 shows the probability of occurrence considering all chiral and achiral structures. The analysis of these results led to an interesting observation. The pair of enantiomers that appeared as the putative global minimum at temperature 0 K was strongly dominant in the temperature range from 20 to 1500 K. Moreover, there were no solid-solid transformation points in any temperature range, which means no interchange of dominant low-energy structures at high temperatures. A closer inspection of Figure 5.4 shows that the decay of probability of occurrence of the pair of enantiomers with symmetry C_1, depicted by a red solid line, is closer to linear rather than exponential for temperatures ranging from 20 to 600 K. Above 600 K and up to 1500 K, the decay is exponential. At 300 K, the chiral structure has a probability of 32%, whereas the second isomer located 0.4 kcal/mol above the putative global minimum has a probability of 16%. The above discussion shows that all molecular properties of the Cu_{13} cluster are attributed to the chiral putative global minimum at absolute temperature zero. The probability of occurrence of the chiral putative global structures, is depicted by blue and yellow solid lines in Figure 5.4. The

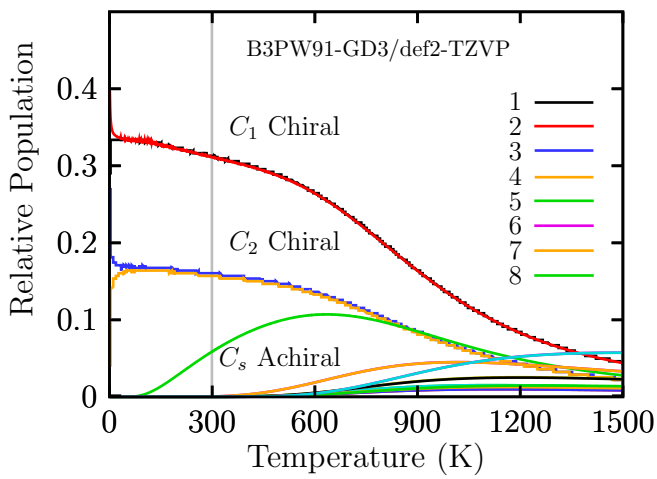

Figure 5.4: Probability of occurrence for all isomers at temperatures.

probability of occurrence for structures with C_1 and C_2 symmetries showed similar behaviors but different values; even so, the molecular properties are attributed to only one pair of enantiomers with symmetry C_1. The probability of occurrence for the achiral structure, which is shown in Figure 5.1c, located 1 kcal/mol above the putative global minimum, is depicted by a green solid line in Figure 5.4; it started to increase around a temperature of 120 K, and at room temperature, it is has a probability of 5%. At 700 K, the highest probability of occurrence was reached, corresponding to 12%; above this temperature, up to 1500 K, it started to decrease. Note that above 800 K and up to 1200 K, the achiral structure with C_s symmetry and the putative global minimum structures with C_2 symmetries coexisted. Interestingly, the Boltzmann ensemble was composed of an equal mixture of $\mathcal{M}$ and $\mathcal{P}$ enantiomers; thus, the chiral properties were null in all ranges of temperature, i.e., the Cu_{13} cluster did not exhibit properties such as vibrational/electronic circular dichroism. In ranging temperatures from 1200 to 1500 K, all isomers coexist with less than ten percent probability. To wit, all isomers are equally populated for hot temperatures or when the temperature increases to large values. The bulk melting temperature of copper, 1358 K [63]; So, we must consider that the anharmonic effects become strong at high temperatures [2]. From the thermal population, we consider the entropic-temperature term has a small effect on the Cu_{13} cluster distribution of isomers on the scale of temperature, as shown in Figure 5.4.

5.3.4 Enantiomerization Energy Barrier at Finite Temperature.

The process in which one enantiomer in a pair is converted into the other is known as enantiomerization; enantiomers each have an equal probability of occurrence, and the same energy. The enantiomerization energy or activation energy at temperature T defines the configurational stability. In some cases, a low enantiomerization energy is undesirable [318]. Two reaction mechanisms compete for the interconversion

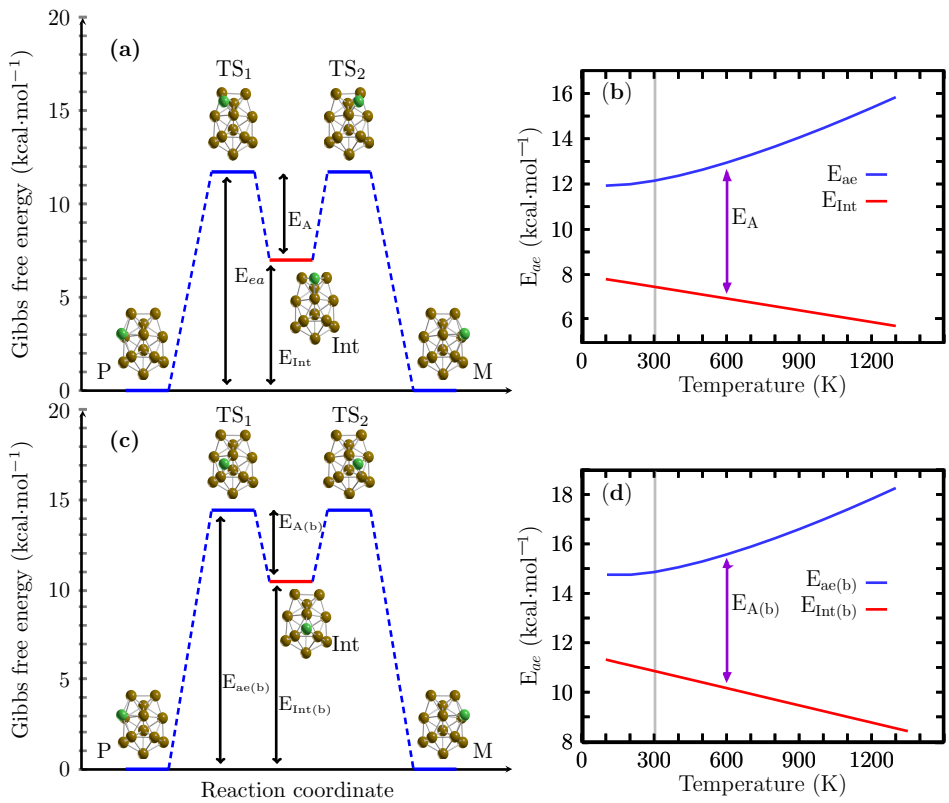

Figure 5.5: Figure shows the energy profile of a chemical reaction.

from $\mathcal{P}$ to $\mathcal{M}$ structures, and the shape of the energy barriers (or IRC) is similar to the inverted double-well potential [319] Figure 5.5a shows the reaction mechanism for the interconversion between $\mathcal{P}$ and $\mathcal{M}$ structures for route A, which proceeds via a two-step mechanism consisting of two symmetric steps with only one intermediate. Figure 5.5a shows the reaction mechanism for the interconversion between $\mathcal{P}$ and $\mathcal{M}$ structures for route B, which proceeds via a two-step mechanism consisting of two symmetric steps with only one intermediate. Figure 5.5a depicts the transition states TS1 and TS2, the intermediate (Int), and the putative lowest energy pair of enantiomers $\mathcal{P}$ and $\mathcal{M}$. The energy of enantiomerization was 12.15 kcal/mol, whereas the activation energy for the interconversion of the intermediate to $\mathcal{P}/\mathcal{M}$ structures was 5 kcal/mol at room temperature. The intermediate state was located at 7.13 kcal/mol above the putative chiral lowest energy structure The structures of the TS1 and TS2 states are depicted in Figure 5.5a. They appeared to be bilayer structures composed of a shared pentagonal bipyramid interspersed with a distorted hexagonal ring. The green atom represents the Cu atom that caps one edge of the pentagonal bipyramid and is responsible for the chirality of the Cu_{13} cluster. The intermediate state structure for the same bilayer presented 12 Cu atoms and the green Cu atom caps one of the faces in the pentagonal bipyramid. Figure 5.5a shows the enantiomerization energy E_{ae} depicted by a solid blue line. The relative energy of

the intermediate, E_{Int}, for the putative global chiral structures is depicted by a solid red line. As the temperature increased, the enantiomerization energy increased almost linearly. In contrast, the relative energy of the intermediate with respect to the putative global minimum decreased linearly, implying that the inverted double-wall became energetically greater. The activation energy for the interconversion between the intermediate and the $\mathcal{M}$ structure was 5 kcal/mol at room temperature; this increased linearly, from 4 kcal/mol at a temperature of 100 K to 9.5 kcal/mol at a temperature of 1200 K. As a consequence. In contrast, at low temperatures, the enantiomerization energy trend reached a minimum, whereas the relative energy of the intermediate increased; thus, the energy activation for the interconversion of the intermediate to the $\mathcal{P}/\mathcal{M}$ states tended to be smaller. These results suggest that at high temperatures, the enantiomerization barrier energy increased, and the intermediate state energy became more significant, stabilizing chirality and allowing the separation of enantiomers at room temperature. To elucidate the behavior of the interconversion from $\mathcal{P}$ and $\mathcal{M}$ structures; We computed the reaction rate constants based on Equation 5.1 (Eyring equation) that used the activation barrier ΔG between the putative global minimum $\mathcal{P}/\mathcal{M}$ structures and the transition state and did not take into account the tunneling effect. The Eyring equation relates the rate constant to temperature and the activation free energy.

$$k = k_0 \frac{K_B T}{h} e^{-\Delta G/RT} \tag{5.1}$$

Table 5.2: Table shows the values of enantiomerization energy (E_{ea}), relative energy of intermediate (E_{Int}), and activation energy (E_A).

	Reaction A			Reaction B		
Level of theory	E_{ea}	E_{Int}	E_A	E_{ea}	E_{Int}	E_A
B3PW91-D3/Def2TZVP	12.15	7.13	5.0	14.85	10.86	3.99
B3PW91/Def2TZVP	12.36	6.38	5.97	15.60	11.31	4.28

In Equation 5.1, k is the rate constant, k_0 transmission coefficient that in the absence of other kinetic data is set to 1, K_B is Boltzmann constant, T is the temperature, h is the Planck constant, R is ideal gas constant, and ΔG is the activation energy barrier. We consider the rate-determining step in the overall reaction is the rate of interconversion between $\mathcal{P}/\mathcal{M}$ and intermediary structures, and it is the slowest step; besides, its high activation energy characterizes it. (Notice, the activation energy barrier ΔG is computed with the statistical thermodynamics). The height of the activation energy barrier at room temperature for interconversion between $\mathcal{P}/\mathcal{M}$ and intermediary structures in route A is 12.14 kcal/mol, which leads to a rate constant of 7.84×103 1/s, whereas the activation energy barrier at 900 K is 14.0 kcal/mol, which leads to a rate constant of 7.47×109 1/s. This show that the rate constant increases at high temperatures, and it agrees with the thermal populations where the contribution of all isomers is less than 10% at high temper-

atures. We also have to consider that the melting point for copper is 1358 K, thus around this temperature, the glass state will dominate. Regarding dispersion, if it is not considered, the energy barriers tend to increase. For ease of comparison, Table 2 shows the values of the two similar reaction mechanisms A and B, taking into account the D3 dispersion of Grimme. Energetically, the reaction mechanism of route B is not so different from that of route A, as we can see in Figure 5.5c,d and in Table 5.2.

5.4 Conclusions

For the first time, to our knowledge and from our results, we computed the effect of symmetry on the Boltzmann populations on TM Cu clusters.

Chapter 6

The Cu_{38} cluster

6.1 Abstract

The UV-visible and IR properties of the Cu_{38} nanocluster depend to a great extent on the temperature. Density functional theory and nanothermodynamics can be combined to compute the geometrical optimization of isomers and their spectroscopic properties in an approximate manner. In this chapter 6, we investigate entropy-driven isomer distributions of Cu_{38} clusters and the effect of temperature on their UV-visible and IR spectra. An extensive, systematic global search is performed on the potential and free energy surfaces of Cu_{38} using a two-stage strategy to identify the lowest-energy structure and its low-energy neighbors. The effects of temperature on the UV and IR spectra are considered via Boltzmann probability. The computed UV-visible and IR spectrum of each isomer is multiplied by its corresponding Boltzmann weight at finite temperature. Then, they are summed together to produce a final temperature-dependent, Boltzmann-weighted UV-visible and IR spectrum. Additionally, Molecular Dynamics simulation of the Cu_{38} nanocluster was performed to gain insight into the system dynamics and make a three-dimensional movie of the system with atomistic resolution. Our results show the thermal populations at the absolute temperature of Cu_{38} cluster, and the disordered structure that dominates at high temperatures

6.2 Introduction

Nano clusters are of interest due they allow us to study the transition from free atoms to bulk condensed systems[320] as a consequence, analyze the size-dependent evolution of their properties.[321] Especially, Noble-Metal Nanoclusters (NMC) have attracted attention in many fields of science due to interesting plasmonic, catalytic properties,[322, 323] and photophysical properties at nanoscale,[324] Particularly, Nano Cu clusters embedded in the dielectric matrix have attracted attention because of their tunable longitudinal surface plasmon resonance.[322] Besides, copper is cheaper than gold and silver, and it has large photosensitivity, high thermal and electric conductivity, and optical properties [325] that makes it a good candidate to develop nanodevices [326] and nanoelectronics. [327] In particular, Cu_{38} attracted attention due to it has a magic structures, [328] defined in terms of geometric and energetic factors and related to the closing of electronic shells [329] as it happens

in small sodium clusters.[330] For the Cu_{38} cluster its magicity is due to only energetic considerations.[331, 329] In contrast, small packed barium clusters with magic numbers, the stability is dominated for geometrical effects rather than electronic effects.[330] It is believed that magic structures are the putative global minimum energy structures on the potential energy surface, thus reflect the molecular properties of the system.[329] From the experimental point of view, the Cu_{38} cluster has been widely studied by photoelectron spectroscopy techinque (PES). Pettiette *et al.*[332] employing PES extract the electronic gap of anionic Cu_{38} cluster and found a semiconductor type with 0.33 eV.[332, 325] However, the geometrical structure was not investigated. In contrast, Kostko *et al.* also studied the anionic Cu_{38} and from the PES inferred that putative global minimum should be an oblate structure instead of a high symmetric structure,[333, 325] despite that computations for 38 atom clusters on noble metal clusters frequently found high symmetric (cuboctahedral) structures.[331, 334, 333] From the theoretical point of view, Taylor *et al.* presented a study based on density functional theory (DFT) of thermodynamic properties of Cu_{38} cluster,[335] Prevoius works employing DFT studied the transition states and reaction energies of water gas shift reaction in a Cu_{38} cluster and Cu slab.[336] In other previously DFT studies the high symmetry octahedral structure was reported as the lowest energy structure[337] employing PW91[291] functional, plane wave basis set and pseudopotential approximation.[260] Hijazi *et al.* [338] investigated the Cu_{38} cluster employing hybrid strategy; they used the embedded atom method potential followed by DFT computations using the PBE functional and pseudopotential approximation and reported that octahedral (OH) symmetry is the putative global minimum structure followed by the incomplete-Mackay icosahedron (IMI) located at 0.26 eV above of the putative global minimum. On the other hand, search for the lowest energy structure employing many body potentials gives a cuboctahedral structure.[331, 339] Erkoc *et al.* [340] employing an empirical potential-energy function, which contains two-body atomic interactions [341] found that the fivefold symmetry appears as putative global minimum in Cu_{38} cluster. In contrast, the cuboctahedron structure was reported as putative global minimum in a previous studies[342] employing empirical *many-body Gupta* and *Sutton-Chen* potentials. Nevertheless, there has been some discussion which is the lowest energy structure, some previous works consider the Cu_{38} octahedron cluster, as the putative global minimum[338, 337, 260], in contrast, several others found that Cu_{38} cluster with the truncated octahedron geometry is energetically more stable than other configurations[343, 338, 260, 344, 345, 346]. We point out that the energy computed with different methods such as DFT, MP2, or CCSDT, just to mention few of them, yield different energetic ordering.[1, 347, 236] In the case of DFT, the functional and basis set employed, ZPE energy correction, or energy of dispersion among others can interchange the putative global minimum. Moreover, practical molecular systems and materials needs warm temperature [348], so the molecular properties at temperatures T are dominated by Boltzmann distributions of isomers,[1, 77, 2] therefore, their properties are statistical averages over the ensemble of conformations.[1] The structure corresponding to the global minimum ceases

to be the most likely at high T so other structures prevail. Furthermore, in small Ag clusters, the temperature leads the transition from the initial FCC phase to other structural modifications,[349] so it promotes the changes of fases in materials. Interesting, at different temperatures than zero, the molecular system minimizes the Gibbs free energy and maximizes the entropy.[1, 2] Although the search of the global and local minima is useful in understanding reactivities and catalytic efficiencies, but such studies most of the time neglect temperature dependent entropic contributions to free energy when increasing temperature. Taking temperature into account requires dealing with nanothermodyanamics.[1, 2, 52, 65, 64, 16, 63, 161] The thermodynamics of clusters have been studied by a variety of tools,[163, 1, 65, 64] like molecular-dynamics simulations on boron clusters [106] and Cu_{38} clusters.[325] The cluster properties depends strongly of the structure, size, composition, and temperature, so the first step in order to understanding molecular properties is the elucidation of the lowest energy structure and its isomers close in energy; [2, 1, 16, 157] This is a complicated task due to several factors.[1, 2] As second step for understanding cluster properties relies on their spectroscopy which gives insight into its structure and it was proposed as a way of detecting structural transformations into clusters. The influence of temperature on the spectroscopy has been computed before for a variety of clusters, for instance, [350, 1, 2] such in the present study, for the neutral Cu_{38} cluster, we use the statistical formulation of thermodynamics or nanothermodynamics[65, 1, 64, 2] to compute thermodynamics properties and define the putative global minimum at temperatures diferent from zero, evaluated the relative populations among the isomers and computed UV-Visible and IR spectra as a Boltzmann weighted spectrum sum of individual spectra. Our findings show that at hot temperatures at amorphous structure strongly dominate the putative global minimum whereas the truncated octahedron dominates at cold temperatures. The remainder of the manuscript is organized as follows: Section 2 gives the computational details and a brief overview of the theory and the algorithms used. The results and discussion are presented in section 3; The putative global at room temperature and relative population in ranging temperatures from 20 to 1500K, and the IR spectra as a function of temperature.

6.3 Results and Discussion

The ball and stick model shown in Figure 6.1 depicted the lowest-energy structure and the low-energy structures of neutral Cu_{38} clusters along with some competing isomers. At B3PW91/def2SVP level of theory and taking into account the dispersion pairwise correction of Grimme (DFT-GD3),[181] ZPE energy corrections and at room temperature and 1 atmospheric pressure. We found a tetrakaidecahedron as the lowest energy structure which has 14 faces: six equivalent square FCC(100) and eight equivalent hexagons, this shape is obtained when cutting the corners off 3D diamond shape, and it is a fcc-like truncated octahedron (TO). The calculated structure belongs to point group symmetry C_1, electronic ground state ^1A, its lowest IR

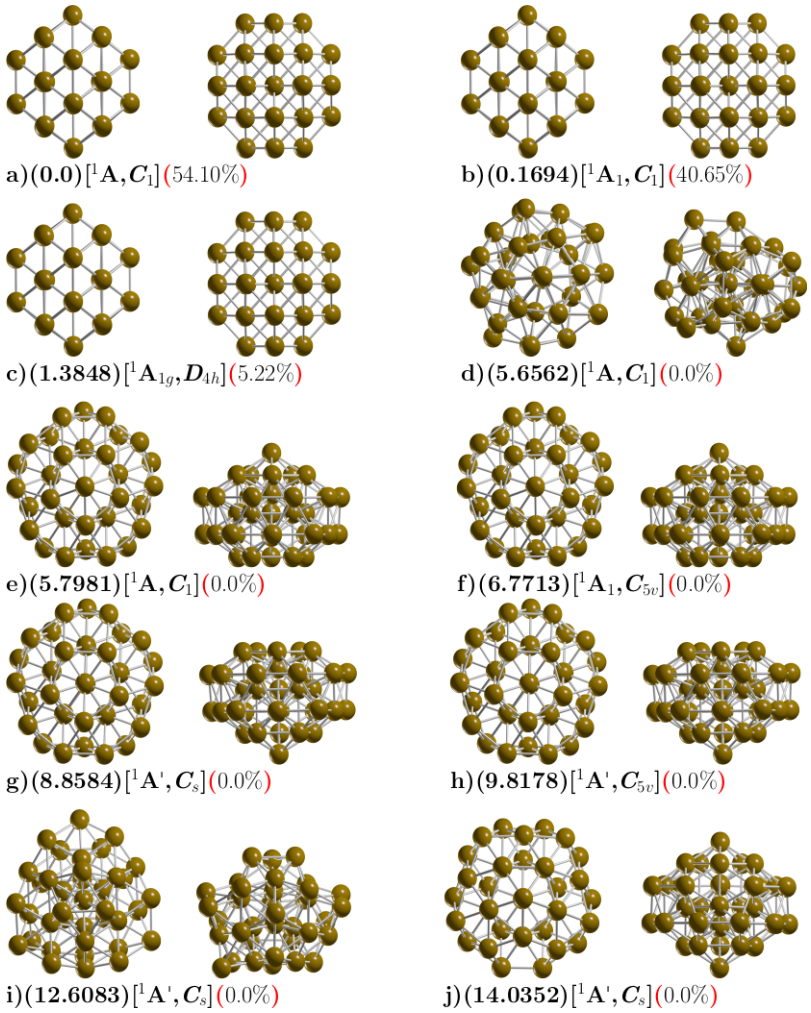

Figure 6.1: Optimized geometries in front and side views of neutral Cu_{38} cluster.

active vibration frequency is 32.57 cm^{-1} and is a semiconductor with electronic gap 0.623 eV. It is known that the bulk rare gas crystals have a face centered cubic (FCC) crystalline symmetry. Previous works on exploration of the potential energy surface of Cu_{38} cluster using genetic algorithms with Gupta potential often find highly symmetric TO structure,[333] other reported previous work employing *Sutton-Chen* potential with monte Carlo simulation also find TO structure.[273] The optimized Cu-Cu bond length is found to be 2.4670, Å which is in good agreement with other reported DFT calculations Cu-Cu dimmer[351, 308] of 2.248, Å and is consistent with the experimental bonding distance Cu-Cu 2.22Å. [351] Our computed diameter of TO structure is 7.8 Å and also is in good agreement of 8 Å reported in previous theoretical DFT calculations.[308] The second structure higher in energy lies at 0.16 kcal/mol at temperature of 298.15 K also is a TO structure with point group symmetry C_1, electronic ground state ^{1}A, the lowest IR active vibration frequency

is 32.13 cm^{-1}, and is a semiconductor with electronic gap 0.623 eV, similarly to that of the putative global minimum. The next structure is slightly higher in energy located at 1.38 kcal/mol also is a TO structure, but with D_{4h} point group symmetry and electronic ground state $^1A_{1g}$, and the lowest IR active vibration frequency is 33.44 cm^{-1}. We also explored TO structure, initializing the geometry from the high-symmetries OH and TH and after geometry optimization without constrains, the OH and TH symmetries become C_1 and D_{H4} symmetries. The perfect OH symmetry it could be deformed due to the *Jahn-Teller effect*[308, 351] and would have to be taken into account in the calculation of total energy[352, 353] and the relative population at temperature T could change as consequence in the optical properties. [354] Recently, in one of our previous works, we clarify the origin of Gibbs free energy differences between two similar structures just with different group symmetry, that is due to the rotational entropy, specifically the $R\,T\,ln(s)$ factor.[2] In this work, the energy difference of 0.16 between the two isomers depicted in Figure 6.1a with symmetry C_1 and RMSD, the difference is 0.08 and is due to the Jean teller effect. The structure located at 1.38 kcal/mol above the putative global minimum with D_{4H} symmetry is due to rotational entropy. The next structure, shown in Figure 6.1d is located at 5.65 kcal/mol above the putative global minimum, with point group symmetry C_1, and electronic ground state ^1A, the lowest IR active vibration frequency is 24.16 cm^{-1}, it is a distorted structure semiconductor with electronic gap of 1.0 eV, the calculated Cu-Cu bond distance is 2.50, Å and the molecular diameter of this structure is 9.1 kcal/mol, slightly larger Cu-Cu bond distance and diameter than the global minimum, this structure possesses the the smallest relative ZPE energy, as shown in Figure, as well as the smallest frequency of the vibrational modes of all isomers. The next two higher energy structures shows in Figure 6.1(e,f) are located up to 5.8 kcal/mol, an both of them are the incomplete-Mackay icosahedron (IMI) with C_1 and C_{5V} point group symmetries and electronic ground state ^1A and $^1A_1$ respectively. For both cases, the molecular diameter is 8.54, Å electronic gap of 0.97 eV eV and the Cu-Cu bonding distance is 2.47 Å. There are other higher energy structures shows in Figure 6.1(g,h,i,j), these do not contribute to any molecular property in all temperature range. In the Figure C.5, Appendix C.6, we depicted the lowest energy structures screening at B3PW91/def2SVP level of theory and without taking into account the atom-pairwise correction of Grimme GD3. The lowest energy structure is IMI structure with point group symmetry C_1 and electronic ground state ^1AH. The molecular diameter is 8.69 Å, slightly larger than those found at TO structure of 7.8, Å the average bond distance is 2.50 Å. At PBE-GD3/Def2SVP level of theory, we found a IMI structure to be the most stable structure whereas at the PBE-GD3/LANL2DZ level of theory we found the TO structure as the putative global minimum energy. The complete description of the structures located at higher energies is in the Supplementary Information. We point out here, for the Cu_{38} clusters, the order energetically of the isomers and the energy gap among isomers as well as the putative global minimum interchange when we take into account the dispersion interactions.

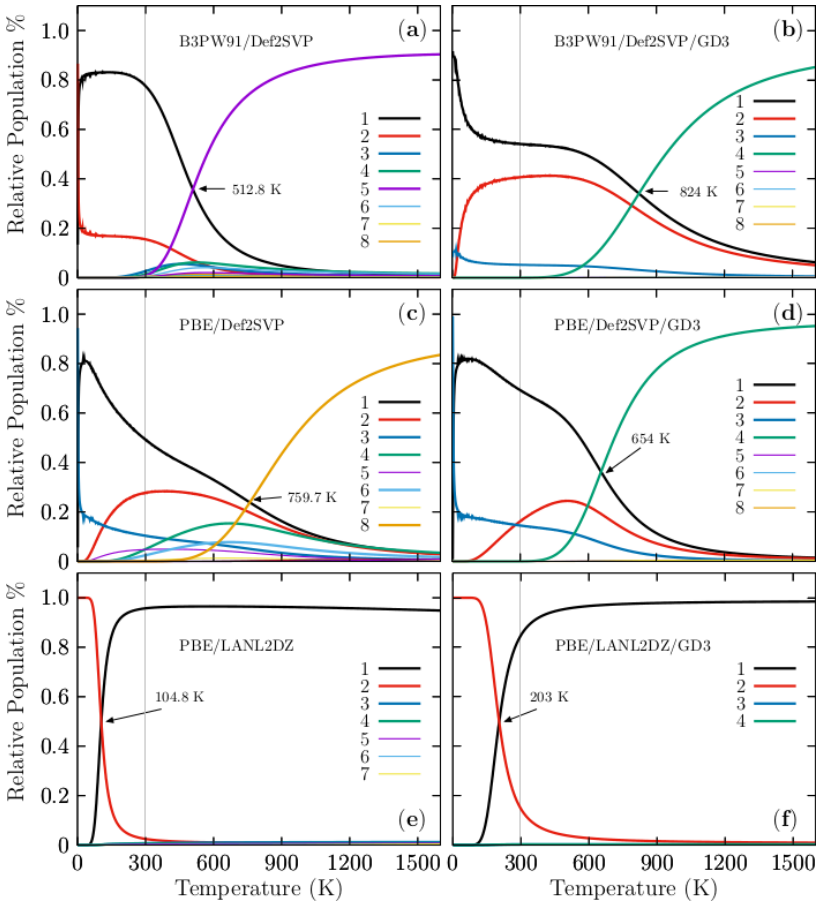

Figure 6.2: The thermal populations.

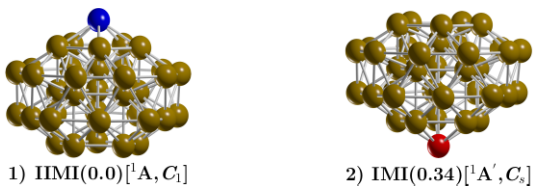

Figure 6.3: We depicted the inverted incomplete Mackay icosahedron, and the incomplete Mackay icosahedron.

6.3.1 Energetics

In the computation of energies employing different methods yield different results due to the functional and basis sets and therefore the energetic isomer ordering changes.[2, 236] The comparison of two different exchange-correlation functionals and two basis set and with and without taking into acount the dispersion D3 the Grimme are shown in the Table 6.1. The optimizations performed at the

Table 6.1: The energetic isomer ordering.

Level of theory	Energy	Isomers (energy kcal/mol)								
		i_a	i_b	i_c	i_d	i_e	i_f	i_g	i_h	i_i
B3PW91/Def2TZVP/GD3	ΔG	0.0	0.16	1.38	5.65	5.79	5.81	6.76	8.85	9.81
	$\mathcal{E}_0 + \mathcal{E}_{\text{ZPE}}$	0.0	0.09	0.0	5.01	5.01	5.01	5.01	5.01	8.17
	$\mathcal{E}_0$	0.05	0.0	0.10	8.76	4.89	4.89	4.88	4.88	4.88
B3PW91/Def2TZVP	ΔG	0.0	0.95	2.0	2.40	2.73	2.91	2.94	3.28	3.32
	$\mathcal{E}_0 + \mathcal{E}_{\text{ZPE}}$	0.0	0.0	2.14	3.29	6.52	3.84	2.14	3.27	3.84
	$\mathcal{E}_0$	0.0	0.0	2.09	3.27	6.13	3.76	2.09	3.28	3.76
PBE/Def2TZVP/GD3	ΔG	0.0	0.86	0.92	5.02	7.23	7.59	7.81	8.88	12.27
	$\mathcal{E}_0 + \mathcal{E}_{\text{ZPE}}$	0.0	0.89	0.0	8.70	7.94	7.92	8.61	7.94	14.24
	$\mathcal{E}_0$	0.0	0.90	0.0	9.14	7.92	7.93	8.84	7.94	12.47
PBE/Def2TZVP	ΔG	0.0	0.34	0.92	1.37	1.38	1.77	2.82	5.79	8.70
	$\mathcal{E}_0 + \mathcal{E}_{\text{ZPE}}$	0.0	0.0	0.37	0.41	1.77	1.77	1.77	9.08	15.75
	$\mathcal{E}_0$	0.0	0.0	0.38	0.39	1.73	1.73	1.74	9.47	9.86
PBE/LANL2DZ/GD3	ΔG	0.0	1.02	3.37	3.46	8.63	9.11	9.59	9.62	9.74
	$\mathcal{E}_0 + \mathcal{E}_{\text{ZPE}}$	2.03	0.0	2.12	2.14	8.31	8.77	8.73	9.34	8.71
	$\mathcal{E}_0$	1.97	0.0	2.01	2.01	8.08	8.60	8.52	9.12	8.45
PBE/LANL2DZ	ΔG	0.0	2.15	2.87	3.03	3.26	4.31	8.89	9.66	9.85
	$\mathcal{E}_0 + \mathcal{E}_{\text{ZPE}}$	0.97	0.0	1.46	1.38	1.64	1.68	7.98	9.19	9.58
	$\mathcal{E}_0$	0.86	0.0	1.27	1.11	1.48	1.42	8.03	8.99	9.37

B3PW91/PBE-def2TZVP considering the dispersion yield the same type of lowest energy equilibrium geometry and similar energetic isomer ordering when we employ the electronic energy with and without ZPE correction energy and Gibbs free energy computed at room temperature. From the energetic point of view, the inclusion of dispersion is more important than the type of functional and basis set, i.e The first line of the Table 6.1 show the relative Gibbs free energies computed at the B3PW91-D3/def2TZVP level of theory, the isomer label i_b in the Table 6.1 and depicted in Figure 6.1b is located 0.16 kcal/mol above the putative global minimum whereas the second line of the Table 6.1 show the relative Gibbs free energies computed at the B3PW91/def2TZVP level of theory and the isomer i_b in the Table 6.1 and depicted in Figure 6.1b is located 0.95 kcal/mol above the putative global minimum as it is shown in Table 6.1. For isomer i_b, the effect of the dispersion on the energy is decrease the relative Gibbs free energy with respect to the putative global minimum. (from 0.95 to 0.16 kcal/mol). The effect of dispersion, in the case of isomers i_c, is also decrease the relative Gibbs free energy with respect to the putative global minimum from 2.0 to 1.38 kcal/mol whereas for isomer label i_d, the relative Gibbs free energy increase from 2.4 to 5.65 kcal/mol. In summary, the effect of dispersion reduces the Gibbs free energy in the lowest energy structures where the Boltzamnn factors are difrentes from zero. A overall comparison of free energies computed with functional B3PW91, second line of the Table 6.1, and PBE in four line in the Table 6.1, versus free energies computed with functional PBE, four line

of the Table 6.1, and PBE in four line in the Table 6.1, shows a reduction in the relative Gibbs free energies when the PBE functional is employed. For the case of the basis set the LANL2DZ increase the relative Gibbs free energy in the low energy isomers as it is shows a comparison of line 6 of Table 6.1 versus line 1 of Table 6.1.

6.3.2 Relative stability

The probability of finding the TO structure with C_1 symmetry at B3PW91/def2-SVP level of theory is depicted in black-solid line in panel (a) of Figure 6.1(4). It strongly dominates from 0 to 300 K, thus all the molecular properties are due only to this structure. From slightly before 300 K, it start to decay exponentially and almost disappear at 900 K, at the same time, the probability of finding the amorphous structure with point group symmetry C_1, is depicted in violet-solid line in Figure 6.2(a), it start to grow exponentially and become dominate at temperature above 512.8 K and at 900 K it become strongly dominate. At solid-solid transition temperature of 512.8 K the TO and the amorphous structure co-exist. The effect of dispersion can be appreciated in panel (b) of Figure 6.2. The relative population is computed at B3PW91-G3/def2-SVP level of theory. The effect of the dispersion is dramatic, the solid-solid transformation point is shifted from 512.8 to 824 K, an increase of 160% and from the panel (b) one can see that the molecular properties below 600 K, are due to only the TO structure. Slightly before 600 K, The probability of finding the amorphous structure, depicted in green-solid line in panel (b), start to grow up exponentially and at temperature of 824 K the TO and amorphous structure co-exit. Whereas a temperature of 600 K the probability of find the TO structure start do decay exponentially and at 900 K its value still around 20%. The probabilities of occurrence at the PBE/def2-SVP level of theory of a particular Cu_{38} isomer are displayed in panel (c) of Figure 6.2. The dominant putative global minimum structure at T=0, is the inverted incomplete-Mackay icosahedron (IIMI) structure depicted in Figure 6.3a with C_1 symmetry and its probrobability of finding it is depicted as a black solid line in panel (c) of Figure 6.2. Its probability decays almost linearly until 1000 K where it almost disappears. At temperature of 759.7 K, the solid-solid transformation point, the IIMI structure co-exist with an amorphous structure. The probability of finding the amorphous structure start to grew up at 600 K, and above of solid-solid transformation point, it start to strongly dominate as putative global minimum. Where the probability of finding the IMI structure is depicted in red-solid line on panel (c) of Figure 6.2, the largest probability is 30% at room temperature. Interesting, the probabilities of IIMI and IMI structures does not cross at cold temperature. Zhang *et al.* [325] reported that IMI structure could be highly competitive at finite temperatures, but our findings shows that the amorphous structure with C_1 symmetry is highly dominant at hot temperatures, whereas the IIMI structure is highly dominant at cold temperatures.

For ease comparison, the Figure 6.3 display the IIMI and the IMI structures side by side. At cold and the IIMI structure dominate. The effects of dispersion is shift the solid-solid transformation point to lower temperatures from 759.7 K to

654 K as one can see in panel (d) Figure 6.2. The probability of finding the IIMI structure as a function of temperature is depicted in black solid-line and it decays approximately linearly from 50 to 500 K, after that it decays exponentially until 900 K where it disappears. At around 400 K, the probability of finding the amorphous structure, depicted in green solid-line in panel (d) of Figure 6.2, start to grow up in exponential way, and at temperature of 654 K it co-exit with the IIMI structure. Above 654 K, the amorphous structure becomes energetically favorable.

6.3.3 IR spectra at finite temperature

The properties observed in a molecule are statistical averages over the ensemble of geometrical conformations or isomers accessible to the cluster, so the molecular properties are governed by the Boltzmann distributions of isomers that can change significantly with the temperature primary due to entropic effects.[2, 1, 64] The major contributions to the entropy are the many soft vibrational modes that the clusters possesses. The IR spectrum is related to vibrations or rotations that alter the dipole moment, and it will happen in molecules that have a dipole moment. Also, the IR spectrum is related to the curvature of the potential curve versus interatomic distances. Complete information about molecular vibrations allows us to analyze catalytic chemical reactions.[355, 356] IR spectra are used to identify functional groups and chemical bond information. However, assigning IR bands to vibrational molecular modes in the measured spectra can be difficult and requires DFT calculations; as we mentioned earlier, the temperature is not considered in these computations and discrepancies between experimental and computed IR spectra can result from finite temperature, anharmonic effects, and multi-photon nature of experments, whereas IR computations assume single-photon processes.[1, 2] The IR spectra of isolated metal clusters in the gas phase for vanadium cluster cations as well as for neutral and cationic niobium clusters were measured.[357] Even though Cu clusters are important in catalysis and were the first clusters experimentally produced,[358] the available structural information is limited to study photoelectron spectroscopy for anions, mass spectrometry, and photodissociation spectra in the visible range.[359] Reciently, Lushchikova *et al.* [359] determine the structure of small cationic copper clusters based on a combination of IR spectroscopy of Cu_n^+-Ar_m complexes and DFT calculations. In this chapter 6, the IR spectra of isomers computations were carried out using the Gaussian package under harmonic approximation at level of theory PBPW91-D3[360]/def2TZVP and full width at half maximum (FWHM) of 8 cm^{-1} taking into account the dispersion of Grimme D3 as implemented in Gaussian code. Negative frequencies were checked in all calculations to ensure that there were not transitions states. The computed frequencies were scaled by 0.98 to estimate the observed frequencies. Here, the total IR spectrum is computed as a weighted Boltzmann sum of the single IR spectrum of each isomer of the distribution at finite temperature[2, 1, 268, 361] given by: IR=$\sum_{i=1}$ w$_i IR_i$, and the probabilities of occurrence displayed in Figure 6.2. To our knowledge, there are a few theoretical studies on IR spectra of noble metal clusters computed considering a weighted sum

of the IR spectra of isomers. [361] Computed weighted Boltzmann IR spectra of Cu_{38} clusters at different temperatures are shown in Figure C.3, Appendix C.4. Notice that the transition metal clusters are very stable, and its vibrational frequencies are found below 400 cm^{-1}[362] in good agreement with our computed spectra displayed in Figure C.3, Appendix C.4.

6.3.4 UV-Visible spectra at finite temperature

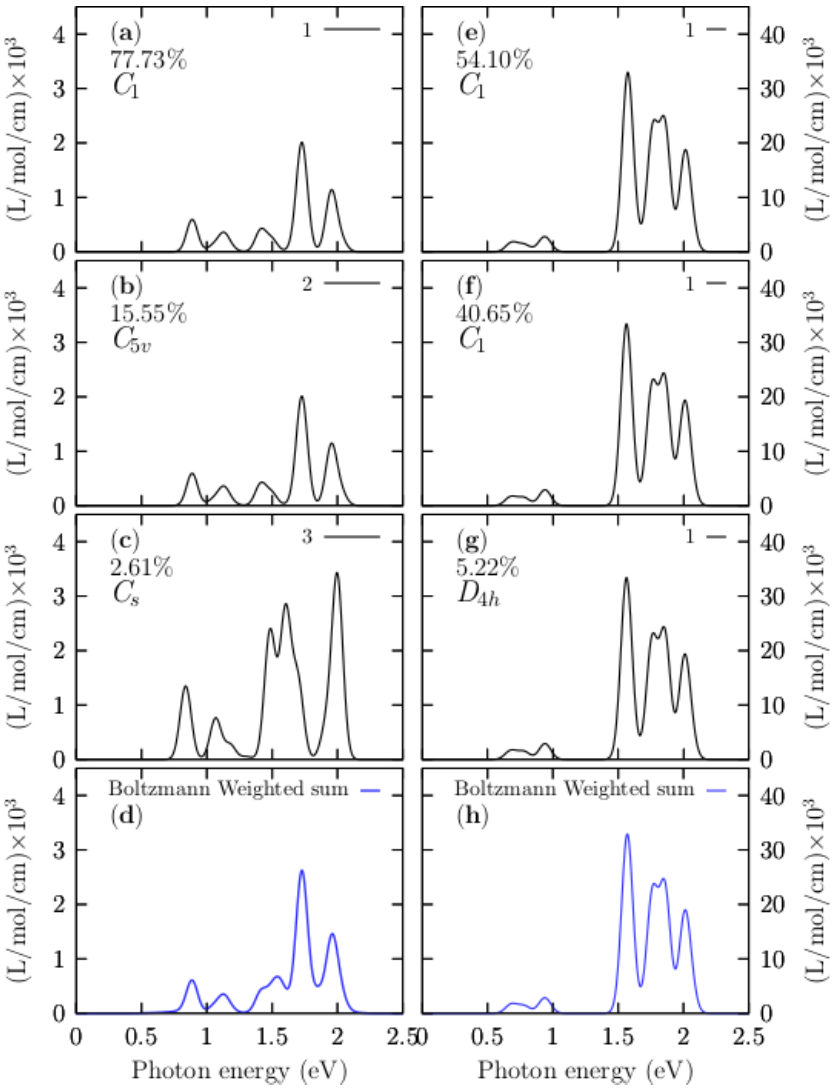

Figure 6.4: The UV-visible Boltzmann spectra weighted at room temperature of the neutral Cu_{38} cluster.

The optical properties are a source tomic structural information, and their electronic structure determines them.[363, 364] In this paper the TD-DFT was used

to compute the optical absorption spectra in the UV-visible range $0.5 < \hbar\omega < 2.5$ eV for the Cu_{38} cluster. We employ the CAM-B3LYP functional, Def2-TZVP basis set, and 50 singlets and 50 triplets states. The transition metals clusters allow us to study the influence of the **d** electrons on the optical properties; it is known that the **d** electrons strongly influence the surface plasmon response.[268] We show in Figure 6.4 the UV-spectra for the Cu_{38} cluster with and without the Grimme's dispersion D3. To take into account the effects of temperature on the UV-visible spectra. We consider that the UV-visible spectrum of a molecular ensemble is a weighted sum of all the individual contributions of each isomer that forms the ensemble. In panel labeled (e) is displayed the UV spectra considering the Grimme's dispersion GD3 and for the lowest energy structure with symmetry C_1; this structure contribute with 54% to the total Boltzamnn spectrum. In panel (f) is displayed the UV-visible for the low-energy structure located at 0.16 kcal/mol at room temperature and above the putative global minimum with C_1 symmetry, and this contributes to 40% to the Boltzmann spectrum. In panel (g) is displayed the UV-visible for the low-energy structure located at 1.38 kcal/mol at room temperature and above the putative global minimum with D_{4h} symmetry, and this contributes to 5.22% to the Boltzmann spectrum. In panel (h) is displayed the Boltzmann weighted UV-Visible spectrum at room temperature. Notice that all absorption spectra, (g) to (h), are similar; The Boltzmann weighted UV-Visible spectrum presented in Figure 6.4, panel (h) is composed of three peaks located between 1.5 to 2 eV and smaller intensity peaks located at 0.5 and 1.0 eV. The most significant absorption peak is located at 1.6 eV. Our computations show five absorption peaks of the UV-visible spectrum starting at 0.5 eV and finishing at 2.5 eV. Notice that the total optical spectrum is due only to the putative global minimum; despite the number of isomers growing exponentially, the main contribution to the optical properties comes from those low energy structures very close to the global minimum where weights Boltzmann factors temperature dependents are different from zero. Interestingly, the second low-energy structure located at 0.16 kcal/mol (room temperature) above the putative lowest energy structure screen or blocked the contributions to the Boltzmann optical spectrum of the other structures. In this paper, we called those structures as *shielding structures*. In Figure 6.4, panels (a) to (d) are displayed the optical absorption spectra in the UV-visible range computed with structures optimized without the Grimme's dispersion D3. Notice the effects of dispersion on UV-visible spectra is introduced by the change of the relative population when the optimizations are computed without, and with dispersion, e.g., the contribution, to the Boltzmann weighted UV-Visible spectrum, of the lowest energy structure computed without Grimme's dispersion D3 is 77% meanwhile, the contribution is 54% when an optimized structure is computed with Grimme's dispersion D3. The complete evolution of the Boltzmann weighted UV-Visible spectra for temperatures ranging from 10 to 1500 K is displayed in Figure C.4, Appendix C.5.

6.3.5 Molecular Dynamics

We performed Born-Oppenheimer molecular dynamics (MD) of the Cu_{38} cluster employing the deMon2K program[189] (deMon2k v. 6.01, Cinvestav, Mexico City, Mexico, 2011) at temperature of 600 K, aiming to gain insight into the dynamical behavior of the Cu_{38} cluster. The MD started from global putative minimun structure. The simulation time was 25 ps with a step size of 1 fs. All computations were performed under scheme of ADFT,[365] and for the basis set we employed the double zeta plus valence polarization (DZVP) all-electron basis. We employed the Nosé-Hoover thermostat to fix the temperature and the linear and angular momenta of the cluster Cu_{38} were initialized to zero and conserved.

6.4 Conclusions

For the first time, to our knowledge and from our results, we proposed the inverted incomplete-Mackay icosahedron (IIMI) with symmetry C_1 as low-energy structure[55] than the incomplete-Mackay icosahedron (IMI) with symmetry C_s and located 0.34 kcal/mol energy above the putative minimum global at 298.15 K. The yellow, the IIMI structure is the result of interchanging the red Cu atom depicted in the IMI structure to the position of blue atom in the IIMI structure. The IMI structure was reported in The HOMO-LUMO gap of the IMI structure is 0.24 eV (0.356 eV reported by previous DFT studies[325]) whereas for the HOMO-LUMO gap for IIMI structure is 0.30 eV, suggesting why the IIMI structure is energetically more stable.

Chapter 7

Conclusions

7.1 Conclusions

In this chapter, I list the main findings and the theoretical contribution made in this thesis to the nanoclusters and nanothermodynamics fields. I also propose new lines of investigation and perspectives.

1. Effects of temperature-symmetry in atomic nanoclusters
2. The effect of temperature on molecular properties
3. The development of the methodology based in nanothermodynamics and DFT to compute the molecular properties as a function of temperature.

The major conclusions of this doctoral thesis on different nanoclusters were as follows:

7.1.1 The $Be_6B_{11}^-$ cluster

We computed the relative population as a function of temperature using Boltzmann factors and the IR spectra dependent on temperature as a Boltzmann weighted sum of each IR spectrum's isomer. Here, we demonstrate that the temperature and entropic effects produce several competing structures, so a mixture of isomers co-exist at a specific temperature. Our computations showed (with relative population) that the low-symmetry isomers have a higher stability than isomers with high symmetry at high temperatures as a result of the entropic effect. The coaxial triple-layered structures with C_s symmetry are the putative global minima above 377 to 1500 K due to entropic effects. There are four T_{ss} points in the relative population of the $Be_6B_{11}^-$ cluster; the most important and dominant of these is the T_{ss} point located at 377 K with a relative population of 33%. Additionally, our results give insight into the long-range *van der Waals* interactions effects on the solid-solid transformation temperature points, hence the molecular properties. Indeed, the effect of dispersion shifts up in temperature the dominant T_{ss} point, keeping the relative population almost invariant. The other T_{ss} points shifted down on the temperature axis, so there is no clear trend in the up/downshifts in the $Be_6B_{11}^-$ cluster. Remarkably, the coaxial triple-layered structures with C_s and C_{2v} symmetries have the lowest B-B bond length, and the same geometrical structures have the lowest relative zero-point energy. This suggests that both trends shortening of the B-B bond length and lowest

relative zero-point energy are correlated with entropic effects. Analysis of our results leads to an interesting observation: The strong dominant putative global minimum, under high-temperature conditions, has the shortest B-B bond length and the lowest relative zero-point energy. The low vibrational modes significantly contribute to entropy, whereas high vibrational modes provide small contributions to entropy. The $Be_6B_{11}^-$ cluster has 45 vibrational modes. We found the range of frequencies-the lowest to the highest vibrational modes that contribute to zero-point energy by computing the zero-point energy as a function of vibrational modes. We needed to sum the first 38 modes that contribute to zero-point energies; the frequency range was between 46 and 1026 cm^1. Vibrational modes outside of this range do not contribute to the zero-point energy. At the energy single-point CCSD(T) level of theory, the energetic ordering of isomers changes with respect to employing the electronic or Gibb's free energies. The inclusion of the zero-point energy in CCSD(T) energies illustrates that the energy difference among isomers reduces drastically, which suggests that the dominant putative global minimum at zero temperature when we employ the CCSD(T) energies will change with the inclusion of temperature. The properties observed in a molecule are statistical averages over the ensemble of geometrical conformations or isomers accessible to the cluster, so the molecular properties are ruled by the Boltzmann distributions of isomers, which can change significantly with temperature, primarily due to entropic effects. We computed the IR spectra dependent on temperature as a Boltzmann weighted sum of each IR spectrum's isomer. Our computations showed that the competing structures provide a different percentage to the entire molecular properties and IR spectra, in detail, the molecular properties can not be attributed to only the lowest energy structure. The structures located at high energy above the putative global minimum that have a significant energy difference among isomers on the potential/free energy surface do not contribute to the entire IR spectrum. Despite the number of isomers growing exponentially, the main contribution to the molecular properties comes from the low-energy structures close to the global minimum where the weighted Boltzmann factors temperature dependence are different from zero. (This depends strongly on the energy separation; if the energy separation is significant, the IR spectrum does not change.) The spectra that belong to the low-energy structure dominate the IR spectrum of the $Be_6B_{11}^-$ cluster at low-temperature structures, whereas at high temperatures, it is strongly dominated by the spectra of structures located at high energy above the putative lowest energy structures. The increase/decrease in a peak/band in the IR spectra as a function of temperature is a clear signature of an interchange of the dominant lowest energy structure. With the IR spectra, we illustrated that the main contributions to the molecular properties are from the low-energy structures that are very close to the global minimum where the weighted Boltzmann factors temperature dependence is different from zero. The present thesis highlights the importance of entropy-temperature effects and what happens when some low-energy structures are not considered. We show that symmetry plays an important role in the definition of the global minimum and hence in molecular properties. We demonstrate that dispersion effects has a little the changes of the T_{SS} points in temperature scale.

All of these effects have an impact on the spectroscopic and any other property of a molecular system. The Boltzmann-IR-spectra as a function of temperature were presented. The spectra unravel that the peak located at 1500 cm^{-1}, shows in Figure 8, panels (a-d), is present only in temperatures higher than 300 K, where the coaxial-triple layered structures start to be the lowest energy structures. The above mentioned reasons indicate that the vibrational modes located in the range of 1036 to 1518 cm^{-1} are responsible for the cluster's fluxionality. An immediate future project is the computation of the optical spectra and other molecular properties employing the methodology described in this chapter and the computation of the relative population in many atomic and molecular clusters of interest employing higher levels of theory.

7.1.2 The Be_4B_8 cluster

We initially sampling the potential energy surface with 2400 candidates of neutral Be_4B_8 structures, and with an efficient cascade type algorithm coupled to DFT; We were able to locate twenty-two final isomers within an energy range of 9.2 kcal/mol, six of which are chiral low energy structures with symmetries C_1, C_2, and D_2 respectively, as far as we know not yet reported as chiral structures. They are constituted by a sandwich structure type in which the boron atoms from a distorted ellipsoid ring with each Be-Be dimers are capping each side of the sandwich. Our findings show that the chirality that exhibits the Be_4B_8 cluster emerges from the Be-Be dimers' mirror position. Additionally, based on the AdNDP analysis and the computed transition state and IRC between $\mathcal{P}$ and $\mathcal{M}$ enantiomers, we can deduce that the Be-Be and Be-B interaction favors the Be_4B_8 to be chiral and energetic minimum structure. According to our calculations, the enantiomerization energies barriers of the transformation $\mathcal{P}$ to $\mathcal{M}$ and $\mathcal{M}$ to $\mathcal{P}$ is equal to each other, moreover the activation energy between $\mathcal{P}$ to an achiral structure and $\mathcal{M}$ to an achiral structure are equal, thus the Boltzmann ensemble is composed of an equal mixture of $\mathcal{M}$ and $\mathcal{P}$ enantiomers. The enantiomerization energy between the chiral putative global minima in the ranging of temperatures from 20 to 1900 K is mainly composed of enthalpic than entropic term. The entropy-temperature term reduces the interconversion energy barrier like maximum in 28%; thus, the barrier is not influenced significantly by the entropic term. On the other hand, our results show that the energy barrier is 6.20 kcal/mol at room temperature between the lowest energy enantiomer ($\mathcal{P}/\mathcal{M}$ and the first achiral structure located at 1.79 kcal/mol at 298.15 K. The barrier does no increase significantly neither at cold temperatures nor at hot temperatures, the barrier high at 20 K is 6.43 kcal/mol. In contrast, it is 7.32 kcal/mol at 1900 K. Remarkably, the interconversion between enantiomers and achiral structure is more favored than the interconversion between a pair of enantiomers in all ranges of temperature. Furthermore, our results show that in the temperature range from 20 to 738 K, the interconversion between an enantiomer ($\mathcal{P}/\mathcal{M}$ and the achiral structure is an endothermic type reaction. At the transformation solid-solid point located at 739 K, the enthalpy of reaction is zero, and the energy barrier is

a minimum. In this point coexist the $\mathcal{P}$ and $\mathcal{M}$ structures with an achiral structure. At 739 K, above the interconversion between enantiomers-achiral structures are exothermic, which implies the heat of reaction. Notice that the change from endo to exothermic reaction is driven by entropic-temperature term. In this st udy and for the first time, we defined two novel points on a scale of temperature. a) The first one is the T_{ee} where the change in the reaction type occurs, and b) the second is the T_{bb} where the activation energy of two different reaction mechanisms are equal to each other, so the reaction rate equals. The energetic ordering of the isomers when we employing the Gibbs free energy computed at 298.15 Kagree with the energy ordering employing the single point CCSD(T) energies computed with DLPNO-CCSD(T), and the energy ordering change just with the interchange of the two achiral structures located at 3.61 kcal/mol and 3.38 kcal/mol above the putative global minimum. Furthermore, Our results on $\mathcal{T}_1$ diagnostic confirm that energies computed at the DFT level of theory do not contain a large multireference character, so the Be_4B_8 cluster is well characterized. Regarding relative population, our findings show that the putative global minimum that clearly and strongly dominates at cold temperatures is the pair of enantiomers. At 739 K, above, an achiral structure dominates as a putative global minimum with less than 20%. We also show that the relative population or Boltzmann distribution could depend on the functional and the basis set employed. The energy separation among isomers affects the relative population strongly. The Boltzmann distribution is composed of six isomers at 298.15 K with only different symmetries, and its contribution is approximately 98% thus, at room temperature, the molecular properties are strongly dominated by the pair of enantiomers putative global minimum. We analyzed the effects of the point group symmetry on Gibbs free energy as a function of temperature. The small Gibbs free relative energy differences of 0.41 and 0.81 kcal/mol between different symmetries at 298.15 K are due to rotational entropy that in fact, it is a function of number of symmetry, and it become larger at the temperature increase. This strongly suggests that we need to explore the free energy surface taking into account clusters with low symmetries. The low symmetries trends to dominate as putative global minimum as the temperature increases. For total VCD/IR spectra as a function of temperature, we compute the Boltzmann weighted superposition of each isomer's VCD/IR spectrum that yields a total VCD/IR spectrum. Boltzmann VCD weighted spectra for this particular chiral cluster is null in all range of temperature because in the ensemble P and M enantiomers are present in equal mixture. However, a clear temperature dependence of the Boltzmann IR weighted spectra is driven just by the probability of the putative low-energy isomers in the temperature ranging from 20 to 739 K. At temperature above 739 K, the IR spectra decay strongly, whereas, at a temperature above 1200 K, the IR spectra are almost null. In summary, IR spectra at room temperature are dominated by pair of enantiomers putative global minima, whereas at hot temperatures, the IR spectra are almost null. Our molecular dynamics corroborate that the melting point is located in the temperature ranging from 1400 to 1500 K, because and in accorde with molecular dynamics, the dissociation phenomenon occurs at 1500 K, and the melting point is

located below this point. As future work, the inclusion of anharmonic effects should be taken into account also the relative population at CCSDT(T) level of theory is going to be calculated. The melting point also should be computed. At finite temperature the entropy is maximized, taking into account this, a future project is a implementation of an algorithm to search on the free energy surface employing the entropy as an objective function instead of energy. Finally, we point out that in any reaction, the activation energy at finite temperature must be computed considering the reactants and products with non-symmetry (C_1), by reason of the small energy differences dependent on symmetry and temperature (i.e 0.41 kcal/mol for C_2 at 298.15 K) increase the energy barrier between the reactants and products, hence the velocity of the reaction could be miscalculated. The Boltzmann Optics Full Adder (BOFA) *Python* code supporting the findings of this study is available from the corresponding author upon reasonable request.

7.1.3 The Cu_{13} cluster

Our computed $\mathcal{T}_1$ diagnostic 0.023, determine that the computed DFT energies are not properly described by a single reference method or contain a multireference character. So, further studies needed to be done. We explored the potential and free energy surface of the neutral Cu_{13} cluster with an efficient cascade-type algorithm coupled to DFT. We found that the putative global minimum was a pair of enantiomers that strongly dominated at room temperature. Our findings show that the chirality exhibited by the Cu_{13} cluster emerged from the Cu atom capping a face of the core Cu_{12} cluster. We showed that for the interconversion between $\mathcal{P}$ and $\mathcal{M}$ structures, two similar reaction mechanisms were possible. Both of them closed in their energy barriers and proceeded via two symmetric steps. The energy of enantiomerization and the energy barrier between the intermediate and the $\mathcal{P}/\mathcal{M}$ structures increased as the temperature increased. We computed the reaction rate constants based on the Eyring equation; our findings show that at high temperatures, enantiomerization is favored. The entropic-temperature term did not significantly influence the energy barriers; thus, they are mainly composed of enthalpic energy. Regarding Grimme's dispersion D3, this lowers the energy barriers, i.g., in route B, the EA decreased by 7% (from 4.3 to 4.0 kcal/mol). We showed that the pair of enantiomers with C_1 symmetries strongly dominated at room temperature revealed by the thermal population. Hence, at body temperature, all the molecular properties were attributable to those structures. For each DFT functional (B3PW91, TPSS, PBE, and BP86) used in this study, the thermal population and energetic ordering of the isomers are preserved, although differences in the energy between the isomers occur; the main contributors to any molecular property of Cu_{13} are always the chiral isomers. The bonding in the lowest energy chiral Cu_{13} cluster is due to the 4s shell electrons for which the bonding pattern, as revealed by Ad-NDP, consisted of 6 sets of 13c-2e completely delocalized bonds, plus a 9c-1e bond corresponding to the unpaired electron. Future work will focus on the computation of UV absorption of the Cu clusters employing Boltzmann weighted spectra,

comparing it with a single UV spectrum of the putative global minimum.

7.1.4 The Cu_{38} cluster

We computed the effect of symmetry on the Boltzmann populations on Cu_{38} clusters. In spite that the number of isomers grows exponentially, the main contribution to the optical properties comes from those low energy structures very close to the global minimum where weights Boltzmann factors temperature dependents are different from zero. We performed an unbiased global search for minimum energy Cu_{38} clusters structures using a two-stage strategy. First a global search using a semi empirical methodology, followed by a density functional theory optimization of the best structures from the first stage was done at different levels of theory. The temperature and entropic effects cause several competing structures because energy separation between isomers on the free energy surface is small and changes the dominant structure, so probably a mixture of isomers interconverted at temperature finite. Those energetically competing structures provide a different percentage of the entire IR spectrum. On the other hand, those higher energy structures with significant energy separation among isomers on the potential energy surface do not contribute to the entire IR spectrum. Despite that, the number of isomers grows exponentially. The main contribution to the molecular properties comes from those low-energy structures very close to the global minimum, where weight's Boltzmann factors temperature dependents are different from zero. (depends strongly on the energy separation, if the energy separation is significant, the IR spectrum going to be rigid, not changes) A motif is dominant in cold conditions, whereas the other motif is dominant in other hot conditions; additionally, the level of theory is decisive in the computations of TSS point dependent-temperature Our computations clearly show (relative population) that the low-symmetry isomers become more stable at high temperatures due to the entropic effect and the fact that energy states of molecules follow Boltzmann distribution in all six different levels of theory. Our unbiased global search on the free energy surface show that there is an amorphous structure that strongly dominate at hot temperatures, as far as we know this is a novel putative global minimum at hot temperatures. As immediate work is the computations of the relative populations at high level of theory and compute the $\mathcal{T}_1$ diagnostic to determine that the computed DFT energies are not properly described by a single reference method or contain a multireference character. So, further studies needed to be done.

7.2 Perspectives and future work

The cluster propierties depends strongly on the structure, size, composition and temperature and with the aim to compute molecular properties is necessary to consider statistical thermodynamics; the first step in order to understand the molecular properties is the elucidation of the lowest energy structure and its isomers. I underline that the temperature is a key in the chemical reactions, so to compare the-

oretical computations and experiments, the temperature must be considered. The experiment studies are carring out in non-zero temperatures and its necessary to understand what are the effect of the temperature. Future work should be adressed in these points:

- Computations at a high level of theory, like CCSD(T) level.
- Corrections at high temperatures.
- Computations on nitrogenous bases and nucleic acids like DNA and RNA.

Bibliography

[1] Carlos Emiliano Buelna-García, José Luis Cabellos, Jesus Manuel Quiroz-Castillo, Gerardo Martinez-Guajardo, Cesar Castillo-Quevedo, Aned de Leon-Flores, Gilberto Anzueto-Sanchez, and Martha Fabiola Martin-del Campo-Solis. Exploration of free energy surface and thermal effects on relative population and infrared spectrum of the $Be_6B_{11}^-$ fluxional cluster. *Materials*, 14(1), 2021. (Cited on pages 2, 8, 9, 10, 11, 15, 16, 21, 43, 44, 45, 46, 49, 58, 60, 61, 62, 65, 66, 74, 75 and 81.)

[2] Carlos Emiliano Buelna-García, Eduardo Robles-Chaparro, Tristan Parra-Arellano, Jesus Manuel Quiroz-Castillo, Teresa del Castillo-Castro, Gerardo Martínez-Guajardo, Cesar Castillo-Quevedo, Aned de León-Flores, Gilberto Anzueto-Sánchez, Martha Fabiola Martin-del Campo-Solis, Ana Maria Mendoza-Wilson, Alejandro Vásquez-Espinal, and Jose Luis Cabellos. Theoretical prediction of structures, vibrational circular dichroism, and infrared spectra of chiral Be_4B_8 cluster at different temperatures. *Molecules*, 26(13), 2021. (Cited on pages 2, 9, 10, 11, 13, 15, 16, 21, 45, 49, 58, 60, 61, 62, 63, 66, 67, 68, 74, 75, 77, 78 and 81.)

[3] Jin-Chang Guo, Lin-Yan Feng, Ying-Jin Wang, Said Jalife, Alejandro Vásquez-Espinal, José Luis Cabellos, Sudip Pan, Gabriel Merino, and Hua-Jin Zhai. Coaxial triple-layered versus helical $Be_6B_{11}^-$ clusters: Dual structural fluxionality and multifold aromaticity. *Angewandte Chemie International Edition*, 56(34):10174–10177, 2017. (Cited on pages 2, 8, 22, 25, 26, 28, 32, 39, 43, 44, 49 and 62.)

[4] John L. Margrave. Chemistry at high temperatures. *Science*, 135(3501):345–350, 1962. (Cited on page 4.)

[5] A. D. Kirshenbaum and A. V. Grosse. The combustion of carbon subnitride, C_4N_2, and a chemical method for the production of continuous temperatures in the range of 5000-6000°k. *Journal of the American Chemical Society*, 78(9):2020–2020, 1956. (Cited on page 4.)

[6] A. D. Becke. Density-functional exchange-energy approximation with correct asymptotic behavior. *Phys. Rev. A*, 38:3098–3100, Sep 1988. (Cited on pages 7, 61 and 65.)

[7] John P. Perdew, Kieron Burke, and Matthias Ernzerhof. Generalized gradient approximation made simple. *Phys. Rev. Lett.*, 77(18):3865–3868, October 1996. (Cited on pages 7 and 65.)

[8] Zhongqi Ma. Quantum three-body problems. *Science in China Series A: Mathematics*, 43(10):1093–1107, Oct 2000. (Cited on page 7.)

[9] L. I. Schiff. Book Review: Quantum mechanics, Second edition. McGraw Hill Book Co, New York, Toronto, London. 1955. xii-417 pages. *McGraw Hill*, 1:133–133, 1956. (Cited on page 7.)

[10] L. H. Thomas. The calculation of atomic fields. *Mathematical Proceedings of the Cambridge Philosophical Society*, 23(5):542–548, 1927. (Cited on page 7.)

[11] Elliott H Lieb and Barry Simon. The thomas-fermi theory of atoms, molecules and solids. *Advances in Mathematics*, 23(1):22 – 116, 1977. (Cited on page 7.)

[12] P. Hohenberg and W. Kohn. Inhomogeneous electron gas. *Phys. Rev.*, 136:B864–B871, Nov 1964. (Cited on page 7.)

[13] Tun Lu, Libo Wang, Ye Jiang, Qiuwen liu, and Caijin Huang. Hexagonal boron nitride nanoplates as emerging biological nanovectors and their potential applications in biomedicine. *J. Mater. Chem. B*, 4:6103–6110, 2016. (Cited on page 8.)

[14] M. J. Frisch, G. W. Trucks, H. B. Schlegel, and G. E. Scuseria et al. Gaussian 09. *Gaussian Inc. Wallingford CT 2009*, jan 2009. (Cited on pages 8 and 61.)

[15] Min Ji, Xiao Gu, Xi Li, Xingao Gong, Jun Li, and Lai-Sheng Wang. Experimental and theoretical investigation of the electronic and geometrical structures of the au32 cluster. *Angewandte Chemie International Edition*, 44(43):7119–7123, 2005. (Cited on pages 8 and 28.)

[16] Francesca Baletto and Riccardo Ferrando. Structural properties of nanoclusters energetic, thermodynamic, and kinetic effects. *Rev. Mod. Phys.*, 77:371–423, May 2005. (Cited on pages 8, 22, 23, 43, 45, 58, 60 and 75.)

[17] L T Wille and J Vennik. Computational complexity of the ground-state determination of atomic clusters. *Journal of Physics A: Mathematical and General*, 18(8):L419–L422, June 1985. (Cited on page 8.)

[18] Shao-Gang Xu, Yu-Jun Zhao, Ji-Hai Liao, and Xiao-Bao Yang. Understanding the stable boron clusters: A bond model and first-principles calculations based on high-throughput screening. *The Journal of Chemical Physics*, 142(21):214307, 2015. (Cited on page 8.)

[19] G Rossi and R Ferrando. Searching for low-energy structures of nanoparticles: a comparison of different methods and algorithms. *Journal of Physics: Condensed Matter*, 21(8):084208, jan 2009. (Cited on page 8.)

[20] Longjiu Cheng, Yan Feng, Jie Yang, and Jinlong Yang. Funnel hopping: Searching the cluster potential energy surface over the funnels. *The Journal of Chemical Physics*, 130(21):214112, 2009. (Cited on page 8.)

[21] Zhen Hua Li, Ahren W. Jasper, and Donald G. Truhlar. Structures, rugged energetic landscapes, and nanothermodynamics of aln (2, <n< 65) particles. *Journal of the American Chemical Society*, 129(48):14899–14910, 2007. PMID: 17994736. (Cited on pages 8, 23 and 28.)

[22] S. Kirkpatrick, C. D. Gelatt, and M. P. Vecchi. Optimization by simulated annealing. *Science*, 220(4598):671–680, 1983. (Cited on page 8.)

[23] Nicholas Metropolis, Arianna W. Rosenbluth, Marshall N. Rosenbluth, Augusta H. Teller, and Edward Teller. Equation of state calculations by fast computing machines. *J. Chem. Phys.*, 21(6):1087–1092, 1953. (Cited on page 8.)

[24] Y. Xiang and X. G. Gong. Efficiency of generalized simulated annealing. *Phys. Rev. E*, 62:4473–4476, Sep 2000. (Cited on page 8.)

[25] Yang Xiang, Sylvain Gubian, Brian Suomela, and Julia Hoeng. Generalized simulated annealing for global optimization: the GenSA package for R. *The R Journal*, 5(1):13–29, June 2013. (Cited on page 8.)

[26] D.G. Vlachos, L.D. Schmidt, and R. Aris. Comparison of small metal clusters: Ni, Pd, Pt, Cu, Ag, Au. *Z. Phys. D Atom Mol. Cl.*, 26(1):156–158, 1993. (Cited on page 8.)

[27] V. Granville, M. Krivanek, and J.-P. Rasson. Simulated annealing: a proof of convergence. *IEEE Trans. Pattern Anal. Mach. Intell.*, 16(6):652–656, 1994. (Cited on page 8.)

[28] Xue Dong, Said Jalife, Alejandro Vásquez-Espinal, Estefanía Ravell, Sudip Pan, José Luis Cabellos, Wei-yan Liang, Zhong-hua Cui, and Gabriel Merino. Li_2B_{12} and Li_3B_{12}: prediction of the smallest tubular and cage-like boron structures. *Angewandte Chemie International Edition*, 57(17):4627–4631, 2018. (Cited on pages 8, 21, 43 and 62.)

[29] Xue Dong, Said Jalife, Alejandro Vásquez-Espinal, Jorge Barroso, Mesías Orozco-Ic, Estefanía Ravell, José Luis Cabellos, Wei-yan Liang, Zhong-hua Cui, and Gabriel Merino. Li_2B_{24}: the simplest combination for a three-ring boron tube. *Nanoscale*, 11:2143–2147, 2019. (Cited on pages 8 and 62.)

[30] Anastassia N. Alexandrova, Alexander I. Boldyrev, You-Jun Fu, Xin Yang, Xue-Bin Wang, and Lai-Sheng Wang. Structure of the na_xcl_x (x=1,4) clusters via ab-initio genetic algorithm and photoelectron spectroscopy. *J. Chem. Phys.*, 121(12):5709–5719, 2004. (Cited on pages 8 and 62.)

[31] Martin Saunders. Stochastic search for isomers on a quantum mechanical surface. *Journal of Computational Chemistry*, 25(5):621–626, 2004. (Cited on page 8.)

[32] Martin Saunders. Stochastic exploration of molecular mechanics energy surfaces. hunting for the global minimum. *Journal of the American Chemical Society*, 109(10):3150–3152, 1987. (Cited on page 8.)

[33] P. J. Hsu and S. K. Lai. Structures of bimetallic clusters. *J. Chem. Phys.*, 124(4):044711–0, 2006. (Cited on page 8.)

[34] Wei Qin, Wen-Cai Lu, Li-Zhen Zhao, Qing-Jun Zang, C Z Wang, and K M Ho. Stabilities and fragmentation energies of si n clusters (n = 2-33). *J. Phys.: Condens. Matter*, 21(45):455501, 2009. (Cited on page 8.)

[35] David E. Goldberg. *Genetic Algorithms in Search, Optimization and Machine Learning*. Addison-Wesley Longman Publishing Co., Inc., Boston, MA, USA, 1st edition, 1989. (Cited on page 8.)

[36] Anastassia N. Alexandrova and Alexander I. Boldyrev. Search for the $li_n^{0,+1,-1}$ (n = 5-7) lowest-energy structures using the ab initio gradient embedded genetic algorithm (gega). elucidation of the chemical bonding in the lithium clusters. *J. Chem. Theory Comput.*, 1(4):566–580, 2005. (Cited on page 8.)

[37] Anastassia N. Alexandrova. H·(h2o)n clusters: Microsolvation of the hydrogen atom via molecular ab initio gradient embedded genetic algorithm (gega). *J. Phys. Chem. A*, 114(48):12591–12599, 2010. (Cited on page 8.)

[38] D. Harding, S. R. Mackenzie, and T. R. Walsh. Structural isomers and reactivity for rh6 and rh6+. *J. Phys. Chem. B*, 110(37):18272–18277, 2006. (Cited on page 8.)

[39] David J. Wales and Jonathan P. K. Doye. Global optimization by basin hopping and the lowest energy structures of Lennard-Jones clusters containing up to 110 atoms. *J. Phys. Chem. A*, 101(28):5111–5116, 1997. (Cited on page 8.)

[40] Sukanta Mondal, Jose Luis Cabellos, Sudip Pan, Edison Osorio, Juan Jose Torres-Vega, William Tiznado, Albeiro Restrepo, and Gabriel Merino. 10-π-electron arenes a la carte: structure and bonding of the [e-($c_n h_n$)-e]n-6 (e = ca, sr, ba; n = 6-8) complexes. *Phys. Chem. Chem. Phys.*, 18:11909–11918, 2016. (Cited on page 8.)

[41] Estefanía Ravell, Said Jalife, Jorge Barroso, Mesias Orozco-Ic, Gerardo Hernandez-Juarez, Filiberto Ortiz-Chi, Sudip Pan, Jose Luis Cabellos, and Gabriel Merino. Structure and bonding in CE_5^- (e=al-tl) clusters: Planar tetracoordinate carbon versus pentacoordinate carbon. *Chemistry - An Asian Journal*, 13(11):1467–1473, 2018. (Cited on pages 8 and 62.)

[42] Rafael Grande-Aztatzi, Paulina R. Martínez-Alanis, José Luis Cabellos, Edison Osorio, Ana Martínez, and Gabriel Merino. Structural evolution of small gold clusters doped by one and two boron atoms. *Journal of Computational Chemistry*, 35(32):2288–2296, 2014. (Cited on pages 8, 9, 21 and 62.)

[43] Sudip Pan, Diego Moreno, Jose Luis Cabellos, Jonathan Romero, Andres Reyes, Gabriel Merino, and Pratim K. Chattaraj. In quest of strong be-ng bonds among the neutral ng-be complexes. *The Journal of Physical Chemistry A*, 118(2):487–494, 2014. PMID: 24199587. (Cited on page 8.)

[44] Zhong-hua Cui, Yi-hong Ding, Jose Luis Cabellos, Edison Osorio, Rafael Islas, Albeiro Restrepo, and Gabriel Merino. Planar tetracoordinate carbons with a double bond in cal3e clusters. *Phys. Chem. Chem. Phys.*, 17:8769–8775, 2015. (Cited on pages 8 and 62.)

[45] Alba Vargas-Caamal, Sudip Pan, Filiberto Ortiz-Chi, Jose Luis Cabellos, Roberto A. Boto, Julia Contreras-Garcia, Albeiro Restrepo, Pratim K. Chattaraj, and Gabriel Merino. How strong are the metallocene-metallocene interactions? cases of ferrocene, ruthenocene, and osmocene. *Phys. Chem. Chem. Phys.*, 18:550–556, 2016. (Cited on page 8.)

[46] Alba Vargas Caamal, Jose Luis Cabellos, Filiberto Ortiz-Chi, Henry S. Rzepa, Albeiro Restrepo, and Gabriel Merino. How many water molecules does it take to dissociate hcl? *Chemistry A European Journal*, 22(8):2812–2818, 2016. (Cited on pages 8, 22, 24 and 37.)

[47] Zhong-hua Cui, Valentin Vassilev-Galindo, José Luis Cabellos, Edison Osorio, Mesías Orozco, Sudip Pan, Yi-hong Ding, and Gabriel Merino. Planar pentacoordinate carbon atoms embedded in a metallocene framework. *Chem. Commun.*, 53:138–141, 2017. (Cited on pages 8 and 62.)

[48] Alba Vargas-Caamal, Filiberto Ortiz-Chi, Diego Moreno, Albeiro Restrepo, Gabriel Merino, and Jose Luis Cabellos. The rich and complex potential energy surface of the ethanol dimer. *Theoretical Chemistry Accounts*, 134(2):16, 2015. (Cited on pages 8 and 62.)

[49] Elizabeth Flórez, Nancy Acelas, César Ibarguen, Sukanta Mondal, José Luis Cabellos, Gabriel Merino, and Albeiro Restrepo. Microsolvation of NO_3^-: structural exploration and bonding analysis. *RSC Adv.*, 6:71913–71923, 2016. (Cited on pages 8 and 62.)

[50] Osvaldo Yañez, Diego Inostroza, Brandon Usuga-Acevedo, Alejandro Vásquez-Espinal, Ricardo Pino-Rios, Mauricio Tabilo-Sepulveda, Jorge Garza, Jorge Barroso, Gabriel Merino, and William Tiznado. valuation of restricted probabilistic cellular automata on the exploration of the potential energy surface of $Be_6B_{11}^-$. *Theoretical Chemistry Accounts*, 139(3):139–147, 2020. (Cited on pages 9, 22, 29, 32, 44 and 49.)

[51] M. J. Frisch, G. W. Trucks, H. B. Schlegel, G. E. Scuseria, M. A. Robb, J. R. Cheeseman, G. Scalmani, V. Barone, B. Mennucci, G. A. Petersson, H. Nakatsuji, M. Caricato, X. Li, H. P. Hratchian, A. F. Izmaylov, J. Bloino, G. Zheng, J. L. Sonnenberg, M. Hada, M. Ehara, K. Toyota, R. Fukuda, J. Hasegawa,

M. Ishida, T. Nakajima, Y. Honda, O. Kitao, H. Nakai, T. Vreven, J. A. Montgomery, J. E. Peralta, F. Ogliaro, M. Bearpark, J. J. Heyd, E. Brothers, K. N. Kudin, V. N. Staroverov, R. Kobayashi, J. Normand, K. Raghavachari, A. Rendell, J. C. Burant, S. S. Iyengar, J. Tomasi, M. Cossi, N. Rega, J. M. Millam, M. Klene, J. E. Knox, J. B. Cross, V. Bakken, C. Adamo, J. Jaramillo, R. Gomperts, R. E. Stratmann, O. Yazyev, A. J. Austin, R. Cammi, C. Pomelli, J. W. Ochterski, R. L. Martin, K. Morokuma, V. G. Zakrzewski, G. A. Voth, P. Salvador, J. J. Dannenberg, S. Dapprich, A. D. Daniels, Farkas, J. B. Foresman, J. V. Ortiz, J. Cioslowski, and D. J. Fox. Gaussian 09, Revision B.01, 2009. (Cited on pages 9, 24, 25, 56, 58 and 62.)

[52] Terrell L. Hill. Thermodynamics of small systems. *The Journal of Chemical Physics*, 36(12):3182–3197, 1962. (Cited on pages 9, 23, 45 and 75.)

[53] Terrell L. Hill. Extension of nanothermodynamics to include a one dimensional surface excess. *Nano Letters*, 1(3):159–160, 2001. (Cited on pages 9 and 23.)

[54] T.L. Hill. *An Introduction to Statistical Thermodynamics*. Addison-Wesley series in chemistry. Dover Publications, 1986. (Cited on pages 9, 13 and 15.)

[55] Carlos Emiliano Buelna-García, Cesar Castillo-Quevedo, Jesus Manuel Quiroz-Castillo, Edgar Paredes-Sotelo, Manuel Cortez-Valadez, Martha Fabiola Martin-del Campo-Solis, Tzarara Lopez-Luke, Marycarmen Utrilla-Vázquez, Ana Maria Mendoza-Wilson, Peter L. Rodríguez-Kessler, Alejandro Vazquez-Espinal, Sudip Pan, Aned de Leon-Flores, Jhonny Robert Mis-May, Adán R. Rodríguez-Domínguez, Gerardo Martínez-Guajardo, and José Luis Cabellos. Relative populations and IR spectra of Cu_{38} cluster at finite temperature based on DFT and statistical thermodynamics calculations. *Frontiers in Chemistry*, 10, 2022. (Cited on pages 9, 15, 16 and 84.)

[56] Christopher Sutton and Sergey V. Levchenko. First-principles atomistic thermodynamics and configurational entropy. *Frontiers in Chemistry*, 8:757, 2020. (Cited on pages 9, 10 and 45.)

[57] Peter Kratzer and Jorg Neugebauer. The basics of electronic structure theory for periodic systems. *Frontiers in Chemistry*, 7, 2019. (Cited on page 10.)

[58] Eugenia Dzib, José Luis Cabellos, Filiberto Ortíz-Chi, Sudip Pan, Annia Galano, and Gabriel Merino. Eyringpy: A program for computing rate constants in the gas phase and in solution. *International Journal of Quantum Chemistry*, 119(2):e25686, 2019. (Cited on pages 10, 11, 13, 16, 22, 24 and 44.)

[59] D.A. McQuarrie and M.Q.D. A. *Statistical Mechanics*. Chemistry Series. Harper & Row, 1975. (Cited on pages 10, 11 and 15.)

[60] D.A. McQuarrie and J.D. Simon. *Molecular Thermodynamics*. University Science Books, 1999. (Cited on page 10.)

[61] Joseph Ochterski. *Thermochemistry in* Gaussian. 2000, Gaussian, Inc., 1996. (Cited on page 10.)

[62] F. Jensen. *Introduction to Computational Chemistry.* Wiley, 2017. (Cited on page 10.)

[63] Valeri G. Grigoryan and Michael Springborg. Temperature and isomeric effects in nanoclusters. *Phys. Chem. Chem. Phys.*, 21:5646–5654, 2019. (Cited on pages 10, 16, 22, 23, 24, 45, 58, 68 and 75.)

[64] Zhen Hua Li, Ahren W. Jasper, and Donald G. Truhlar. Structures, rugged energetic landscapes, and nanothermodynamics of Al_n (2<n< 65) particles. *Journal of the American Chemical Society*, 129(48):14899–14910, 2007. PMID: 17994736. (Cited on pages 10, 16, 45, 58, 75 and 81.)

[65] Zhen Hua Li and Donald G. Truhlar. Nanothermodynamics of metal nanoparticles. *Chem. Sci.*, 5:2605–2624, 2014. (Cited on pages 10, 23, 45, 58 and 75.)

[66] Georg Brehm, Markus Reiher, Boris Le Guennic, Michael Leibold, Siegfried Schindler, Frank W. Heinemann, and Siegfried Schneider. Investigation of the low-spin to high-spin transition in a novel [Fe(pmea)(NCS)2] complex by IR and raman spectroscopy and DFT calculations. *Journal of Raman Spectroscopy*, 37(1-3):108–122, 2006. (Cited on page 10.)

[67] Philipp Pracht and Stefan Grimme. Calculation of absolute molecular entropies and heat capacities made simple. *Chem. Sci.*, 12:6551–6568, 2021. (Cited on pages 10 and 11.)

[68] E.B. Wilson, J.C. Decius, and P.C. Cross. *Molecular Vibrations: The Theory of Infrared and Raman Vibrational Spectra.* Dover Books on Chemistry Series. Dover Publications, 1980. (Cited on page 11.)

[69] Donald G. Truhlar. A simple approximation for the vibrational partition function of a hindered internal rotation. *Journal of Computational Chemistry*, 12(2):266–270, 1991. (Cited on page 11.)

[70] Stefan Grimme. Supramolecular binding thermodynamics by dispersion-corrected density functional theory. *Chemistry - A European Journal*, 18(32):9955–9964, 2012. (Cited on page 11.)

[71] Ruth L. Jacobsen, Russell D. III Johnson, Karl K. Irikura, and Raghu N. Kacker. Anharmonic vibrational frequency calculations are not worthwhile for small basis sets. *Journal of Chemical Theory and Computation*, 9(2):951–954, 2013. PMID: 26588738. (Cited on page 11.)

[72] Peter R. Franke, John F. Stanton, and Gary E. Douberly. How to vpt2: Accurate and intuitive simulations of ch stretching infrared spectra using vpt2+k with large effective hamiltonian resonance treatments. *The Journal of Physical Chemistry A*, 125(6):1301–1324, 2021. PMID: 33506678. (Cited on page 11.)

[73] Alexander Laugier and József Garai. Derivation of the ideal gas law. *Journal of Chemical Education*, 84(11):1832, 2007. (Cited on page 12.)

[74] Adam W. Bushmaker, Vikram V. Deshpande, Scott Hsieh, Marc W. Bockrath, and Stephen B. Cronin. Direct observation of Born-Oppenheimer Approximation breakdown in carbon nanotubes. *Nano Letters*, 9(2):607–611, 2009. PMID: 19161322. (Cited on page 13.)

[75] Preeti Bhumla, Manish Kumar, and Saswata Bhattacharya. Theoretical insights into c-h bond activation of methane by transition metal clusters: the role of anharmonic effects. *Nanoscale Adv.*, 3:575–583, 2021. (Cited on page 16.)

[76] David Shortle. Propensities, probabilities, and the boltzmann hypothesis. *Computational and Theoretical Chemistry*, 12:1298–1302, 2003. (Cited on pages 16 and 24.)

[77] Ana María Mendoza-Wilson, René Renato Balandrán-Quintana, and José Luis Cabellos. Thermochemical behavior of sorghum procyanidin trimers with c4 c8 and c4 c6 interflavan bonds in the reaction with superoxide anion radical and h2o2 forming nadh-oxidase flavoenzyme. *Computational and Theoretical Chemistry*, 1186:112912, 2020. (Cited on pages 16, 22 and 74.)

[78] D. Schebarchov, F. Baletto, and D. J. Wales. Structure, thermodynamics, and rearrangement mechanisms in gold clusters insights from the energy landscapes framework. *Nanoscale*, 10:2004–2016, 2018. (Cited on pages 16, 22 and 23.)

[79] Bryan R. Goldsmith, Jacob Florian, Jin-Xun Liu, Philipp Gruene, Jonathan T. Lyon, David M. Rayner, André Fielicke, Matthias Scheffler, and Luca M. Ghiringhelli. Two to three dimensional transition in neutral gold clusters: The crucial role of van der waals interactions and temperature. *Phys. Rev. Materials*, 3:016002, Jan 2019. (Cited on pages 16, 22 and 23.)

[80] Vladimir Prelog. Chirality in chemistry. *Science*, 193(4247):17–24, 1976. (Cited on page 16.)

[81] Gerhard H. Fecher, Jurgen Kubler, and Claudia Felser. Chirality in the solid state: Chiral crystal structures in chiral and achiral space groups. *Materials*, 15(17), 2022. (Cited on page 16.)

[82] David Ayuso, Ofer Neufeld, Andres F. Ordonez, Piero Decleva, Gavriel Lerner, Oren Cohen, Misha Ivanov, and Olga Smirnova. Synthetic chiral light for efficient control of chiral light-matter interaction. *Nature Photonics*, 13(12):866–871, Dec 2019. (Cited on pages 17 and 44.)

[83] David Ayuso, Andres Ordonez, Piero Decleva, Misha Ivanov, and Olga Smirnova. Polarization of chirality, 2020. (Cited on pages 17 and 44.)

[84] Ping Guo, Biao Yang, Li Zhang, and Liang Zhao. Temperature dependent chiroptical response of sigmoidal gold clusters: probing the stability of chiral metal clusters. *Chem. Sci.*, 9:5614–5622, 2018. (Cited on pages 17 and 44.)

[85] Ariela W. Kaspi-Kaneti, Jorge Barroso, Gabriel Merino, David Avnir, Ignacio L. Garzon, and Inbal Tuvi-Arad. Head to tail distortion wave characterizes the enantiomerization of helicenes. *The Journal of Organic Chemistry*, 85(23):15415–15421, 2020. PMID: 33210538. (Cited on pages 17 and 44.)

[86] Wei-Li Li, Ya-Fan Zhao, Han-Shi Hu, Jun Li, and Lai-Sheng Wang. B_{30}^{-}: A quasiplanar chiral boron cluster. *Angewandte Chemie International Edition*, 53(22):5540–5545, 2014. (Cited on pages 17, 21, 43 and 44.)

[87] Jorge Barroso, Jose Luis Cabellos, Sudip Pan, Fernando Murillo, Ximena Zarate, Maria A. Fernandez-Herrera, and Gabriel Merino. Revisiting the racemization mechanism of helicenes. *Chem. Commun.*, 54:188–191, 2018. (Cited on pages 17, 44 and 60.)

[88] Daniel Ebeling, Marina Šekutor, Marvin Stiefermann, Jalmar Tschakert, Jeremy E. P. Dah, Robert M. K. Carlson, André Schirmeisen, and Peter R. Schreiner. Assigning the absolute configuration of single aliphatic molecules by visual inspection. *Nature Communications*, 9(1):2420, Jun 2018. (Cited on pages 17, 44 and 60.)

[89] Z. Tang. *Chiral Nanomaterials Preparation, Properties and Applications*. Wiley, 2017. (Cited on page 17.)

[90] Carlos Outeiral, Mark A. Vincent, Ángel Martín Pendás, and Paul L. A. Popelier. Revitalizing the concept of bond order through delocalization measures in real space. *Chem. Sci.*, 9:5517–5529, 2018. (Cited on page 17.)

[91] R. T. Sanderson. Principles of chemical bonding. *Journal of Chemical Education*, 38(8):382, 1961. (Cited on page 17.)

[92] Dmitry Yu. Zubarev and Alexander I. Boldyrev. Developing paradigms of chemical bonding: adaptive natural density partitioning. *Phys. Chem. Chem. Phys.*, 10:5207–5217, 2008. (Cited on pages 18 and 62.)

[93] Aungwa Francis, S. G. Abdu, Ali Haruna, and Eli Danladi. Computation of the cohesive energies of nacl, sio2 and al using density functional theory. *Physical Science International Journal*, 1(2):1–9, 2016. (Cited on page 18.)

[94] M. T. Yin and Marvin L. Cohen. Ground-state properties of diamond. *Phys. Rev. B*, 24:6121–6124, Nov 1981. (Cited on page 18.)

[95] C. Kittel. *Introduction to Solid State Physics*. Wiley, 1996. (Cited on page 18.)

[96] Alexandre Tkatchenko and Matthias Scheffler. Accurate molecular van der waals interactions from ground-state electron density and free-atom reference data. *Phys. Rev. Lett.*, 102:073005, Feb 2009. (Cited on page 18.)

[97] Sheh-Yi Sheu, Dah-Yen Yang, H. L. Selzle, and E. W. Schlag. Energetics of hydrogen bonds in peptides. *Proceedings of the National Academy of Sciences*, 100(22):12683–12687, 2003. (Cited on page 18.)

[98] Avik Halder, Larry A. Curtiss, Alessandro Fortunelli, and Stefan Vajda. Perspective: Size selected clusters for catalysis and electrochemistry. *The Journal of Chemical Physics*, 148(11):110901, 2018. (Cited on page 18.)

[99] Hyung Jun Park, Dong Jun Shin, and Junhua Yu. Categorization of quantum dots, clusters, nanoclusters, and nanodots. *Journal of Chemical Education*, 98(3):703–709, 2021. (Cited on page 19.)

[100] Carlos Emilano Buelna-García, César Castillo-Quevedo, Edgar Paredes-Sotelo, Gerardo Martinez-Guajardo, and José Luis Cabellos. Boltzmann populations of the fluxional $Be_6B_{11}^-$ and chiral Be_4B_8 clusters at finite temperatures computed by DFT and statistical thermodynamics. In Daniel Glossman-Mitnik, editor, *Density Functional Theory*, chapter 4. IntechOpen, Rijeka, 2021. (Cited on page 21.)

[101] Said Jalife, Lei Liu, Sudip Pan, José Luis Cabellos, Edison Osorio, Cheng Lu, Thomas Heine, Kelling J. Donald, and Gabriel Merino. Dynamical behavior of boron clusters. *Nanoscale*, 8:17639–17644, 2016. (Cited on pages 21, 22 and 45.)

[102] Hua-Jin Zhai, Ya-Fan Zhao, Wei-Li Li, Qiang Chen, Hui Bai, Han-Shi Hu, Zachary A. Piazza, Wen-Juan Tian, Hai-Gang Lu, Yan-Bo Wu, Yue-Wen Mu, Guang-Feng Wei, Zhi-Pan Liu, Jun Li, Si-Dian Li, and Lai-Sheng Wang. Observation of an all-boron fullerene. *Nature Chemistry*, pages 727–731, 2014. (Cited on pages 21, 22 and 43.)

[103] Weiguo Sun, Dongliang Kang, Bole Chen, Xiaoyu Kuang, Kewei Ding, and Cheng Lu. Tuning of structure evolution and electronic properties through palladium-doped boron clusters: PdB_{16} as a motif for boron-based nanotubes. *The Journal of Physical Chemistry A*, 1(10):123–134, 2020. PMID: 33085487. (Cited on pages 21 and 22.)

[104] Tian Jian, Xuenian Chen, Si-Dian Li, Alexander I. Boldyrev, Jun Li, and Lai-Sheng Wang. Probing the structures and bonding of size-selected boron and doped-boron clusters. *Chem. Soc. Rev.*, 48:3550–3591, 2019. (Cited on page 21.)

[105] Teng-Teng Chen, Wan-Lu Li, Wei-Jia Chen, Jun Li, and Lai-Sheng Wang. $La_3B_{14}^-$: an inverse triple-decker lanthanide boron cluster. *Chem. Commun.*, 55:7864–7867, 2019. (Cited on pages 21 and 22.)

[106] Gerardo Martínez-Guajardo, Jose Luis Cabellos, Andres Díaz-Celaya, Sudip Pan, Rafael Islas, Pratim K. Chattaraj, Thomas Heine, and Gabriel Merino. Dynamical behavior of borospherene a nanobubble. *Sci. Report*, 22:11287–11297, June 2015. (Cited on pages 21, 23, 45 and 75.)

[107] Kang Dongliang, Sun Weiguo, Shi Hongxiao, Lu Cheng, and Xiaoyu. Probing the structure and electronic properties of beryllium doped boron clusters: A planar BeB_{16} cluster motif for metallo-borophene. *Sci. Rep.*, 9:14367–14387, Oct 2019. (Cited on pages 21 and 44.)

[108] Penelope J. Brothers. Boron complexes of porphyrins and related polypyrrole ligands: unexpected chemistry for both boron and the porphyrin. *Chem. Commun.*, pages 2090–2102, 2008. (Cited on page 21.)

[109] Jonathan C. Axtell, Liban M. A. Saleh, Elaine A. Qian, Alex I. Wixtrom, and Alexander M. Spokoyny. Synthesis and applications of perfunctionalized boron clusters. *Inorganic Chemistry*, 57(5):2333–2350, 2018. PMID: 29465227. (Cited on pages 21 and 44.)

[110] Zachary A. Piazza, Han-Shi Hu, Wei-Li Li, Ya-Fan Zhao, Jun Li, and Lai-Sheng Wang. From planar boron clusters to borophenes and metalloborophenes. *Nature Reviews Chemistry*, 1(10):0071, 2017. (Cited on pages 21, 22, 43 and 44.)

[111] Andrew J. Mannix, Zhuhua Zhang, Nathan P. Guisinger, Boris I. Yakobson, and Mark C. Hersam. Borophene as a prototype for synthetic 2D materials development. *Nature Nanotechnology*, 13:444–450, 2018. (Cited on page 21.)

[112] N. Vast, S. Baroni, G. Zerah, J. M. Besson, A. Polian, M. Grimsditch, and J. C. Chervin. Lattice dynamics of icosahedral α-boron under pressure. *Phys. Rev. Lett.*, 78:693–696, Jan 1997. (Cited on page 21.)

[113] M. Fujimori, T. Nakata, T. Nakayama, E. Nishibori, K. Kimura, M. Takata, and M. Sakata. Peculiar covalent bonds in α-rhombohedral boron. *Phys. Rev. Lett.*, 82:4452–4455, May 1999. (Cited on page 21.)

[114] Hongxiao Shi, Xiaoyu Kuang, and Cheng Lu. LiB_{13}: A new member of tetrahedral-typed B_{13} ligand half-surround cluster. *Scientific Reports*, 10:1642–1651, March 2020. (Cited on page 21.)

[115] Zachary A. Piazza, Han-Shi Hu, Wei-Li Li, Ya-Fan Zhao, Jun Li, and Lai-Sheng Wang. Planar hexagonal B_{36} as a potential basis for extended single-atom layer boron sheets. *Nature Communications*, 1(1):3113, 2014. (Cited on pages 21, 22 and 43.)

[116] Qiang Chen, Teng-Teng Chen, Hai-Ru Li, Xiao-Yun Zhao, Wei-Jia Chen, Hua-Jin Zhai, Si-Dian Li, and Lai-Sheng Wang. B_{31}^- and B_{32}^-: chiral quasi-planar boron clusters. *Nanoscale*, 11:9698–9704, 2019. (Cited on pages 21 and 43.)

[117] Boggavarapu Kiran, Satya Bulusu, Hua-Jin Zhai, Soohaeng Yoo, Xiao Cheng Zeng, and Lai-Sheng Wang. Planar-to-tubular structural transition in boron clusters: B_{20} as the embryo of single-walled boron nanotubes. *Proceedings of the National Academy of Sciences*, 102(4):961–964, 2005. (Cited on pages 22 and 43.)

[118] Qiang Chen, Wei-Li Li, Ya-Fan Zhao, Su-Yan Zhang, Han-Shi Hu, Hui Bai, Hai-Ru Li, Wen-Juan Tian, Hai-Gang Lu, Hua-Jin Zhai, Si-Dian Li, Jun Li, and Lai-Sheng Wang. Experimental and theoretical evidence of an axially chiral borospherene. *ACS Nano*, 9(1):754–760, 2015. PMID: 25517915. (Cited on pages 22 and 44.)

[119] Ying-Jin Wang, Ya-Fan Zhao, Wei-Li Li, Tian Jian, Qiang Chen, Xue-Rui You, Ting Ou, Xiao-Yun Zhao, Hua-Jin Zhai, Si-Dian Li, Jun Li, and Lai-Sheng Wang. Observation and characterization of the smallest borospherene, B_{28}^- and B_{28}. *The Journal of Chemical Physics*, 144(6):064307, 2016. (Cited on pages 22 and 43.)

[120] Jian Lv, Yanchao Wang, Lijun Zhang, Haiqing Lin, Jijun Zhao, and Yanming Ma. Stabilization of fullerene-like boron cages by transition metal encapsulation. *Nanoscale*, 7:10482–10489, 2015. (Cited on pages 22 and 43.)

[121] Lin-Yan Feng, Jin-Chang Guo, Peng-Fei Li, and Hua-Jin Zhai. Boron-based chiral helix $Be_6B_{10}^{-2}$ and $Be_6B_{11}^-$ clusters: Structures, chemical bonding, and formation mechanism. *Chemistry - An Asian Journal*, 15(7):1094–1104, 2020. (Cited on pages 22, 43 and 44.)

[122] Andrew J. Mannix, Xiang-Feng Zhou, Brian Kiraly, Joshua D. Wood, Diego Alducin, Benjamin D. Myers, Xiaolong Liu, Brandon L. Fisher, Ulises Santiago, Jeffrey R. Guest, Miguel Jose Yacaman, Arturo Ponce, Artem R. Oganov, Mark C. Hersam, and Nathan P. Guisinger. Synthesis of borophenes: Anisotropic, two-dimensional boron polymorphs. *Science*, 350(6267):1513–1516, 2015. (Cited on page 22.)

[123] W. K. Barney, G. A. Sehmel, and W. E. Seymour. The use of boron carbide for reactor control. *Nuclear Science and Engineering*, 4(3):439–448, 1958. (Cited on page 22.)

[124] Zbigniew J. Leśnikowski. Challenges and opportunities for the application of boron clusters in drug design. *Journal of Medicinal Chemistry*, 59(17):7738–7758, 2016. PMID: 27124656. (Cited on page 22.)

[125] Fayaz Ali, Narayan S Hosmane, and Yinghuai Zhu. Boron chemistry for medical applications. *Molecules*, 25(4):828–835, 2020. (Cited on pages 22 and 44.)

[126] Ofelia B. Oña, Juan J. Torres-Vega, Alicia Torre, Luis Lain, Diego R. Alcoba, Alejandro Vásquez-Espinal, and William Tiznado. Chemical bonding analysis

in boron clusters by means of localized orbitals according to the electron localization function topology. *Theoretical Chemistry Accounts*, 134(28):28–37, 2015. (Cited on page 22.)

[127] Anastassia N. Alexandrova, Alexander I. Boldyrev, Hua-Jin Zhai, and Lai-Sheng Wang. All-boron aromatic clusters as potential new inorganic ligands and building blocks in chemistry. *Coordination Chemistry Reviews*, 250(21):2811 – 2866, 2006. 18th Main Group Chemistry. (Cited on page 22.)

[128] Dmitry Yu. Zubarev and Alexander I. Boldyrev. Comprehensive analysis of chemical bonding in boron clusters. *Journal of Computational Chemistry*, 28(1):251–268, 2007. (Cited on page 22.)

[129] Jordi Poater, Miquel Duran, Miquel Sola, and Bernard Silvi. Theoretical evaluation of electron delocalization in aromatic molecules by means of atoms in molecules (aim) and electron localization function (elf) topological approaches. *Chemical Reviews*, 105(10):3911–3947, 2005. PMID: 16218571. (Cited on page 22.)

[130] Marcos Mandado, María J. González-Moa, and Ricardo A. Mosquera. Qtaim n-center delocalization indices as descriptors of aromaticity in mono and poly heterocycles. *Journal of Computational Chemistry*, 28(1):127–136, 2007. (Cited on page 22.)

[131] Sudip Pan, Jorge Barroso, Said Jalife, Thomas Heine, Knut R. Asmis, and Gabriel Merino. Fluxional boron clusters: From theory to reality. *Accounts of Chemical Research*, 52(9):2732–2744, 2019. PMID: 31487150. (Cited on pages 22 and 43.)

[132] Ying-Jin Wang, Lin-Yan Feng, Jin-Chang Guo, and Hua-Jin Zhai. Dynamic Mg_2B_8 cluster: A nanoscale compass. *Chemistry - An Asian Journal*, 12(22):2899–2903, 2017. (Cited on page 22.)

[133] Huanchen Zhai and Anastassia N. Alexandrova. Fluxionality of catalytic clusters: When it matters and how to address it. *ACS Catalysis*, 7(3):1905–1911, 2017. (Cited on page 22.)

[134] Gabriel Merino and Thomas Heine. And yet it rotates: The starter for a molecular wankel motor. *Angewandte Chemie International Edition*, 51(41):10226–10227, 2012. (Cited on page 22.)

[135] Constantin Romanescu, Timur R. Galeev, Wei-Li Li, Alexander I. Boldyrev, and Lai-Sheng Wang. Transition-metal-centered monocyclic boron wheel clusters (M©Bn): A new class of aromatic borometallic compounds. *Accounts of Chemical Research*, 46(2):350–358, 2013. PMID: 23210660. (Cited on page 22.)

[136] Wei-yan Liang, Jorge Barroso, Said Jalife, Mesías Orozco-Ic, Ximena Zarate, Xue Dong, Zhong-hua Cui, and Gabriel Merino. B_10M_2 (m = rh, ir): finally a

stable boron-based icosahedral cluster. *Chem. Commun.*, 55:7490–7493, 2019. (Cited on page 22.)

[137] Teng-Teng Chen, Wan-Lu Li, Hui Bai, Wei-Jia Chen, Xin-Ran Dong, Jun Li, and Lai-Sheng Wang. ReB_8 and ReB_9^-: New members of the transition-metal-centered borometallic molecular wheel family. *The Journal of Physical Chemistry A*, 123(25):5317–5324, 2019. (Cited on page 22.)

[138] Xue Dong, Said Jalife, Alejandro Vásquez-Espinal, Jorge Barroso, Mesías Orozco-Ic, Estefanía Ravell, Jose Luis Cabellos, Wei-yan Liang, Zhong-hua Cui, and Gabriel Merino. Li_2B_{24}: the simplest combination for a three-ring boron tube. *Nanoscale*, 11:2143–2147, 2019. (Cited on pages 22 and 43.)

[139] Ivan A. Popov, Tian Jian, Gary V. Lopez, Alexander I. Boldyrev, and Lai-Sheng Wang. Cobalt-centred boron molecular drums with the highest coordination number in the CoB_{16}^- cluster. *Nature Communications*, 6:8654, 2015. (Cited on page 22.)

[140] Long Van Duong and Minh Tho Nguyen. Silicon doped boron clusters: how to make stable ribbons? *Phys. Chem. Chem. Phys.*, 19:14913–14918, 2017. (Cited on page 22.)

[141] Francisco Cervantes-Navarro, Gerardo Martínez-Guajardo, Edison Osorio, Diego Moreno, William Tiznado, Rafael Islas, Kelling J. Donald, and Gabriel Merino. Stop rotating! one substitution halts the B_{19}^- motor. *Chem. Commun.*, 50:10680–10682, 2014. (Cited on page 22.)

[142] Piero Ferrari, Jan Vanbuel, Klavs Hansen, Peter Lievens, Ewald Janssens, and André Fielicke. Effect of radiative cooling on the size-dependent stability of small boron clusters. *Phys. Rev. A*, 98:012501, Jul 2018. (Cited on page 22.)

[143] Gerardo Martínez-Guajardo, Alina P. Sergeeva, Alexander I. Boldyrev, Thomas Heine, Jesus M. Ugalde, and Gabriel Merino. Unravelling phenomenon of internal rotation in B_{13}^+ through chemical bonding analysis. *Chem. Commun.*, 47:6242–6244, 2011. (Cited on page 22.)

[144] Diego Moreno, Sudip Pan, Lei Liu Zeonjuk, Rafael Islas, Edison Osorio, Gerardo Martínez-Guajardo, Pratim K. Chattaraj, Thomas Heine, and Gabriel Merino. B_{18}: a quasi-planar bowl member of the wankel motor family. *Chem. Commun.*, 50:8140–8143, 2014. (Cited on pages 22 and 43.)

[145] Truong Ba Tai, Arnout Ceulemans, and Minh Tho Nguyen. Disk aromaticity of the planar and fluxional anionic boron clusters ${B_{20}}^{-/2-}$. *Chemistry - A European Journal*, 18(15):4510–4512, 2012. (Cited on page 22.)

[146] Matias R. Fagiani, Xiaowei Song, Petko Petkov, Sreekanta Debnath, Sandy Gewinner, Wieland Schöllkopf, Thomas Heine, André Fielicke, and Knut R. Asmis. Structure and fluxionality of B_{13}^+ probed by infrared photodissociation

spectroscopy. *Angewandte Chemie International Edition*, 56(2):501–504, 2017. (Cited on pages 22, 23 and 45.)

[147] Yonggang Yang, Dongming Jia, Ying-Jin Wang, Hua-Jin Zhai, Yuan Man, and Si-Dian Li. A universal mechanism of the planar boron rotors B_{11}^-, B_{13}^+, B_{15}^+, and B_{19}^-: inner wheels rotating in pseudo-rotating outer bearings. *Nanoscale*, 9:1443–1448, 2017. (Cited on pages 22 and 44.)

[148] Ying-Jin Wang, Xiao-Yun Zhao, Qiang Chen, Hua-Jin Zhai, and Si-Dian Li. B_{11}^-: a moving subnanoscale tank tread. *Nanoscale*, 7:16054–16060, 2015. (Cited on page 22.)

[149] Ying-Jin Wang, Jin-Chang Guo, and Hua-Jin Zhai. Why nanoscale tank treads move? structures, chemical bonding, and molecular dynamics of a doped boron cluster $B_{10}C$. *Nanoscale*, 9:9310–9316, 2017. (Cited on page 22.)

[150] F. Calvo, J. P. K. Doye, and D. J. Wales. Quantum partition functions from classical distributions: Application to rare-gas clusters. *The Journal of Chemical Physics*, 114(17):7312–7329, 2001. (Cited on page 22.)

[151] C. Bréchignac, Ph. Cahuzac, M. de Frutos, N. Kebaïli, A. Sarfati, and V. Akulin. Experimental evidence for the entropy effect in coulombic cluster fission. *Phys. Rev. Lett.*, 77:251–254, Jul 1996. (Cited on page 22.)

[152] D.M. Foster, R. Ferrando, and R.E. Palmer. Experimental determination of the energy difference between competing isomers of deposited, size-selected gold nanoclusters. *Nature Communications*, 9:1323–1334, Apr 2018. (Cited on page 22.)

[153] A.I. Shkrebtii, J. Heron, J.L. Cabellos, N. Witkowski, O. Pluchery, B.S. Mendoza, and Y. Borensztein. Temperature dependent optical response of Si(100): Theory vs. experiment. *MRS Proceedings*, 1370:mrss11–1370–yy05–10, 2011. (Cited on page 22.)

[154] Luca M Ghiringhelli, Philipp Gruene, Jonathan T Lyon, David M Rayner, Gerard Meijer, André Fielicke, and Matthias Scheffler. Not so loosely bound rare gas atoms: finite temperature vibrational fingerprints of neutral gold cluster complexes. *New Journal of Physics*, 15(8):083003, aug 2013. (Cited on pages 22 and 23.)

[155] Ari P. Seitsonen, Kari Laasonen, R. M. Nieminen, and Michael L. Klein. Structure of cal12. *The Journal of Chemical Physics*, 103(18):8075–8080, 1995. (Cited on pages 23 and 45.)

[156] Prachi Chandrachud, Kavita Joshi, and D. G. Kanhere. Thermodynamics of carbon doped al and ga clusters: Ab initio molecular dynamics simulations. *Phys. Rev. B*, 76:235423, Dec 2007. (Cited on page 23.)

[157] Koichi Ohno and Satoshi Maeda. Global reaction route mapping on potential energy surfaces of formaldehyde, formic acid, and their metal-substituted analogues. *The Journal of Physical Chemistry A*, 110(28):8933–8941, 2006. PMID: 16836457. (Cited on pages 23 and 75.)

[158] Bjørn A. Strøm, Jean Marc Simon, Sondre K. Schnell, Signe Kjelstrup, Jianying He, and Dick Bedeaux. Size and shape effects on the thermodynamic properties of nanoscale volumes of water. *Phys. Chem. Chem. Phys.*, 19:9016–9027, 2017. (Cited on page 23.)

[159] J.W. Gibbs. *Thermodynamics*. Scientific Papers. Dover Publications, 1961. (Cited on page 23.)

[160] Florent Calvo. Thermodynamics of nanoalloys. *Phys. Chem. Chem. Phys.*, 17:27922–27939, 2015. (Cited on page 23.)

[161] M. Bixon and Joshua Jortner. Energetic and thermodynamic size effects in molecular clusters. *The Journal of Chemical Physics*, 91(3):1631–1642, 1989. (Cited on pages 23 and 75.)

[162] W. Damgaard Kristensen, E. J. Jensen, and R. M. J. Cotterill. Thermodynamics of small clusters of atoms: A molecular dynamics simulation. *The Journal of Chemical Physics*, 60(11):4161–4169, 1974. (Cited on page 23.)

[163] David J. Wales. Structure, dynamics, and thermodynamics of clusters: Tales from topographic potential surfaces. *Science*, 271(5251):925–929, 1996. (Cited on pages 23 and 75.)

[164] P. Jena, S.N. Khanna, and B.K. Rao. *Physics and Chemistry of Finite Systems From Clusters to Crystals*. Number v. 2 in NATO ASI Series : advanced science institutes series: Series C, Mathematical and physical sciences. Kluwer Academic Publishers, 1992. (Cited on page 23.)

[165] H. Fox, A. P. Horsfield, and M. J. Gillan. Density functional calculations of surface free energies. *The Journal of Chemical Physics*, 124(13):134709, 2006. (Cited on pages 23 and 45.)

[166] Elizabeth C. Beret, Luca M. Ghiringhelli, and Matthias Scheffler. Free gold clusters: beyond the static, monostructure description. *Faraday Discuss.*, 152:153–167, 2011. (Cited on page 23.)

[167] Zhen-Long Lv, Kai Xu, Yan Cheng, Xiang-Rong Chen, and Ling-Cang Cai. Ab initio investigation of the lower energy candidate structures for $(H_2O)_5^+$ water cluster. *The Journal of Chemical Physics*, 141(5):054309, 2014. (Cited on page 23.)

[168] Alhadji Malloum, Jean Jules Fifen, Zoubeida Dhaouadi, Serge Guy Nana Engo, and Nejm-Eddine Jaidane. Structures and relative stabilities of ammonia clusters at different temperatures dft vs. ab initio. *Phys. Chem. Chem. Phys.*, 17:29226–29242, 2015. (Cited on page 23.)

[169] Alhadji Malloum, Jean Jules Fifen, Zoubeida Dhaouadi, Serge Guy Nana Engo, and Nejm-Eddine Jaidane. Structures and spectroscopy of medium size protonated ammonia clusters at different temperatures h^+ (nh_3). *The Journal of Chemical Physics*, 146(4):044305, 2017. (Cited on pages 23 and 24.)

[170] Alhadji Malloum, Jean Jules Fifen, and Jeanet Conradie. Structures and infrared spectroscopy of large sized protonated ammonia clusters. *The Journal of Chemical Physics*, 149(24):244301, 2018. (Cited on page 23.)

[171] Jean Jules Fifen and Noam Agmon. Structure and spectroscopy of hydrated sodium ions at different temperatures and the cluster stability rules. *Journal of Chemical Theory and Computation*, 12(4):1656–1673, 2016. PMID: 26913993. (Cited on page 23.)

[172] Philipp Gruene, David M. Rayner, Britta Redlich, Alexander F. G. van der Meer, Jonathan T. Lyon, Gerard Meijer, and André Fielicke. Structures of neutral au7, au19, and au20 clusters in the gas phase. *Science*, 321(5889):674–676, 2008. (Cited on page 23.)

[173] André Fielicke, Gert von Helden, Gerard Meijer, David B. Pedersen, Benoit Simard, and David M. Rayner. Gold cluster carbonyls saturated adsorption of co on gold cluster cations, vibrational spectroscopy, and implications for their structures. *Journal of the American Chemical Society*, 127(23):8416–8423, 2005. PMID: 15941275. (Cited on page 23.)

[174] André Fielicke, Andrei Kirilyuk, Christian Ratsch, Jörg Behler, Matthias Scheffler, Gert von Helden, and Gerard Meijer. Structure determination of isolated metal clusters via far-infrared spectroscopy. *Phys. Rev. Lett.*, 93:023401, Jul 2004. (Cited on page 23.)

[175] Christoph Sieber, Jean Buttet, Wolfgang Harbich, Christian Félix, Roland Mitrić, and Vlasta Bonači ć Koutecký. Isomer-specific spectroscopy of metal clusters trapped in a matrix: ag_9. *Phys. Rev. A*, 70:041201, Oct 2004. (Cited on pages 23, 24 and 37.)

[176] Simon J. Teague. Implications of protein flexibility for drug discovery. *Nature Reviews Drug Discovery*, 2:527–541, July 2003. (Cited on page 24.)

[177] Wei An, Satya Bulusu, Yi Gao, and X. C. Zeng. Relative stability of planar versus double-ring tubular isomers of neutral and anionic boron cluster B_{20} and B_{20}^-. *The Journal of Chemical Physics*, 124(15):154310, 2006. (Cited on pages 24 and 43.)

[178] James Kubicki and Heath Watts. Quantum mechanical modeling of the vibrational spectra of minerals with a focus on clays. *Minerals*, 9(3):141, Feb 2019. (Cited on pages 24 and 44.)

[179] Carlo Adamo and Vincenzo Barone. Toward reliable density functional methods without adjustable parameters: The PBE0 model. *The Journal of Chemical Physics*, 110(13):6158–6170, 1999. (Cited on pages 25 and 133.)

[180] Florian Weigend and Reinhart Ahlrichs. Balanced basis sets of split valence, triple zeta valence and quadruple zeta valence quality for H to Rn: Design and assessment of accuracy. *Phys. Chem. Chem. Phys.*, 7:3297–3305, 2005. (Cited on page 25.)

[181] Stefan Grimme, Jens Antony, Stephan Ehrlich, and Helge Krieg. A consistent and accurate ab initio parametrization of density functional dispersion correction (dft-d) for the 94 elements h-pu. *The Journal of Chemical Physics*, 132(15):154104, 2010. (Cited on pages 25, 61 and 75.)

[182] Li-Li Pan, Jun Li, and Lai-Sheng Wang. Low-lying isomers of the b_9^- boron cluster: The planar molecular wheel versus three-dimensional structures. *The Journal of Chemical Physics*, 129(2):024302, 2008. (Cited on page 25.)

[183] Yoshiaki Shoji, Tsukasa Matsuo, Daisuke Hashizume, Matthias J. Gutmann, Hiroyuki Fueno, Kazuyoshi Tanaka, and Kohei Tamao. Boron-boron σ-bond formation by two-electron reduction of a h-bridged dimer of monoborane. *Journal of the American Chemical Society*, 133(29):11058–11061, 2011. PMID: 21711029. (Cited on page 26.)

[184] Hua-Jin Zhai, Anastassia N. Alexandrova, K. Alexander Birch, Alexander I. Boldyrev, and Lai-Sheng Wang. Hepta- and octacoordinate boron in molecular wheels of eight- and nine-atom boron clusters: Observation and confirmation. *Angewandte Chemie International Edition*, 42(48):6004–6008, 2003. (Cited on page 26.)

[185] Afarin Moezzi, Marilyn M. Olmstead, and Philip P. Power. Boron-boron double bonding in the species $[B_2R_4]2^-$: synthesis and structure of $[(Et_2O)$Li2Mes2BB(Mes)Ph], a diborane(4) dianion analog of a substituted ethylene. *Journal of the American Chemical Society*, 114(7):2715–2717, 1992. (Cited on pages 27 and 46.)

[186] Mingfei Zhou, Nobuko Tsumori, Zhenhua Li, Kangnian Fan, Lester Andrews, and Qiang Xu. Ocbbco: A neutral molecule with some boron-boron triple bond character. *Journal of the American Chemical Society*, 124(44):12936–12937, 2002. PMID: 12405806. (Cited on pages 27 and 46.)

[187] Ferran Feixas, Eduard Matito, Jordi Poater, and Miquel Sola. Understanding conjugation and hyperconjugation from electronic delocalization measures.

The Journal of Physical Chemistry A, 115(45):13104–13113, 2011. PMID: 21932863. (Cited on page 27.)

[188] Andrea Szabo, Attila Kovacs, and Gernot Frenking. Theoretical studies of inorganic compounds. 341) energy decomposition analysis of E-E bonding in planar and perpendicular X2E-EX2 (E = B, Al, Ga, In, Tl; X = H, F, Cl, Br, I). *Zeitschrift für anorganische und allgemeine Chemie*, 631(10):1803–1809, 2005. (Cited on page 27.)

[189] Gerald Geudtner, Patrizia Calaminici, Javier Carmona-Espíndola, Jorge Martín del Campo, Víctor Daniel Domínguez-Soria, Robert Flores Moreno, Gabriel Ulises Gamboa, Annick Goursot, Andreas M. Köster, José Ulises Reveles, Tzonka Mineva, José Manuel Vásquez-Pérez, Alberto Vela, Bernardo Zúñinga Gutierrez, and Dennis R. Salahub. deMon2k. *WIREs Computational Molecular Science*, 2(4):548–555, 2012. (Cited on pages 35, 58 and 84.)

[190] C. Spickermann. *Entropies of Condensed Phases and Complex Systems: A First Principles Approach*. Springer Theses. Springer Berlin Heidelberg, 2011. (Cited on page 36.)

[191] Takahiro Kondo. Recent progress in boron nanomaterials. *Science and technology of advanced materials*, 18(1):780–804, Oct 2017. (Cited on page 43.)

[192] N. Kabay, M. Bryjak, and N. Hilal. *Boron Separation Processes*. Elsevier Science, 2015. (Cited on page 43.)

[193] Tahere Kheshti, Zabiollah Mahdavifar, and Siamak Noorizadeh. Umbrella-shaped vs planar; evolutionary search for bnq, BeB_n^Q (n=6-12, q=0, -1) clusters. *Journal of Molecular Liquids*, 328:115389, 2021. (Cited on page 43.)

[194] Heather DeFrancesco, Joshua Dudley, and Adiel Coca. *Boron Chemistry: An Overview*, chapter 1, pages 1–25. ACS Publications, 2016. (Cited on page 43.)

[195] Truong Ba Tai and Minh Tho Nguyen. A new chiral boron cluster B_{44} containing nonagonal holes. *Chem. Commun.*, 52:1653–1656, 2016. (Cited on pages 43 and 44.)

[196] M. Frederick Hawthorne. The role of chemistry in the development of boron neutron capture therapy of cancer. *Angewandte Chemie International Edition in English*, 32(7):950–984, 1993. (Cited on page 44.)

[197] Lara Pizzorno. Nothing boring about boron. *Integrative medicine (Encinitas, Calif.)*, 14(4):35–48, Aug 2015. (Cited on page 44.)

[198] A. R. Oganov and V. L. Solozhenko. Boron: a hunt for superhard polymorphs. *Journal of Superhard Materials*, 31(5):285, Nov 2009. (Cited on page 44.)

[199] Enis Fakioglu, Yuda Yurum, and T Nejat Veziroglu. A review of hydrogen storage systems based on boron and its compounds. *International Journal of Hydrogen Energy*, 29(13):1371–1376, 2004. (Cited on page 44.)

[200] H.R. Jiang, Ziheng Lu, M.C. Wu, Francesco Ciucci, and T.S. Zhao. Borophene: A promising anode material offering high specific capacity and high rate capability for lithium-ion batteries. *Nano Energy*, 23:97–104, 2016. (Cited on page 44.)

[201] Pei Liang, Yanting Cao, Bo Tai, Lin Zhang, Haibo Shu, Feng Li, Dongliang Chao, and Xiaoqing Du. Is borophene a suitable anode material for sodium ion battery? *Journal of Alloys and Compounds*, 704:152–159, 2017. (Cited on page 44.)

[202] Yang Zhang, Zhi-Feng Wu, Peng-Fei Gao, Sheng-Li Zhang, and Yu-Hua Wen. Could borophene be used as a promising anode material for high-performance lithium ion battery? *ACS Applied Materials & Interfaces*, 8(34):22175–22181, 2016. PMID: 27487298. (Cited on page 44.)

[203] Ning Jiang, Biao Li, Fanghua Ning, and Dingguo Xia. All boron-based 2d material as anode material in li-ion batteries. *Journal of Energy Chemistry*, 27(6):1651–1654, 2018. (Cited on page 44.)

[204] Showkat H. Mir, Sudip Chakraborty, Prakash C. Jha, John Warna, Himadri Soni, Prafulla K. Jha, and Rajeev Ahuja. Two-dimensional boron lightest catalyst for hydrogen and oxygen evolution reaction. *Applied Physics Letters*, 109(5):053903, 2016. (Cited on page 44.)

[205] Zhenguo Huang, Suning Wang, Rian D. Dewhurst, Nikolai V. Ignat'ev, Maik Finze, and Holger Braunschweig. Boron: Its role in energy-related processes and applications. *Angewandte Chemie International Edition*, 59(23):8800–8816, 2020. (Cited on page 44.)

[206] Xinlei Yu, Chang Xu, and Longjiu Cheng. Theoretical investigation on anti-sandwich beryllium-boron clusters $Be_{2m}B_n$ (m=1-3): Fluxionality and multi-aromaticity. *Computational and Theoretical Chemistry*, 1188:112949, 2020. (Cited on page 44.)

[207] Zhong-hua Cui, Wen-sheng Yang, Lili Zhao, Yi-hong Ding, and Gernot Frenking. Unusually short be-be distances with and without a bond in Be_2F_2 and in the molecular discuses Be_2B_8 and $Be_2B_7^-$. *Angewandte Chemie International Edition*, 55(27):7841–7846, 2016. (Cited on pages 44 and 47.)

[208] Andreas Hermann, N. W. Ashcroft, and Roald Hoffmann. Binary compounds of boron and beryllium: A rich structural arena with space for predictions. *Chemistry - A European Journal*, 19(13):4184–4197, 2013. (Cited on page 44.)

[209] Lin-Yan Feng, Jin-Chang Guo, Peng-Fei Li, and Hua-Jin Zhai. Boron-based binary $Be_6B_{10}^{2-}$ cluster three-layered aromatic sandwich, electronic transmutation, and dynamic structural fluxionality. *Phys. Chem. Chem. Phys.*, 20:22719–22729, 2018. (Cited on page 44.)

[210] Li-Hua Han, Ying-Jin Wang, and Hua-Jin Zhai. Boron-based $Be_2B_5^+0$- alloy clusters: inverse sandwiches with pentagonal boron ring and reduction-induced structural transformation to molecular wheel structure. *New J. Chem.*, 45:4675–4682, 2021. (Cited on page 44.)

[211] Tatyana N. Gribanova, Ruslan M. Minyaev, and Vladimir I. Minkin. Stabilization of non-typical forms of boron clusters by beryllium doping. *Chemical Physics*, 522:44–54, 2019. (Cited on page 44.)

[212] Tatyana N. Gribanova, Ruslan M. Minyaev, Vladimir I. Minkin, and Alexander I. Boldyrev. Novel architectures of boron. *Structural Chemistry*, 31(6):2105–2128, Dec 2020. (Cited on page 44.)

[213] Hai-Ru Li, Hui Liu, Xin-Xin Tian, Wen-Yan Zan, Yue-Wen Mu, Hai-Gang Lu, Jun Li, Yue-Kui Wang, and Si-Dian Li. Structural transition in metal-centered boron clusters from tubular molecular rotors $Ta@B_{21}$ and $Ta@B_{22}{}^+$ to cage-like endohedral metalloborospherene $Ta@B22^-$. *Phys. Chem. Chem. Phys.*, 19:27025–27030, 2017. (Cited on page 44.)

[214] P.J. Stephens, F.J. Devlin, and J.R. Cheeseman. *VCD Spectroscopy for Organic Chemists*. Taylor & Francis, 2012. (Cited on pages 44 and 45.)

[215] P. Ulrich Biedermann, James R. Cheeseman, Michael J. Frisch, Volker Schurig, Ivan Gutman, and Israel Agranat. Conformational spaces and absolute configurations of chiral fluorinated inhalation anaesthetics. a theoretical study. *The Journal of Organic Chemistry*, 64(11):3878–3884, 1999. (Cited on page 44.)

[216] Ahmed Aamouche, Frank J. Devlin, Philip J. Stephens, Jozef Drabowicz, Bogdan Bujnicki, and Marian Mikolajczyk. Vibrational circular dichroism and absolute configuration of chiral sulfoxides: tert-butyl methyl sulfoxide. *Chemistry - A European Journal*, 6(24):4479–4486, 2000. (Cited on pages 44 and 45.)

[217] Valentin Paul Nicu, Attila Mándi, Tibor Kurtán, and Prasad L. Polavarapu. On the complementarity of ecd and vcd techniques. *Chirality*, 26(9):525–531, 2014. (Cited on page 44.)

[218] Ettore Castiglioni, Paolo Biscarini, and Sergio Abbate. Experimental aspects of solid state circular dichroism. *Chirality*, 21(1E):E28–E36, 2009. (Cited on page 44.)

[219] J. R. Avilés Moreno, M. M. Quesada Moreno, J. J. López González, R. M. Claramunt, C. López, I. Alkorta, and J. Elguero. Self-assembly structures of

1h-indazoles in the solution and solid phases: A vibrational (ir, fir, raman, and vcd) spectroscopy and computational study. *ChemPhysChem*, 14(14):3355–3360, 2013. (Cited on page 44.)

[220] Juan Ramón Aviles-Moreno, Elena Urena Horno, Francisco Partal Urena, and Juan Jesús López González. Ir-raman-vcd study of r-(+)-pulegone: Influence of the solvent. *Spectrochimica Acta Part A: Molecular and Biomolecular Spectroscopy*, 79(4):767–776, 2011. The Xth International Conference on Molecular Spectroscopy. (Cited on page 44.)

[221] Francisco Partal Ureña, Juan Ramón Avilés Moreno, and Juan Jesús López González. Conformational flexibility in terpenes: Vibrational circular dichroism (vcd), infrared and raman study of s-perillaldehyde. *The Journal of Physical Chemistry A*, 112(34):7887–7893, 2008. (Cited on page 44.)

[222] T.R. Huet, J.-R. Aviles Moreno, O. Pirali, M. Tudorie, F. Partal Ureña, and J.-J. Lopez Gonzalez. Terpenes in the gas phase: The far-ir spectrum of perillaldehyde. *Journal of Quantitative Spectroscopy and Radiative Transfer*, 113(11):1261–1265, 2012. Three Leaders in Spectroscopy. (Cited on page 44.)

[223] Guochun Yang and Yunjie Xu. *Vibrational Circular Dichroism Spectroscopy of Chiral Molecules*, pages 189–236. Springer Berlin Heidelberg, Berlin, Heidelberg, 2011. (Cited on page 44.)

[224] L. A. Nafie, J. C. Cheng, and P. J. Stephens. Vibrational circular dichroism of 2,2,2-trifluoro-1-phenylethanol. *Journal of the American Chemical Society*, 97(13):3842–3843, 1975. (Cited on page 44.)

[225] Edward C. Sherer, Claire H. Lee, Joseph Shpungin, James F. Cuff, Chenxiao Da, Richard Ball, Richard Bach, Alejandro Crespo, Xiaoyi Gong, and Christopher J. Welch. Systematic approach to conformational sampling for assigning absolute configuration using vibrational circular dichroism. *Journal of Medicinal Chemistry*, 57(2):477–494, 2014. PMID: 24383452. (Cited on page 44.)

[226] Philip J. Stephens, Frank J. Devlin, and Jian-Jung Pan. The determination of the absolute configurations of chiral molecules using vibrational circular dichroism (vcd) spectroscopy. *Chirality*, 20(5):643–663, 2008. (Cited on page 44.)

[227] N. David Mermin. Thermal properties of the inhomogeneous electron gas. *Phys. Rev.*, 137:A1441–A1443, Mar 1965. (Cited on page 45.)

[228] S. Pittalis, C. R. Proetto, A. Floris, A. Sanna, C. Bersier, K. Burke, and E. K. U. Gross. Exact conditions in finite-temperature density-functional theory. *Phys. Rev. Lett.*, 107:163001, Oct 2011. (Cited on page 45.)

[229] A. Gonis. Extension of the kohn-sham formulation of density functional theory to finite temperature. *Journal of Physics and Chemistry of Solids*, 116:86–99, 2018. (Cited on page 45.)

[230] Helmut Eschrig. T> 0 ensemble-state density functional theory via legendre transform. *Phys. Rev. B*, 82:205120, Nov 2010. (Cited on page 45.)

[231] David J. Wales. Structure, dynamics, and thermodynamics of clusters tales from topographic potential surfaces. *Science*, 271(5251):925–929, 1996. (Cited on page 45.)

[232] Philip J. Stephens. Philip j. stephens: A scientific memoir. *Theoretical Chemistry Accounts*, 119(1):5–18, Jan 2008. (Cited on page 45.)

[233] L.A. Nafie. *Vibrational Optical Activity: Principles and Applications*. Wiley, 2011. (Cited on page 45.)

[234] Laurence A. Nafie. Infrared and raman vibrational optical activity: Theoretical and experimental aspects. *Annual Review of Physical Chemistry*, 48(1):357–386, 1997. PMID: 9348659. (Cited on page 45.)

[235] Yanan He, Bo Wang, Rina K. Dukor, and Laurence A. Nafie. Determination of absolute configuration of chiral molecules using vibrational optical activity: A review. *Applied Spectroscopy*, 65(7):699–723, 2011. PMID: 21740631. (Cited on page 45.)

[236] E. de la Puente, A. Aguado, A. Ayuela, and J. M. López. Structural and electronic properties of small neutral $(MgO)_n$ clusters. *Phys. Rev. B*, 56:7607–7614, Sep 1997. (Cited on pages 49, 52, 74 and 78.)

[237] John A. Pople, Martin Head Gordon, and Krishnan Raghavachari. Quadratic configuration interaction. a general technique for determining electron correlation energies. *The Journal of Chemical Physics*, 87(10):5968–5975, 1987. (Cited on page 50.)

[238] Gerardo Hernández-Juárez, Estefanáa Ravell, Jessica Arcudia, Ximena Zarate, Zhong-hua Cui, Gabriel Merino, and Jorge Barroso. Structural effects of alkali-metals on the b_{12} skeleton. *Phys. Chem. Chem. Phys.*, 22:17344–17350, 2020. (Cited on pages 50 and 62.)

[239] Jianmin Tao, John P. Perdew, Viktor N. Staroverov, and Gustavo E. Scuseria. Climbing the density functional ladder: nonempirical meta generalized gradient approximation designed for molecules and solids. *Phys. Rev. Lett.*, 91:146401, Sep 2003. (Cited on pages 52 and 133.)

[240] Prince Ravat. Carbo[n]helicenes restricted to enantiomerize: an insight into the design process of configurationally stable functional chiral pahs. *Chemistry - A European Journal*, 27(12):3957–3967, 2021. (Cited on page 52.)

[241] Sami Malola and Hannu Hakkinen. Chiral inversion of thiolate-protected gold nanoclusters via core reconstruction without breaking a au-s bond. *Journal of the American Chemical Society*, 141(14):6006–6012, 2019. PMID: 30889350. (Cited on page 53.)

[242] Kurt R. Glaesemann and Laurence E. Fried. Quantitative molecular thermochemistry based on path integrals. *The Journal of Chemical Physics*, 123(3):034103, 2005. (Cited on page 56.)

[243] Olle Hellman, Peter Steneteg, I. A. Abrikosov, and S. I. Simak. Temperature dependent effective potential method for accurate free energy calculations of solids. *Phys. Rev. B*, 87:104111, Mar 2013. (Cited on page 56.)

[244] Göran Grimvall, Blanka Magyari-Köpe, Vidvuds Ozoliņš, and Kristin A. Persson. Lattice instabilities in metallic elements. *Rev. Mod. Phys.*, 84:945–986, Jun 2012. (Cited on page 56.)

[245] Jörg Neugebauer and Tilmann Hickel. Density functional theory in materials science. *WIREs Computational Molecular Science*, 3(5):438–448, 2013. (Cited on page 56.)

[246] Min Li, Jun Wang, Baoqin Fu, and Qing Hou. A molecular dynamics study of melting and dissociation of tungsten nanoparticles. *AIP Advances*, 5(12):127131, 2015. (Cited on page 58.)

[247] Anderson S. Chaves, Maurício J. Piotrowski, and Juarez L. F. Da Silva. Evolution of the structural, energetic, and electronic properties of the 3d, 4d, and 5d transition-metal clusters (30 TM_n systems for n = 2-15): a density functional theory investigation. *Phys. Chem. Chem. Phys.*, 19:15484–15502, 2017. (Cited on pages 59, 60 and 64.)

[248] Wei Chen and Shaowei Chen. Oxygen electroreduction catalyzed by gold nanoclusters: Strong core size effects. *Angewandte Chemie International Edition*, 48(24):4386–4389, 2009. (Cited on page 59.)

[249] Claude R. Henry. Surface studies of supported model catalysts. *Surface Science Reports*, 31(7):231–325, 1998. (Cited on page 59.)

[250] Beatriz Santiago González, María J. Rodríguez, Carmen Blanco, José Rivas, M. Arturo López-Quintela, and José M. Gaspar Martinho. One step synthesis of the smallest photoluminescent and paramagnetic pvp-protected gold atomic clusters. *Nano Letters*, 10(10):4217–4221, 2010. PMID: 20836542. (Cited on page 59.)

[251] William L. Barnes, Alain Dereux, and Thomas W. Ebbesen. Surface plasmon subwavelength optics. *Nature*, 424(6950):824–830, Aug 2003. (Cited on page 59.)

[252] Nicole Cathcart and Vladimir Kitaev. Silver nanoclusters: Single-stage scaleable synthesis of monodisperse species and their chirooptical properties. *The Journal of Physical Chemistry C*, 114(38):16010–16017, 2010. (Cited on page 59.)

[253] Xun-Lei Ding, Wei Xue, Yan-Ping Ma, Zhe-Chen Wang, and Sheng-Gui He. Density functional study on cage and noncage $(Fe_{42}O_3)_n$ clusters. *The Journal of Chemical Physics*, 130(1):014303, 2009. (Cited on page 59.)

[254] Abdul Majid, Sunbul Zahid, Salah Ud-Din Khan, and Shahab Ud-Din Khan. Theoretical study of $(TM)FeO_3$ (tm = 3d transition metals) molecular clusters. *Journal of Nanoparticle Research*, 22(6):145, May 2020. (Cited on page 59.)

[255] Jiatao Zhang, Junfeng Liu, Qing Peng, Xun Wang, and Yadong Li. Nearly monodisperse Cu_2O and CuO nanospheres: preparation and applications for sensitive gas sensors. *Chemistry of Materials*, 18(4):867–871, Feb 2006. (Cited on page 59.)

[256] Manoj B. Gawande, Anandarup Goswami, François-Xavier Felpin, Tewodros Asefa, Xiaoxi Huang, Rafael Silva, Xiaoxin Zou, Radek Zboril, and Rajender S. Varma. Cu and Cu-based nanoparticles: Synthesis and applications in catalysis. *Chemical Reviews*, 116(6):3722–3811, 2016. PMID: 26935812. (Cited on page 59.)

[257] Yizhong Lu and Wei Chen. Sub-nanometre sized metal clusters: from synthetic challenges to the unique property discoveries. *Chem. Soc. Rev.*, 41:3594–3623, 2012. (Cited on page 59.)

[258] Zhenguang Wang, Bingkun Chen, and Andrey L. Rogach. Synthesis, optical properties and applications of light-emitting copper nanoclusters. *Nanoscale Horiz.*, 2:135–146, 2017. (Cited on page 59.)

[259] Yu-Syuan Lin, Yu-Feng Lin, Amit Nain, Yu-Fen Huang, and Huan-Tsung Chang. A critical review of copper nanoclusters for monitoring of water quality. *Sensors and Actuators Reports*, 3:100026, 2021. (Cited on page 59.)

[260] Masahiro Itoh, Vijay Kumar, Tadafumi Adschiri, and Yoshiyuki Kawazoe. Comprehensive study of sodium, copper, and silver clusters over a wide range of sizes $2<n<75$. *The Journal of Chemical Physics*, 131(17):174510, 2009. (Cited on pages 59 and 74.)

[261] Karl Jug, Bernd Zimmermann, Patrizia Calaminici, and Andreas M. Köster. Structure and stability of small copper clusters. *The Journal of Chemical Physics*, 116(11):4497–4507, 2002. (Cited on page 59.)

[262] Patrizia Calaminici, Florian Janetzko, Andreas M. Koster, Roberto Mejia-Olvera, and Bernardo Zuniga-Gutierrez. Density functional theory optimized

basis sets for gradient corrected functionals: 3d transition metal systems. *The Journal of Chemical Physics*, 126(4):044108, 2007. (Cited on page 59.)

[263] Carlo Massobrio, Alfredo Pasquarello, and Andrea Dal Corso. Structural and electronic properties of small cu_n clusters using generalized-gradient approximations within density functional theory. *The Journal of Chemical Physics*, 109(16):6626–6630, 1998. (Cited on page 59.)

[264] P. Calaminici, A. M. Koster, N. Russo, and D. R. Salahub. A density functional study of small copper clusters: Cu_n (n<5). *The Journal of Chemical Physics*, 105(21):9546–9556, 1996. (Cited on page 59.)

[265] Albert Poater, Miquel Duran, Pablo Jaque, Alejandro Toro-Labbé, and Miquel Sola. Molecular structure and bonding of copper cluster monocarbonyls Cu_nCO (n = 1-9). *The Journal of Physical Chemistry B*, 110(13):6526–6536, 2006. PMID: 16570950. (Cited on page 59.)

[266] Patrizia Calaminici, Andreas M. Koster, and Zeferino Gómez-Sandoval. Density functional study of the structure and properties of Cu_9 and Cu_9^-. *Journal of Chemical Theory and Computation*, 3(3):905–913, 2007. PMID: 26627410. (Cited on page 60.)

[267] M. Yang, F. Yang, K. A. Jackson, and J. Jellinek. Probing the structural evolution of Cu_N, n=9-20, through a comparison of computed electron removal energies and experimental photoelectron spectra. *The Journal of Chemical Physics*, 132(6):064306, 2010. (Cited on page 60.)

[268] S. Lecoultre, A. Rydlo, C. Félix, J. Buttet, S. Gilb, and W. Harbich. Optical absorption of small copper clusters in neon: Cu_n, (n = 1-9). *The Journal of Chemical Physics*, 134(7):074303, 2011. (Cited on pages 60, 81 and 83.)

[269] C. Binns. Nanoclusters deposited on surfaces. *Surface Science Reports*, 44(1):1–49, 2001. (Cited on page 60.)

[270] Matthias Brack. The physics of simple metal clusters: self-consistent jellium model and semiclassical approaches. *Rev. Mod. Phys.*, 65:677–732, Jul 1993. (Cited on page 60.)

[271] T.P. Martin. Shells of atoms. *Physics Reports*, 273(4):199–241, 1996. (Cited on page 60.)

[272] Masaki Sakurai, Koji Watanabe, Kenji Sumiyama, and Kenji Suzuki. Magic numbers in transition metal (Fe, Ti, Zr, Nb, and Ta) clusters observed by time-of-flight mass spectrometry. *The Journal of Chemical Physics*, 111(1):235–238, 1999. (Cited on page 60.)

[273] Sarah Darby, Thomas V. Mortimer-Jones, Roy L. Johnston, and Christopher Roberts. Theoretical study of Cu-Au nanoalloy clusters using a genetic algorithm. *The Journal of Chemical Physics*, 116(4):1536–1550, 2002. (Cited on pages 60 and 76.)

[274] Galip H. Guvelioglu, Pingping Ma, Xiaoyi He, Robert C. Forrey, and Hansong Cheng. Evolution of small copper clusters and dissociative chemisorption of hydrogen. *Phys. Rev. Lett.*, 94:026103, Jan 2005. (Cited on pages 60 and 63.)

[275] Masahiro Itoh, Vijay Kumar, and Yoshiyuki Kawazoe. Growth behaviors and electronic structures of Na and Cu nanoclusters: The role of sp-d hibridization. *International Journal of Modern Physics B*, 19(15n17):2421–2426, 2005. (Cited on page 60.)

[276] Mingli Yang, Koblar A. Jackson, Christof Koehler, Thomas Frauenheim, and Julius Jellinek. Structure and shape variations in intermediate-size copper clusters. *The Journal of Chemical Physics*, 124(2):024308, 2006. (Cited on page 60.)

[277] Minglong Jiang, Qun Zeng, Tingting Zhang, Mingli Yang, and Koblar Alan Jackson. Icosahedral to double-icosahedral shape transition of copper clusters. *The Journal of Chemical Physics*, 136(10):104501, 2012. (Cited on page 60.)

[278] Riguang Zhang, Mao Peng, Tian Duan, and Baojun Wang. Insight into size dependence of C_2 oxygenate synthesis from syngas on cu cluster: The effect of cluster size on the selectivity. *Applied Surface Science*, 407:282–296, 2017. (Cited on page 60.)

[279] Chen Shuangjing, Chen Xin, and Zhang Hui. Probing the activity of Ni_{13}, Cu_{13}, and $Ni_{12}Cu$ clusters towards the ammonia decomposition reaction by density functional theory. *Journal of Materials Science*, 52(6):3162–3168, 2017. (Cited on page 60.)

[280] Keisuke Takahashi. First-principles design of cu12shellfecore core-shell clusters assembled with K_3O into hexameric rings: Implications for gas-storage materials. *ACS Applied Nano Materials*, 3(1):55–58, 2020. (Cited on page 60.)

[281] J P Chou, C R Hsing, C M Wei, C Cheng, and C M Chang. Ab initio random structure search for 13-atom clusters of FCC elements. *Journal of Physics: Condensed Matter*, 25(12):125305, feb 2013. (Cited on pages 60 and 63.)

[282] J. Akola, H. Häkkinen, and M. Manninen. Ionization potential of aluminum clusters. *Phys. Rev. B*, 58:3601–3604, Aug 1998. (Cited on page 60.)

[283] Wei-Li Li, Ya-Fan Zhao, Han-Shi Hu, Jun Li, and Lai-Sheng Wang. $[B_{30}^-]$: A quasiplanar chiral boron cluster. *Angewandte Chemie International Edition*, 53(22):5540–5545, 2014. (Cited on page 60.)

[284] Peng Lv, Zhansheng Lu, Feng Yang, Yi Zhang, Xinwei Yang, Guoliang Xu, and Zongxian Yang. A theoretical study of the lowest-energy PtPd co-doped silicon clusters: Chirality and fluxional transformation. *Physics Letters A*, 381(9):873–878, 2017. (Cited on page 60.)

[285] Yu-Jin Kong, Zhi-Ping Yan, Si Li, Hui-Fang Su, Kai Li, You-Xuan Zheng, and Shuang-Quan Zang. Photoresponsive propeller-like chiral AIE copper(I) clusters. *Angewandte Chemie International Edition*, 59(13):5336–5340, 2020. (Cited on page 60.)

[286] Yi Rao, Yimin Lei, Xiangyuan Cui, Zongwen Liu, and Fuyi Chen. Optical and magnetic properties of Cu-doped 13-atom Ag nanoclusters. *Journal of Alloys and Compounds*, 565:50–55, 2013. (Cited on page 60.)

[287] Wenlong Yang, Giovanna Longhi, Sergio Abbate, Andrea Lucotti, Matteo Tommasini, Claudio Villani, Vincent J. Catalano, Aleksandr O. Lykhin, Sergey A. Varganov, and Wesley A. Chalifoux. Chiral peropyrene: Synthesis, structure, and properties. *Journal of the American Chemical Society*, 139(37):13102–13109, 2017. PMID: 28829125. (Cited on page 61.)

[288] Dimitrios G. Liakos, Yang Guo, and Frank Neese. Comprehensive benchmark results for the domain based local pair natural orbital coupled cluster method (DLPNO-CCSD(T)) for closed- and open-shell systems. *The Journal of Physical Chemistry A*, 124(1):90–100, 2020. PMID: 31841627. (Cited on pages 61 and 65.)

[289] Axel D. Becke. Density functional thermochemistry. iii. the role of exact exchange. *The Journal of Chemical Physics*, 98(7):5648–5652, 1993. (Cited on page 61.)

[290] John P. Perdew and Yue Wang. Accurate and simple analytic representation of the electron-gas correlation energy. *Phys. Rev. B*, 45:13244–13249, Jun 1992. (Cited on page 61.)

[291] John P. Perdew, J. A. Chevary, S. H. Vosko, Koblar A. Jackson, Mark R. Pederson, D. J. Singh, and Carlos Fiolhais. Atoms, molecules, solids, and surfaces: Applications of the generalized gradient approximation for exchange and correlation. *Phys. Rev. B*, 46:6671–6687, Sep 1992. (Cited on pages 61 and 74.)

[292] Estefanía Fernández, Mercedes Boronat, and Avelino Corma. Trends in the reactivity of molecular O2 with copper clusters: Influence of size and shape. *The Journal of Physical Chemistry C*, 119(34):19832–19846, 2015. (Cited on page 61.)

[293] Pablo Jaque and Alejandro Toro-Labbé. Characterization of copper clusters through the use of density functional theory reactivity descriptors. *The Journal of Chemical Physics*, 117(7):3208–3218, 2002. (Cited on page 61.)

[294] Christopher J. Cramer and Donald G. Truhlar. Density functional theory for transition metals and transition metal chemistry. *Phys. Chem. Chem. Phys.*, 11:10757–10816, 2009. (Cited on page 61.)

[295] Aron J. Cohen, Paula Mori-Sánchez, and Weitao Yang. Challenges for density functional theory. *Chemical Reviews*, 112(1):289–320, 2012. PMID: 22191548. (Cited on page 61.)

[296] P. Jeffrey Hay and Willard R. Wadt. Ab initio effective core potentials for molecular calculations. potentials for the transition metal atoms sc to hg. *The Journal of Chemical Physics*, 82(1):270–283, 1985. (Cited on page 61.)

[297] Florian Weigend and Reinhart Ahlrichs. Balanced basis sets of split valence, triple zeta valence and quadruple zeta valence quality for H to Rn: Design and assessment of accuracy. *Phys. Chem. Chem. Phys.*, 7:3297–3305, 2005. (Cited on page 61.)

[298] Q. Zeng, X. Wang, M. L. Yang, and H. B. Fu. Interplay between geometrical and electronic stability of neutral and anionic Cu_{13} clusters: a first-principles study. *The European Physical Journal D*, 58(1):125–129, May 2010. (Cited on page 61.)

[299] Tayyibe Bardakc, Mustafa Kumru, and Ahmet Altun. Molecular structures, charge distributions, and vibrational analyses of the tetracoordinate Cu(II), Zn(II), Cd(II), and Hg(II) bromide complexes of p-toluidine investigated by density functional theory in comparison with experiments. *Journal of Molecular Structure*, 1116:292–302, 2016. (Cited on page 61.)

[300] Piotr Matczak. Assessment of B3LYP combined with various ECP basis sets for systems containing Pd, Sn, and Pb. *Computational and Theoretical Chemistry*, 983:25–30, 2012. (Cited on page 61.)

[301] Sven Heiles and Roy L. Johnston. Global optimization of clusters using electronic structure methods. *International Journal of Quantum Chemistry*, 113(18):2091–2109, 2013. (Cited on page 62.)

[302] Alba Vargas-Caamal, Jose Luis Cabellos, Filiberto Ortiz-Chi, Henry S. Rzepa, Albeiro Restrepo, and Gabriel Merino. How many water molecules does it take to dissociate HCl? *Chemistry A European Journal*, 22(8):2812–2818, 2016. (Cited on page 62.)

[303] Sudip Pan, Diego Moreno, Jose Luis Cabellos, Jonathan Romero, Andres Reyes, Gabriel Merino, and Pratim K. Chattaraj. In quest of strong Be-Ng bonds among the neutral Ng-Be complexes. *The Journal of Physical Chemistry A*, 118(2):487–494, 2014. PMID: 24199587. (Cited on page 62.)

[304] Rosa Elena Navarro, Octavio Serna-Medina, Yedith Soberanes, José Luis Cabellos, Motomichi Inoue, Hisila Santacruz, and A. Amarillas. 1H NMR of paramagnetic Dy^{3+} complex with DTPA amide pxy cyclophane possible probing action toward histidine and histamine. *Polyhedron*, 181:114474, 2020. (Cited on page 62.)

[305] José Luis Cabellos, Filiberto Ortiz-Chi, , and Gabriel Merino. Glomos 1.0. *Cinvestav-Merida*, 1(1):1–10, 2018. (Cited on page 62.)

[306] Peter L. Rodriguez-Kessler, Adan R. Rodriguez-Dominguez, and Alvaro Muñoz Castro. Systematic cluster growth: a structure search method for transition metal clusters. *Phys. Chem. Chem. Phys.*, 23:4935–4943, 2021. (Cited on page 63.)

[307] Dil K. Limbu, Michael U. Madueke, Raymond Atta-Fynn, David A. Drabold, and Parthapratim Biswas. Ab initio density-functional studies of 13-atom Cu and Ag clusters. *Journal of Physics: Conference Series*, 1252:012009, jun 2019. (Cited on page 63.)

[308] Galip H. Guvelioglu, Pingping Ma, Xiaoyi He, Robert C. Forrey, and Hansong Cheng. First principles studies on the growth of small Cu clusters and the dissociative chemisorption of H_2. *Phys. Rev. B*, 73:155436, Apr 2006. (Cited on pages 63, 76 and 77.)

[309] Mukul. Kabir, Abhijit Mookerjee, and A. Bhattacharya. Copper clusters: electronic effect dominates over geometric effect. *The European Physical Journal D - Atomic, Molecular, Optical and Plasma Physics*, 31(3):477–485, December 2004. (Cited on page 63.)

[310] Linus Pauling. On the nature of the bonding in Cu_2 a comment. *The Journal of Chemical Physics*, 78(6):3346–3346, 1983. (Cited on page 63.)

[311] Takeshi Iwasa, Takaaki Sato, Makito Takagi, Min Gao, Andrey Lyalin, Masato Kobayashi, Ken-ichi Shimizu, Satoshi Maeda, and Tetsuya Taketsugu. Combined automated reaction pathway searches and sparse modeling analysis for catalytic properties of lowest energy twins of Cu_{13}. *The Journal of Physical Chemistry A*, 123(1):210–217, 2019. (Cited on page 63.)

[312] R. C. Longo and L. J. Gallego. Structures of 13-atom clusters of FCC transition metals by ab initio and semiempirical calculations. *Phys. Rev. B*, 74:193409, Nov 2006. (Cited on page 63.)

[313] E. de la Puente, A. Aguado, A. Ayuela, and J. M. López. Structural and electronic properties of small neutral $(MgO)_n$ clusters. *Phys. Rev. B*, 56:7607–7614, Sep 1997. (Cited on page 65.)

[314] Jianmin Tao, John P. Perdew, Viktor N. Staroverov, and Gustavo E. Scuseria. Climbing the density functional ladder: Nonempirical meta–generalized

gradient approximation designed for molecules and solids. *Phys. Rev. Lett.*, 91:146401, Sep 2003. (Cited on page 65.)

[315] Timothy J. Lee and Peter R. Taylor. A diagnostic for determining the quality of single-reference electron correlation methods. *International Journal of Quantum Chemistry*, 36(S23):199–207, 1989. (Cited on page 66.)

[316] Antonio Fernández-Ramos, Benjamin A. Ellingson, Rubén Meana-Pañeda, Jorge M. C. Marques, and Donald G. Truhlar. Symmetry numbers and chemical reaction rates. *Theoretical Chemistry Accounts*, 118(4):813–826, Oct 2007. (Cited on page 66.)

[317] Michael K. Gilson and Karl K. Irikura. Symmetry numbers for rigid, flexible, and fluxional molecules: Theory and applications. *The Journal of Physical Chemistry B*, 114(49):16304–16317, 2010. PMID: 21141931. (Cited on page 66.)

[318] Prince Ravat. Carbo[n]helicenes restricted to enantiomerize: an insight into the design process of configurationally stable functional chiral PAHs. *Chemistry - A European Journal*, 27(12):3957–3967, 2021. (Cited on page 68.)

[319] Bjorn Jensen. Quantum mechanics on surfaces. In Mohammad Reza Pahlavani, editor, *Some Applications of Quantum Mechanics*, chapter 8. IntechOpen, Rijeka, 2012. (Cited on page 69.)

[320] J. P. Wilcoxon and B. L. Abrams. Synthesis, structure and properties of metal nanoclusters. *Chem. Soc. Rev.*, 35:1162–1194, 2006. (Cited on page 73.)

[321] Riccardo Ferrando, Julius Jellinek, and Roy L. Johnston. Nanoalloys: From theory to applications of alloy clusters and nanoparticles. *Chemical Reviews*, 108(3):845–910, 2008. (Cited on page 73.)

[322] Gajendra Kumar Inwati, Yashvant Rao, and Man Singh. Thermodynamically induced in situ and tunable cu plasmonic behaviour. *Scientific Reports*, 8(1):3006, Feb 2018. (Cited on page 73.)

[323] Ammu Mathew and Thalappil Pradeep. Noble metal clusters: Applications in energy, environment, and biology. *Particle & Particle Systems Characterization*, 31(10):1017–1053, 2014. (Cited on page 73.)

[324] Paulrajpillai Lourdu Xavier, Kamalesh Chaudhari, Ananya Baksi, and Thalappil Pradeep. Protein-protected luminescent noble metal quantum clusters: an emerging trend in atomic cluster nanoscience. *Nano reviews*, 3:10.3402/nano.v3i0.14767, 2012. (Cited on page 73.)

[325] Chuanchuan Zhang, Haiming Duan, Xin Lv, Biaobing Cao, Ablat Abliz, Zhaofeng Wu, and Mengqiu Long. Static and dynamical isomerization of Cu_{38} cluster. *Scientific Reports*, 9(1):7564, May 2019. (Cited on pages 73, 74, 75, 80 and 84.)

[326] Peisheng Liu, Hao Wang, Xiaoming Li, Muchen Rui, and Haibo Zeng. Localized surface plasmon resonance of Cu nanoparticles by laser ablation in liquid media. *RSC Adv.*, 5:79738–79745, 2015. (Cited on page 73.)

[327] Puru Jena and A. W. Castleman. Clusters: A bridge across the disciplines of physics and chemistry. *Proceedings of the National Academy of Sciences*, 103(28):10560–10569, 2006. (Cited on page 73.)

[328] Dung T. Tran and Roy L. Johnston. Theoretical study of $Cu_{38_n}Au_n$ clusters using a combined empirical potential-density functional approach. *Phys. Chem. Chem. Phys.*, 11:10340–10349, 2009. (Cited on page 73.)

[329] Francesca Baletto, Arnaldo Rapallo, Giulia Rossi, and Riccardo Ferrando. Dynamical effects in the formation of magic cluster structures. *Phys. Rev. B*, 69:235421, Jun 2004. (Cited on pages 73 and 74.)

[330] Walt A. de Heer. The physics of simple metal clusters: experimental aspects and simple models. *Rev. Mod. Phys.*, 65:611–676, Jul 1993. (Cited on page 74.)

[331] Jonathan P. K. Doye and David J. Wales. Global minima for transition metal clusters described by sutton-chen potentials. *New J. Chem.*, 22:733–744, 1998. (Cited on page 74.)

[332] C. L. Pettiette, S. H. Yang, M. J. Craycraft, J. Conceicao, R. T. Laaksonen, O. Cheshnovsky, and R. E. Smalley. Ultraviolet photoelectron spectroscopy of copper clusters. *The Journal of Chemical Physics*, 88(9):5377–5382, 1988. (Cited on page 74.)

[333] O. Kostko, N. Morgner, M. Astruc Hoffmann, and B. von Issendorff. Photoelectron spectra of Na_n- and Cu_n- with n = 20–40: observation ofsurprising similarities. *The European Physical Journal D - Atomic, Molecular, Optical and Plasma Physics*, 34(1):133–137, Jul 2005. (Cited on pages 74 and 76.)

[334] Nobuhisa Fujima and Tsuyoshi Yamaguchi. Magnetic anomaly and shell structure of electronic states of nickel microclusters. *Journal of the Physical Society of Japan*, 58(9):3290–3297, 1989. (Cited on page 74.)

[335] Christopher D. Taylor, Matthew Neurock, and John R. Scully. First-principles investigation of the fundamental corrosion properties of a model Cu_{38} nanoparticle and the (111), (113) surfaces. *Journal of The Electrochemical Society*, 155(8):C407, 2008. (Cited on page 74.)

[336] Dabin Qi, Xudong Luo, Jun Yao, Xiaojun Lu, and Zhan Zhang. Computational study of reverse water gas shift reaction on Cu_{38} cluster model and cu slab model. *Journal of Theoretical and Computational Chemistry*, 19(02):2050008, 2020. (Cited on page 74.)

[337] Nozomi Takagi, Kazuya Ishimura, Masafuyu Matsui, Ryoichi Fukuda, Masahiro Ehara, and Shigeyoshi Sakaki. Core-shell versus other structures in binary Cu_{38}-nMn nanoclusters (M = Ru, Rh, Pd, Ag, Os, Ir, Pt, and Au; n = 1, 2, and 6): Theoretical insight into determining factors. *The Journal of Physical Chemistry C*, 121(19):10514–10528, 2017. (Cited on page 74.)

[338] I. A. Hijazi and Y. H. Park. Structure of pure metallic nanoclusters: Monte carlo simulation and ab initio study. *The European Physical Journal D*, 59(2):215–221, Aug 2010. (Cited on page 74.)

[339] V. G. Grigoryan, D. Alamanova, and M. Springborg. Structure and energetics of nickel, copper, and gold clusters. *The European Physical Journal D - Atomic, Molecular, Optical and Plasma Physics*, 34(1):187–190, Jul 2005. (Cited on page 74.)

[340] Şakir Erkoç and Riad Shaltaf. Monte carlo computer simulation of copper clusters. *Phys. Rev. A*, 60:3053–3057, Oct 1999. (Cited on page 74.)

[341] ŞSakir Erkoç. An empirical many-body potential energy function constructed from pair-interactions. *Zeitschrift für Physik D Atoms, Molecules and Clusters*, 32(3):257–260, Sep 1994. (Cited on page 74.)

[342] Valeri G. Grigoryan, Denitsa Alamanova, and Michael Springborg. Structure and energetics of Cu_N clusters with ($2 < N < 150$): An embedded-atom-method study. *Phys. Rev. B*, 73:115415, Mar 2006. (Cited on page 74.)

[343] Bo Zhao, Riguang Zhang, Zaixing Huang, and Baojun Wang. Effect of the size of Cu clusters on selectivity and activity of acetylene selective hydrogenation. *Applied Catalysis A: General*, 546:111–121, 2017. (Cited on page 74.)

[344] Estefanía Fernández, Mercedes Boronat, and Avelino Corma. Trends in the reactivity of molecular O_2 with copper clusters: Influence of size and shape. *The Journal of Physical Chemistry C*, 119(34):19832–19846, 2015. (Cited on page 74.)

[345] S. Núnez and R. L. Johnston. Structures and chemical ordering of small Cu-Ag clusters. *The Journal of Physical Chemistry C*, 114(31):13255–13266, 2010. (Cited on page 74.)

[346] Young Ho Park and Iyad A. Hijazi. Critical size of transitional copper clusters for ground state structure determination: empirical and ab initio study. *Molecular Simulation*, 38(3):241–247, 2012. (Cited on page 74.)

[347] Cesar Castillo-Quevedo, Carlos Emiliano Buelna-Garcia, Edgar Paredes-Sotelo, Eduardo Robles-Chaparro, Edgar Zamora-Gonzalez, Martha Fabiola Martin-del Campo-Solis, Jesus Manuel Quiroz-Castillo, Teresa del Castillo-Castro, Gerardo Martínez-Guajardo, Aned de Leon-Flores, Manuel Cortez-Valadez, Filiberto Ortiz-Chi, Tulio Gaxiola, Santos Jesus Castillo, Alejandro

Vásquez-Espinal, Sudip Pan, and Jose Luis Cabellos. Effects of temperature on enantiomerization energy and distribution of isomers in the chiral Cu_{13} cluster. *Molecules*, 26(18), 2021. (Cited on page 74.)

[348] Nicola Marzari, David Vanderbilt, and M. C. Payne. Ensemble density-functional theory for ab initio molecular dynamics of metals and finite-temperature insulators. *Phys. Rev. Lett.*, 79:1337–1340, Aug 1997. (Cited on page 74.)

[349] L. V. Redel, Yu. Ya. Gafner, and S. L. Gafner. Role of magic numbers in structure formation in small silver nanoclusters. *Physics of the Solid State*, 57(10):2117–2125, Oct 2015. (Cited on page 75.)

[350] Uzi Even, Narda Ben-Horin, and Joshua Jortner. Multistate isomerization of size-selected clusters. *Phys. Rev. Lett.*, 62:140–143, Jan 1989. (Cited on page 75.)

[351] Mukul Kabir, Abhijit Mookerjee, and A. K. Bhattacharya. Structure and stability of copper clusters: A tight-binding molecular dynamics study. *Phys. Rev. A*, 69:043203, Apr 2004. (Cited on pages 76 and 77.)

[352] Jianhua Zhang, Cai-Zhuang Wang, Zizhong Zhu, Qing Huo Liu, and Kai-Ming Ho. Multimode Jahn-Teller effect in bulk systems: A case of the Nv^0 center in diamond. *Phys. Rev. B*, 97:165204, Apr 2018. (Cited on page 77.)

[353] Matija Zlatar, Maja Gruden-Pavlovic, Carl-Wilhelm Schlapfer, and Claude Daul. Intrinsic distortion path in the analysis of the Jahn-Teller effect. *Journal of Molecular Structure: THEOCHEM*, 954(1):86–93, 2010. DFT09, 13th International Conference on the Applications of Density Functional Theory in Chemistry and Physics. (Cited on page 77.)

[354] U. Opik and Maurice Henry Lecorney Pryce. Studies of the Jahn-Teller effect. i. a survey of the static problem. *Proceedings of the Royal Society of London. Series A. Mathematical and Physical Sciences*, 238(1215):425–447, 1957. (Cited on page 77.)

[355] Stan J. Tinnemans, J. Gerbrand Mesu, Kaisa Kervinen, Tom Visser, T. Alexander Nijhuis, Andrew M. Beale, Daphne E. Keller, Ad M.J. van der Eerden, and Bert M. Weckhuysen. Combining operando techniques in one spectroscopic-reaction cell: New opportunities for elucidating the active site and related reaction mechanism in catalysis. *Catalysis Today*, 113(1):3–15, 2006. Recent Advances in In situ and Operando Studies of Catalytic Reactions. (Cited on page 81.)

[356] Kazuki Hashimoto, Venkata Ramaiah Badarla, Akira Kawai, and Takuro Ideguchi. Complementary vibrational spectroscopy. *Nature Communications*, 10(1):4411, Sep 2019. (Cited on page 81.)

[357] A. Fielicke, G. von Helden, and G. Meijer. Far-infrared spectroscopy of isolated transition metal clusters. *The European Physical Journal D - Atomic, Molecular, Optical and Plasma Physics*, 34(1):83–88, Jul 2005. (Cited on page 81.)

[358] D. E. Powers, S. G. Hansen, M. E. Geusic, A. C. Puiu, J. B. Hopkins, T. G. Dietz, M. A. Duncan, P. R. R. Langridge-Smith, and R. E. Smalley. Supersonic metal cluster beams: laser photoionization studies of copper cluster (Cu_2). *The Journal of Physical Chemistry*, 86(14):2556–2560, 1982. (Cited on page 81.)

[359] Olga V. Lushchikova, Douwe M. M. Huitema, Pablo López-Tarifa, Lucas Visscher, Zahra Jamshidi, and Joost M. Bakker. Structures of Cu_n^+ (n=3-10) clusters obtained by infrared action spectroscopy. *The Journal of Physical Chemistry Letters*, 10(9):2151–2155, 2019. PMID: 30977666. (Cited on page 81.)

[360] Takeshi Yanai, David P Tew, and Nicholas C Handy. A new hybrid exchange-correlation functional using the coulomb-attenuating method (CAM-B3LYP). *Chemical Physics Letters*, 393(1):51–57, 2004. (Cited on page 81.)

[361] Christoph Sieber, Jean Buttet, Wolfgang Harbich, Christian Félix, Roland Mitrić, and Vlasta Bonači ć Koutecký. Isomer-specific spectroscopy of metal clusters trapped in a matrix: Ag_9. *Phys. Rev. A*, 70:041201, Oct 2004. (Cited on pages 81 and 82.)

[362] Vivike J. F. Lapoutre, Marko Haertelt, Gerard Meijer, André Fielicke, and Joost M. Bakker. Communication: IR spectroscopy of neutral transition metal clusters through thermionic emission. *The Journal of Chemical Physics*, 139(12):121101, 2013. (Cited on page 82.)

[363] J. L. Cabellos, Bernardo S. Mendoza, M. A. Escobar, F. Nastos, and J. E. Sipe. Effects of nonlocality on second-harmonic generation in bulk semiconductors. *Phys. Rev. B*, 80:155205, Oct 2009. (Cited on page 82.)

[364] J. L. Cabellos, Cuauhtémoc Salazar, and Bernardo S. Mendoza. Stress-modulated optical spin injection in bulk si and gaas semiconductors. *Phys. Rev. B*, 80:245204, Dec 2009. (Cited on page 82.)

[365] Andreas M. Koster, J. Ulises Reveles, and Jorge M. del Campo. Calculation of exchange-correlation potentials with auxiliary function densities. *The Journal of Chemical Physics*, 121(8):3417–3424, 2004. (Cited on page 84.)

Appendices

Appendix A

Appx. Congress

A.0.1 Attendance certificate *LatinXchem* 2021.

LatinXChem

September 24, 2021

This is to certify that

Edgar Paredes-Sotelo, Carlos Emiliano Buelna-Garcia, Cesar Castillo-Quevedo, and Jose Luis Cabellos

participated in the #LatinXChem Twitter Conference 2021 on Sept. 20, 2021 with the poster #Comp214 entitled:

Relative abundances and enantiomerization energy of the chiral Cu13 cluster at finite temperature

Gabriel Merino
on behalf of the
#LatinXChem Organizing Committee

Andrés Cisneros
#LXChemComp organizer

Fernanda Duarte
#LXChemComp organizer

Joaquín Barroso
#LXChemComp organizer

Figure A.1: Attendance certificate of work presented in the: LatinXchem 2021, Nov. 2012, Virtual Twitter

A.0.2 Attendance certificate *LatinXchem* 2021.

LatinXChem

September 24, 2021

This is to certify that

Carlos Emiliano Buelna-Garcia, Edgar Paredes-Sotelo, Cesar Castillo-Quevedo, and Jose Luis Cabellos

participated in the #LatinXChem Twitter Conference 2021 on Sept. 20, 2021 with the poster #Comp213 entitled:

Theoretical prediction of structures and IR spectra of chiral Be4B8 cluster at different temperatures

Gabriel Merino
on behalf of the
#LatinXChem Organizing Committee

Andrés Cisneros
#LXChemComp organizer

Fernanda Duarte
#LXChemComp organizer

Joaquín Barroso
#LXChemComp organizer

Figure A.2: Attendance certificate of work presented in the: LatinXchem 2021, Nov. 2012, Virtual Twitter

Appendix B

Appx. Be_4B8

B.1 Probability of occurence computed at TPSS-GD3/def2TZVP level of theory.

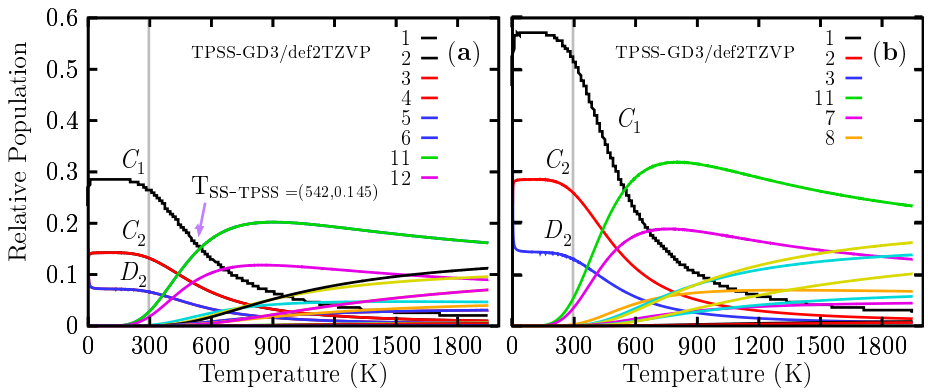

Figure B.1: Probability ocurrence.

For temperatures ranging from 20 to 542 K, the chiral structure, depicted in Figure 4.1(a), strongly dominates as a global minimum. At 542 K, a type-helix chiral structure coexists, depicted Figure 4.1(k), with the chiral putative global minimum at cold temperatures. For temperatures ranging from 543 to 1600 K, the chiral structure's type-helix chiral structure dominates as the putative global minimum. A large difference between the TSS point computed with TPSS functional [239] and that computed with PBEO functional [179]. Thus, it is important to choose the DFT functionals and basis that better describe the system to calculate the relative population and any Boltzmann weighted property.

B.2 Be-Be and B-B bond length evolution for enantiomers

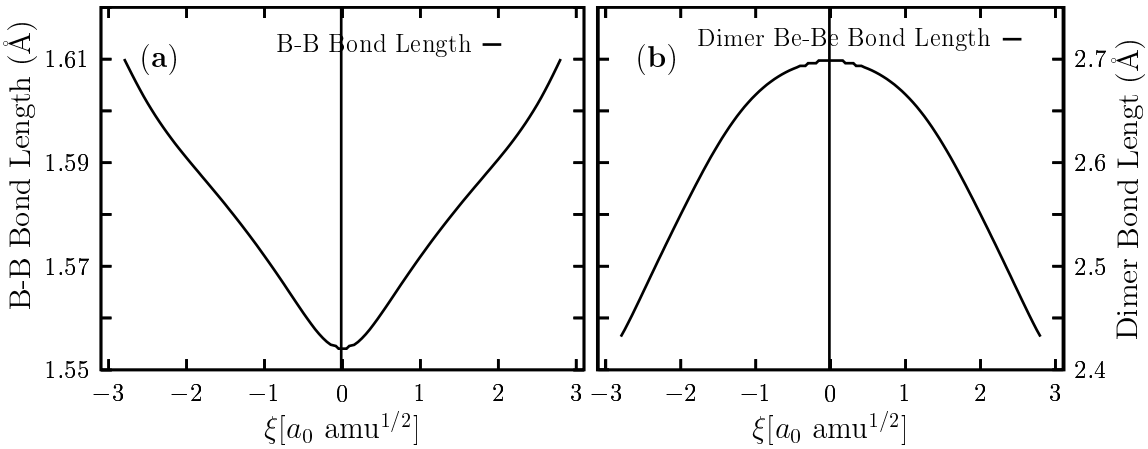

Figure B.2: Figure shows the bond length evolution of the Be-Be dimer.

B.3 Energy of enantiomerization

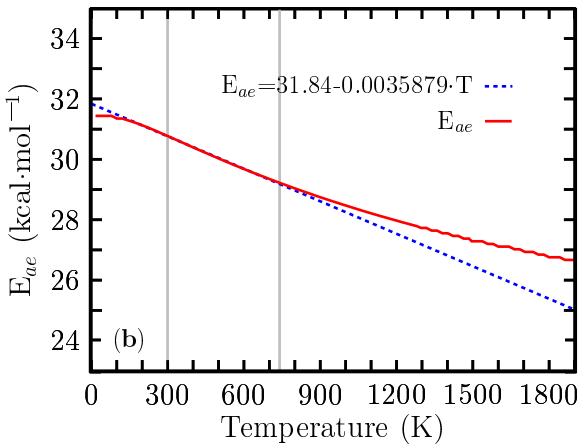

Figure B.3: We show a perfect line depicted in the blue dashed line.

B.4 IR Harmonic vs Anharmonic spectra

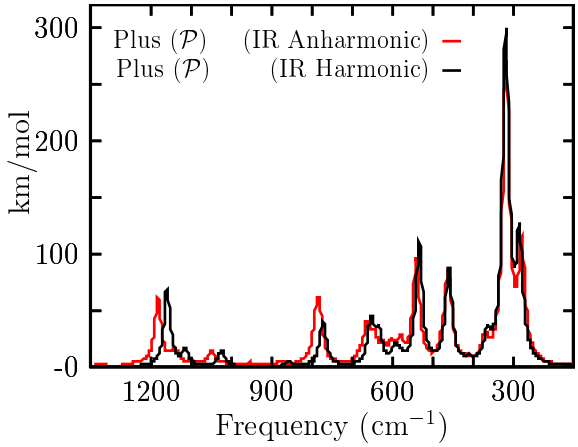

Figure B.4: We show a comparison between IR Harmonic vs IR Anharmonic spectra.

Appendix C

Appx. Cu_{13}

C.1 TPSS/def2-TZVP PBE/def2-TZVP PB68/def2-TZVP

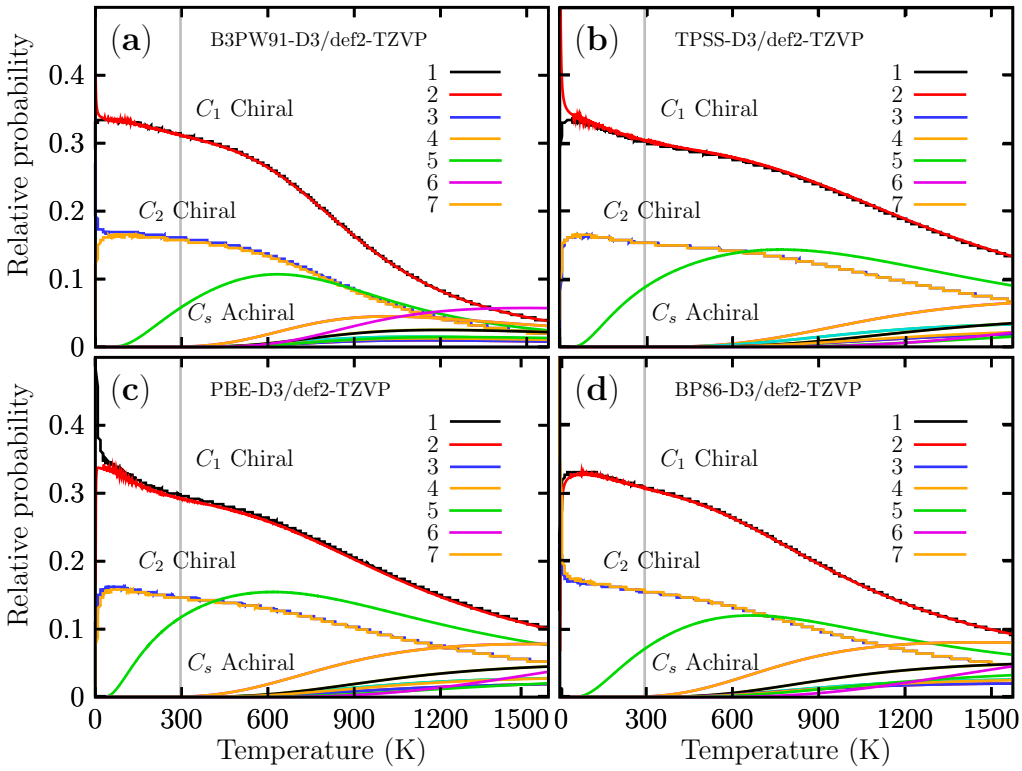

Figure C.1: Probability of occurrence for all isomers.

C.2 XYZ atomic coordiantes of Cu_{13}

```
13
0.0
Cu  -0.990009000000   0.202990000000   0.910273000000
Cu   0.989148000000   0.203204000000  -0.910494000000
Cu   1.307754000000   0.817211000000   1.506707000000
```

```
Cu  -0.756524000000  -1.521352000000  -1.012184000000
Cu  -2.995439000000  -0.494575000000  -0.267184000000
Cu  -0.000551000000   2.308713000000  -0.000120000000
Cu   1.705678000000  -2.128579000000  -1.124758000000
Cu   2.995766000000  -0.493776000000   0.267529000000
Cu   0.756822000000  -1.521006000000   1.012214000000
Cu  -1.308834000000   0.816218000000  -1.506262000000
Cu  -1.705107000000  -2.129263000000   1.124856000000
Cu   2.516484000000   1.969366000000  -0.285914000000
Cu  -2.515188000000   1.970848000000   0.285338000000
13
0.0
Cu   0.000000000000   1.344973000000   0.202955000000
Cu   0.000000000000  -1.344973000000   0.202955000000
Cu  -1.995454000000   0.058043000000   0.817297000000
Cu   1.256550000000  -0.129438000000  -1.520715000000
Cu   2.225189000000   2.023127000000  -0.494441000000
Cu   0.000000000000   0.000000000000   2.309851000000
Cu  -0.329078000000  -2.016616000000  -2.128802000000
Cu  -2.225189000000  -2.023127000000  -0.494441000000
Cu  -1.256550000000   0.129438000000  -1.520715000000
Cu   1.995454000000  -0.058043000000   0.817297000000
Cu   0.329078000000   2.016616000000  -2.128802000000
Cu  -1.493610000000  -2.046117000000   1.968780000000
Cu   1.493610000000   2.046117000000   1.968780000000
```

C.3 ZPE descomposition

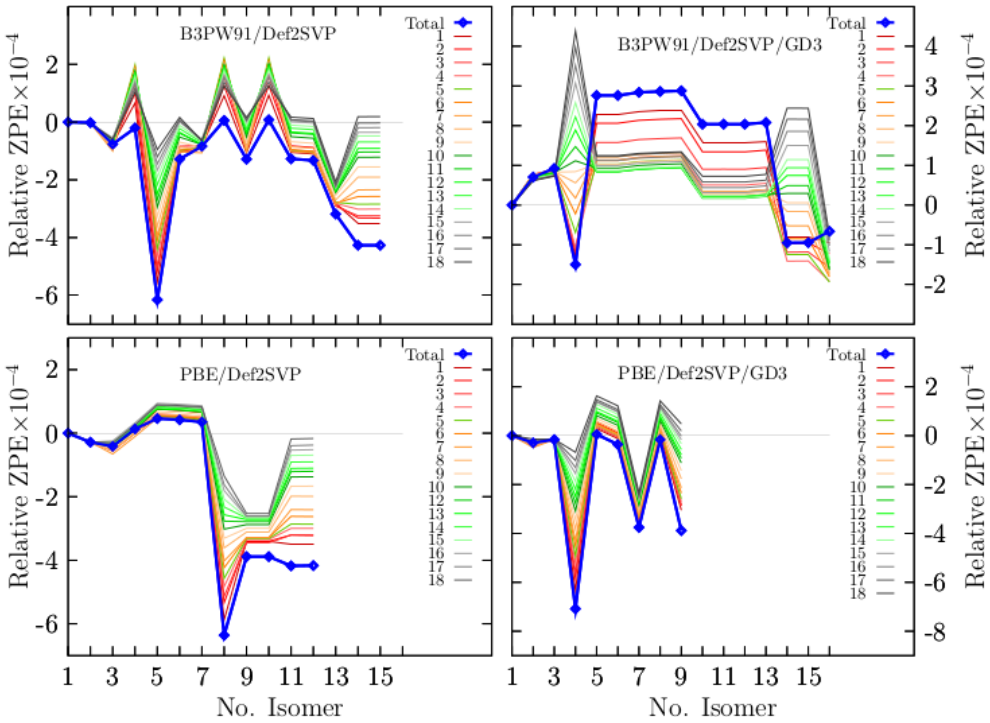

Figure C.2: We show the relative zero-point energy.

C.4 IR spectra

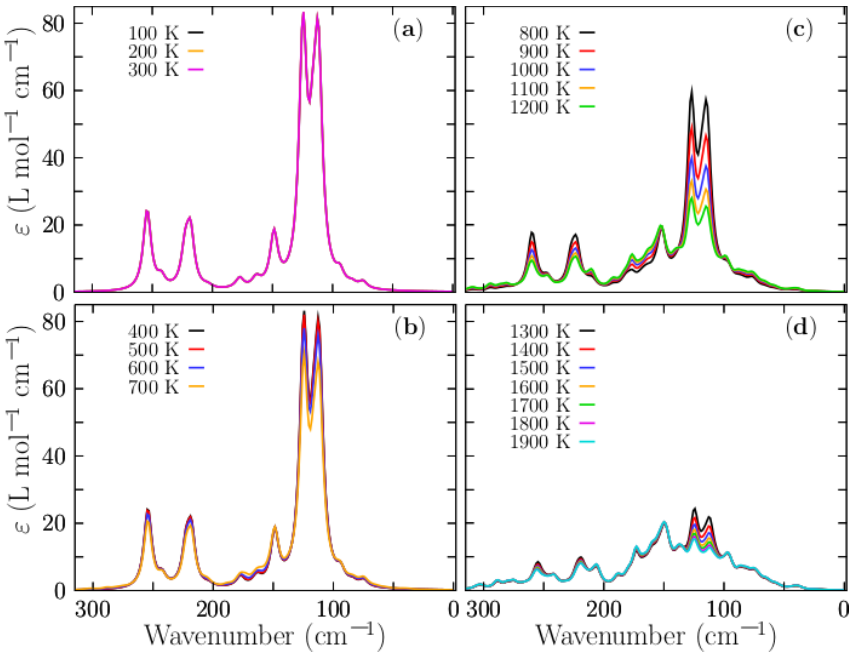

Figure C.3: The IR Boltzmann-spectra-weighted

C.5 UV-Visible spectra for different temperatures

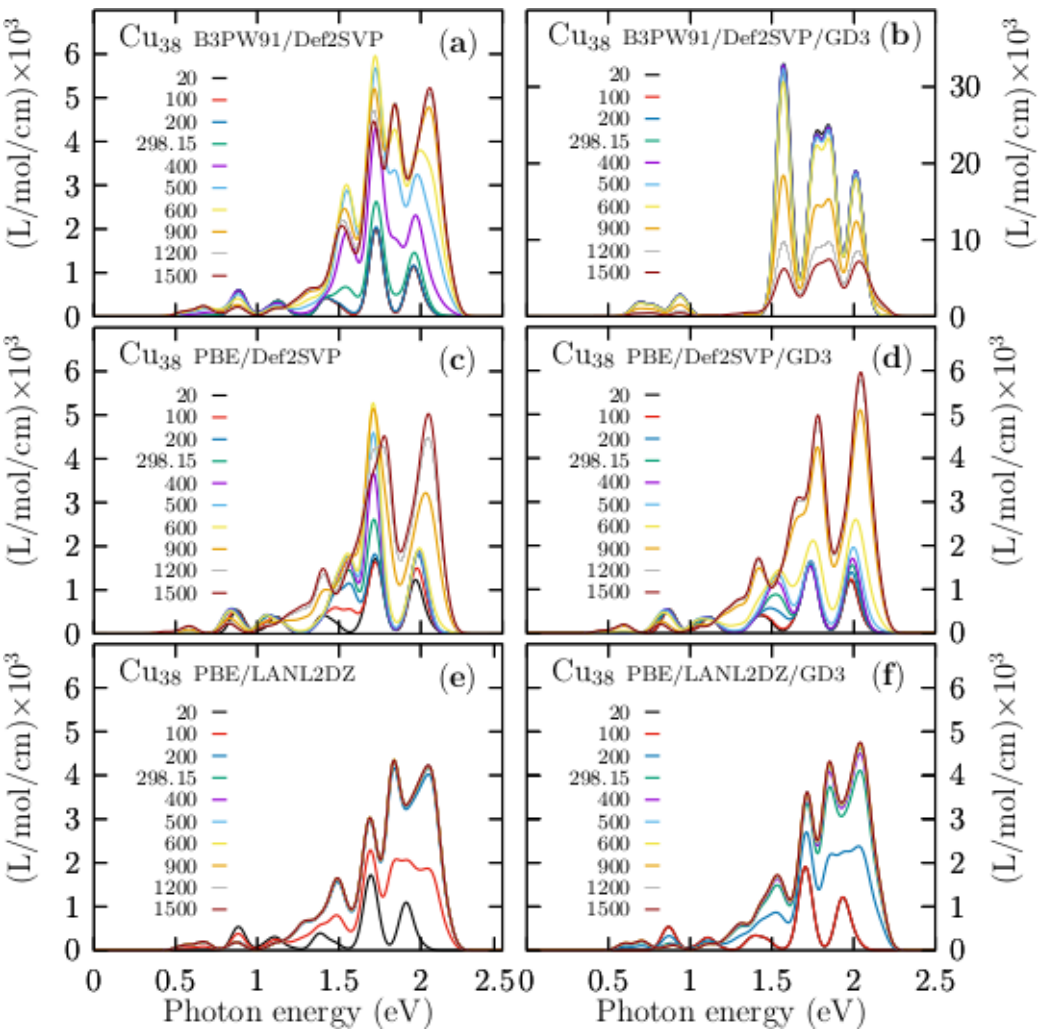

Figure C.4: The UV-visible Boltzmann-spectra-weighted.

C.6 Geometry at B3PW91/Def2svp level of theory

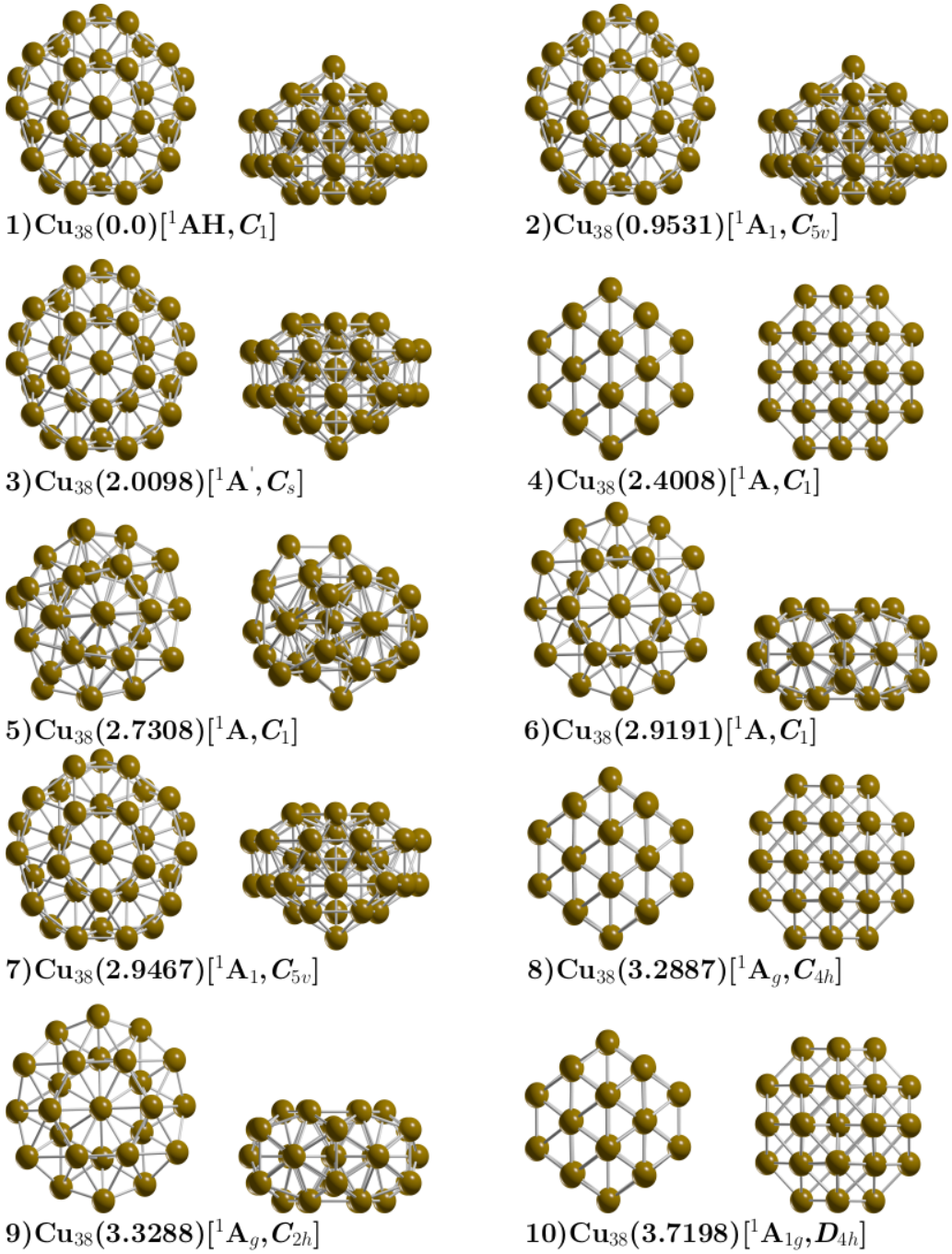

Figure C.5: Optimized geometries in front and side views of neutral Cu_{38} cluster.

Appendix D

Appx. results

List of publications that support this doctoral thesis

List of publications that support the thesis, including publications in journals, and international and national congresses.

1. Materials 2021, 14(1), 112,*Exploration of Free Energy Surface and Thermal Effects on Relative Population and Infrared Spectrum of the $Be_6B_{11}^-$ Fluxional Cluster*

2. Molecules 2021, 26(13), 3953, *Theoretical Prediction of Structures, Vibrational Circular Dichroism, and Infrared Spectra of Chiral Be_4B_8 Cluster at Different Temperatures*

3. Molecules 2021, 26(18), 5710, *Effects of Temperature on Enantiomerization Energy and Distribution of Isomers in the Chiral Cu_{13} Cluster*

4. Front. Chem., 01 March 2022 Sec. *Theoretical and Computational Chemistry, Relative Populations and IR Spectra of Cu_{38} Cluster at Finite Temperature Based on DFT and Statistical Thermodynamics*

5. Book chapter, *Boltzmann Populations of the Fluxional $Be_6B_{11}^-$ and Chiral Be_4B_8 Clusters at Finite Temperatures Computed by DFT and Statistical Thermodynamics*

6. Poster presentation. LatinXchem 2021 (A.0.1)

7. Poster presentation. LatinXchem 2021 (A.0.2)

8. Poster presentation. At the *XXX International Materials Research Congresss 2022*

9. Poster presentation RMFQT. *Exploration of free energy surface and thermal effects of Be_6B_{11} fluxional cluster* on November 2020.

10. Poster presentation RMFQT. In the *GALGOSON hybrid-algorithm in quest of the lowest energy structure* on November 2020.

11. Poster presentation RMFQT. In the *Relative abundances of the chiral* Cu_{13} *cluster at finite temperature* RMFQT on November 2020.

12. Poster presentation. In the XIV Coloquio bienal de ciencias de materiales 2021

- Google scholar, Emiliano Buelna-García